A DOKUMENTUMOT DIGITÁLIS
ALÁÍRÁSSAL LÁTTA EL:
AVDH SIGN
KORMÁNYZATI AZONOSÍTÁSSAL
HITELESÍTETT

BUDAPEST UNIVERSITY OF TECHNOLOGY AND ECONOMICS
FACULTY OF MECHANICAL ENGINEERING
DEPARTMENT OF APPLIED MECHANICS

Identifying the coefficient of friction based on the steering torque

Bendegúz Máté Györök
BSc Thesis

Supervisor:
Dr. Dénes Takács
associate professor

Budapest, 2022

Budapesti Műszaki és Gazdaságtudományi Egyetem
Gépészmérnöki Kar
Műszaki Mechanikai Tanszék
https://www.mm.bme.hu

SZAKDOLGOZAT-FELADAT

NYILVÁNOS

AZONOSÍTÁS	Név: **Györök Bendegúz Máté**		Azonosító: **75223791337**
	Képzéskód: 2N-AM0	Specializáció kódja:	Feladatkiírás azonosítója:
	Szak: Mechatronikai mérnöki alapszak (BSc)	2N-AM0-GM-2017	GEMM:2023-1:2N-AM0:PW5XQR
	Szakdolgozatot kiadó tanszék: Műszaki Mechanikai Tanszék	Záróvizsgát szervező tanszék: Műszaki Mechanikai Tanszék	
	Témavezető: Dr. Takács Dénes (71725502814), egyetemi docens		

FELADAT	Cím	**Súrlódási tényező azonosítása kormányzási nyomaték alapján** Identifying the coefficient of friction based on the steering torque
	Részletes feladatok	1. Végezzen szakirodalmi kutatást és mutassa be milyen megoldások léteznek a kerék-talaj kapcsolat súrlódási tényezőjének azonosítására/becslésére! 2. Egy egyszerű gumimodellt felhasználva készítsen modell alapú becslő algoritmust a súrlódási tényező kormányzott keréken történő azonosítására! 3. Alkalmazzon egy gépi tanulás alapú módszert a feladat megoldására! 4. Numerikus szimulációk segítségével hasonlítsa össze a modell alapú és a gépi tanulás alapú becslő algoritmusok teljesítményét! 5. Tegyen javaslatot egy laboratóriumi kísérleti összeállításra, amellyel mérések végezhetők a kormányzott kerék súrlódási tényezőjével kapcsolatban! 6. Foglalja össze eredményeit magyar és angol nyelven! Készítsen poszter összefoglalót a munkáról!
	Hely	A szakdolgozat készítés helye: Konzulens: ,

ZÁRÓVIZSGA	1. záróvizsga tantárgy(csoport)	2. záróvizsga tantárgy(csoport)	3. záróvizsga tantárgy(csoport)
	ZVEGEMIBMIE Irányításelmélet	**ZVEGEMMBMRD** Robotmechanizmusok dinamikája	**ZVEGEÁTBM04** Áramlások numerikus modellezése

HITELESÍTÉS	Feladat kiadása: 2022. szeptember 5.		Beadási határidő: 2022. december 9.
	Összeállította: Dr. Takács Dénes (71725502814) témavezető	Ellenőrizte: *Dr. Insperger Tamás* s.k. tanszékvezető	Jóváhagyta: *Dr. Györke Gábor* s.k. dékánhelyettes
	Alulírott, a feladatkiírás átvételével egyúttal kijelentem, hogy a Szakdolgozat-készítés c. tantárgy előkövetelményeit maradéktalanul teljesítettem. Tudomásul veszem, hogy jogosulatlan tantárgyfelvétel esetén a jelen feladatkiírás hatálytalan. Györök Bendegúz *Györök Bendegúz Máté*		

DECLARATION OF INDIVIDUAL WORK

I, *Bendegúz Máté Györök* (PW5XQR), the undersigned, student of the Budapest University of Technology and Economics hereby declare that the present thesis has been prepared by myself without any unauthorized help or assistance such that only the specified sources (references, tools, etc.) were used. All parts taken from other sources word by word or after rephrasing but with identical meaning were unambiguously identified with explicit reference to the sources utilized.

Budapest, 2022

Györök Bendegúz

Bendegúz Máté Györök

Contents

Abstract

For precise vehicle motion control, accurate information about the tire-ground relationship is essential. However, the friction properties are changing with time, therefore the identification process is highly complex [1]. The self-aligning torque induced in the contact patch of a steered tire is in close connection with the coefficient of friction. This phenomenon offers a possibility to estimate the friction properties based on the measured steering torque. The goal of this thesis is to analyze the dynamic effects in the contact region of an elastic tire and the ground.

The so-called brush tire model [2] was selected for the investigation, which is a widely used, simplified analytical model that explains the forces caused by the tire deformation. Based on the brush model, a calculation method to estimate the coefficient of friction is derived in the thesis.

Beside the analytic estimation, the use of machine learning methods was also investigated. In this thesis, a simpler neural network was trained to estimate the coefficient of friction. Along with the more “classical” machine learning methods, a scientific machine learning (SciML [3]) process was also implemented, which is a relatively new research area. The method is based on data-driven machine learning as well as model-based mechanical formulas, in such way that the accuracy of the estimation can be enhanced. In the thesis, the nonlinear equation for the coefficient of friction was complemented with a neural network-based learning algorithm, in order to compensate the inaccuracies resulting from the numerical computations and the measurement noise.

The results of the presented estimation methods were compared based on different aspects: accuracy, run time, robustness, etc. The methods were tested with simulations as well as measurements. The measured data-sets were gathered with an experiment set-up manufactured for this purpose.

* * *

Acknowledgement

I would like to thank *Dénes Takács* for the huge amount of help and professional support I received while working on this thesis.

Budapest, 2022

Bendegúz Máté Györök

Notations

The table contains the names of the notations that occur several times, and in case of physical quantities, its unit of measurement. The designation of each quantity is, where possible, the same as that accepted in the domestic and international literature. An explanation of the rarely used notations can be found at their first location.

Latin letters

Notation	Name, comment, value	Dimension
a	contact patch half-length	m
b_{t}	torsional damping	Nms
e	caster length (trail)	m
k	distributed lateral tire stiffness	N/m^2
q	lateral deformation of the tire	m
F_{N}	normal force	N
J	mass moment of inertia	kgm^2
M	steering torque	Nm
M_z	self aligning torque	Nm

Greek letters

Notation	Name, comment, value	Dimension
μ	coefficient of friction	1
ψ	yaw angle	rad

List of Figures

List of Tables

1 Introduction

For precise vehicle motion control, accurate information about the tire-ground relationship is essential. However, the friction properties are not observable, therefore it requires special methods to estimate the coefficient of friction. In the literature, several methods can be found, but none of them provides an accurate, fast, and robust technique, thus the development of an algorithm, that fulfills the above mentioned criterion, is an important topic.

The self-aligning torque induced in the contact patch of a steered tire is in close connection with the coefficient of friction. This phenomenon offers a possibility to estimate the friction properties based on the measured steering torque. This thesis aims to present three methods for estimating the coefficient of friction between the road surface and the tire based on analyzing the dynamic effects in the contact region. The first method solely relies on the analytic modeling of the tire-ground contact. The second method is based on a machine learning technique, neglecting the physics-based part of the system. And finally, the third method combines the advantages of the previous two with a relatively new method in the field of machine learning.

While physics-based modeling is known to provide reasonably accurate solutions for centuries, the field of data-driven modeling with machine learning started to be applied in the last 40-50 years. Although we can find the appropriate equations that describe the dynamics of elastic tires, the modeling is based on assumptions and neglection, which cause errors. In contrast, machine learning techniques often provide accurate solutions, but the inner structure of the network is hard to see through, and the results are hard to interpret on a physical level. Scientific machine learning (SciML) combines physics-based modeling with data-driven approximations, therefore providing more accurate results, because the unmodeled effects are compensated.

1.1 Structure of the thesis

The thesis are categorised into different sections, as follow. In Section 1, the studies, that deal with the subject of estimating the coefficient of friction between the road surface and the tire, are presented and reviewed. A few different methods have been developed by researchers, but none of them is able to provide a quick and robust technique to identify the friction properties accurately. Later on, these methods are listed and categorised, also the advantages and disadvantages are discussed for each method.

In Section 2, the investigated mechanical system, the so-called towed wheel model is introduced, then an analytic tire model - the brush tire model - is being discussed. A simulation environment is developed based on the brush model, in order to analyze the dynamics of the system.

In Section 3, an estimation method is derived, based on the analytic brush tire model.

First, the deformation of the center line of an elastic tire is expressed with an analytic function, then the estimation process is presented with the results on simulated data sets.

Section 4 presents the other two estimation methods. After a brief introduction to artificial neural networks, an estimation technique is discussed using neural networks. Then, a relatively new topic is discussed, namely the field of scientific machine learning, which effectively combines data-driven modeling with physics-based equations. Within SciML, a new method is proposed to solve nonlinear dynamical problems. The results of all three estimation algorithms are compared on simulation data.

In Section 5, an experiment process is discussed. An already established measurement set-up at the Department of Applied Mechanics was modified, in order to test the proposed estimation algorithms on measured data. After discussing the experiment process, the results of the estimations are compared based on different aspects.

In Section 6, the achieved results are summarized, and the final conclusions are drawn. The possible practical applications and the options for further development are also discussed.

1.2 Overview of the literature

The main inspiration of this thesis was the self-balancing motorcycle developed by Honda [4] (illustrated in Figure 1.1), which have been first unveiled in 2017. The motor is able to stabilize itself, when standing still (with no longitudinal motion) using the Honda Moto Riding Assist technology. The motorcycle is balanced by the steering assist system, instead of using gyroscopes as other companies did previously. This industrial research area inspired the topic of the thesis, because knowledge about the frictional relation between the road surface and the elastic tire would provide important information for such steering control task. Similarly to the dynamical problem, that the Honda researchers faced, in this thesis an estimation method for the coefficient of friction between the road and the tire is developed for a vehicle with zero longitudinal velocity.

Just as the mentioned self-balancing motorcycle, other problems in vehicle dynamics would benefit greatly with accurate estimation of the frictional properties in the contact region of road surface and elastic tires. Knowledge about the coefficient of friction makes vehicle control systems more robust and accurate, therefore several studies have been done, in order to develop an estimation method for the friction parameters of tires. In the literature, several estimation approaches can be found, that can be categorised into two groups: cause-based and effect-based techniques [6]. Different methods require different sensors and calculation methods, thus each estimation process has different drawbacks and advantages, which are summarized in Table 1.1.

Cause-based estimations in general utilize some kind of image recognition method in order to provide an estimation for the frictional properties of the road. Kuno and Sugiura proposed a system based on CCD cameras that provides information about road surface

Figure 1.1: Self-balancing motorcycle developed by Honda [5].

conditions [7]. Although the method proved to be reliable during certain conditions, it only calculates from the road surface gloss, which is not the only factor for identifying the coefficient of friction. Holzmann et al. in [8], developed a method based on generic luminance, with sound measurements acquired via a microphone to further improve the reliability of the system. The technique proved to be more accurate, than the previously proposed methods, but still had some drawbacks. In general, vision-based predictions have several possibilities in store for the future, with rapidly improving vision recognition software, but currently, they are not reliable in bad lighting. Another cause-based estimation technique can be found in several commercial vehicles: the road condition can be estimated based on the ambient temperature. This technique does not provide an exact value for the coefficient of friction, but can be used as a warning system for the driver. The advantages of cause-based methods are that the friction properties of the road surface can be predicted ahead, thus, important information can be supplied to the control systems of the vehicle (e.g. ABS control or even the steering assistant control system). Another advantage of these techniques is that the coefficient of friction can be estimated without physical excitation, but they are not taking into account all the factors to provide an accurate estimation for the coefficient of friction, for example, knowledge about the tire: tire type, tire pressure, and so many more aspects are not utilized.

Effect-based techniques provide information resulting from the response of the system to different road conditions. For example, Umeno et al. in [9], proposed a tire vibration model (shown in Figure 1.2), that monitors the longitudinal velocity of the tires to estimate the tire-road friction. The frequency characteristics of the wheel speed is measured, then the coefficient of friction is estimated online, using recursive least squares method. The technique is applicable for rolling tires, but in this thesis, tires are investigated with

Category	Working principle	Advantages	Drawbacks
Cause-based	Image recognition	Can predict the friction properties ahead	Bad lighting decreases reliability
Cause-based	Easy to implement	Based on ambient temperature	Only gives a warning
Effect-based	Vibration model	No special sensors needed	High frequency noises
Effect-based	Vehicle dynamical calculations	Easy implementation to ADAS	No drawbacks
Effect-based	Based on self-aligning torque	Easy implementation to EPAS	No drawbacks

Table 1.1: Summarized estimation methods for the coefficient of friction, that can be found in the literature.

zero longitudinal motion, therefore this method could not be applied. Apart from that, this method suffers from high frequency noises.

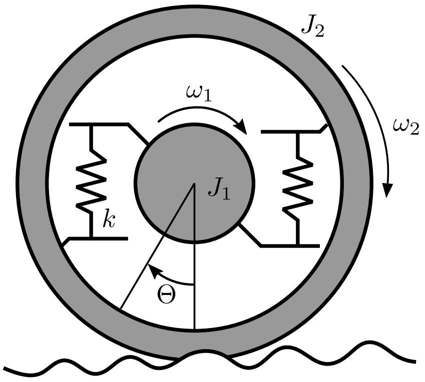

Figure 1.2: The vibration model proposed in [9].

Calculations based on vehicle dynamics can also provide an estimation of the coefficient of friction. For example, larger slip angle occurs on slippery roads (e.g. on ice), than during normal operation. Estimation techniques based on vehicle dynamics usually measure yaw rate, lateral acceleration, and vehicle speed. Most researchers focus on describing the lateral dynamics of the vehicle by using some kind of vehicle model, while the friction forces are taken into account by using a tire model. Hahn, Rajamani and Alexander developed a method for tire-road friction coefficient estimation that calculates the lateral dynamics of the car by processing GPS (global positioning system) signals. The parameters of the tire are calculated real-time by using the so-called tire brush model, then the coefficient of friction was expressed as a function of slip angle, normal force and cornering stiffness. Also based on vehicle dynamical approaches, Ray proposed a Kalman-Bucy filter and Bayesian hypothesis selection to estimate the state and tire forces of an eight-degree-of-freedom vehicle model [10]. The technique is based on inertial sensor data and after the parameter and state estimation, the coefficient of friction is calculated based on a statistical model using the maximum likelihood method. Although the estimation of friction properties based on vehicle dynamical approaches is an interesting and promising field of research, in this thesis, the goal is to provide an estimation algorithm for vehicles with zero longitudinal velocity, therefore these methods could not be applied.

Along with vehicle dynamical measurement signals, the self-aligning torque of tires is recently used in the control schemes of some driver assistant systems. Electronic power-assisted steering (EPAS) made the real-time calculation of the self-aligning torque possible. Previously both Mitsubishi [11] and Toyota [12] released publications about calculating the self-aligning torque based on available signals of the EPAS system. However friction estimation methods based on the self-aligning torque often assume moving vehicles and the states are estimated with the help of a vehicle model, for example, Ahn, Peng and Tseng proposed a method, where the coefficient of friction is estimated using the self-aligning torque of the tire [6], but during the process, non-zero longitudinal velocity was assumed, therefore this technique could not be applied in this thesis.

The found methods either used signals, that were unavailable in the investigated case or were not derived for cases with zero longitudinal velocity, therefore it was necessary to develop a new estimation process. In this thesis, the possible approximations of the coefficient of friction are examined based on only monitoring the lateral dynamics of elastic tires with no longitudinal motion. I would like to emphasize that this thesis is built on a previous paper [13], that has been registered to the Students' Scientific Conference (TDK) at the Budapest University of Technology and Economics.

2 Modeling and simulation of the investigated mechanical system

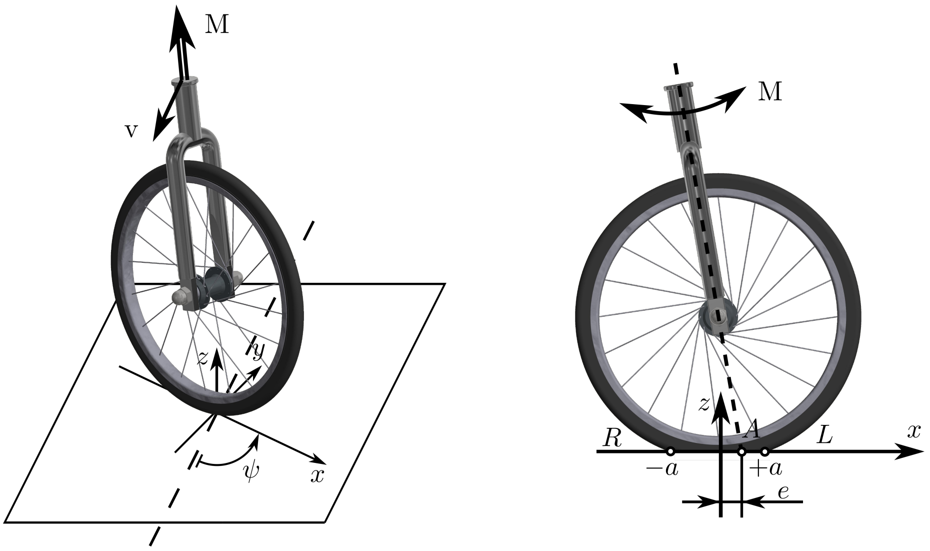

Figure 2.1: Axonometric (left) and side (right) view of the caster-wheel system.

To investigate the tire-ground contact, we use the so-called towed wheel model. In Figure 2.1, the mechanical system is illustrated with the coordinate system and some of the geometrical parameters. In order to describe the tire deformation, the (x, y, z) coordinate system is used. Its origin is fixed to the center of the tire-ground contact patch, while the x and y axes are aligned to the longitudinal and lateral directions of the wheel, respectively. The z-axis is normal to the plane of the ground.

In the side view of the mechanical system (right panel of Figure 2.1), the most relevant geometrical parameters regarding the elastic tire are highlighted. The length of the contact patch is denoted by $2a$. The endpoints of the contact region, where $x = a$ are called the leading edge (L), and the $x = -a$ points are called the rear edge (R). The system is actuated with the steering torque $\mathbf{M}$ as shown in Figure 2.1.

In the right panel of Figure 2.1, the axis of revolution is illustrated with a dotted line. The point, where this line crosses the x-axis, is defined as point A. The distance between the center point of the contact patch and the point A is called caster length (or trail) and is denoted by e. The mass moment of inertia of the steered caster-wheel system with respect to kingpin axis is considered.

In this work, only the quasi-static case is modeled, where the longitudinal velocity of the system is zero ($\mathbf{v} = \mathbf{0}$) and the rotational motion of the wheel is described by steering angle (or yaw angle) $\psi(t)$, which motion induces the deformation of the tire.

2.1 The brush tire model

There are different approaches to model the tire-road relationship. Starting from the 1940s, the vehicle industry showed more and more interest in tire modeling, therefore the first mechanical models were introduced in that time period [1]. Later on, researchers focused more on finding empirical formulas that describe the tire forces. Nowadays, with the advanced computation efforts, combined tire models are being introduced, using both physical models and empirical formulas, moreover finite element methods are used to validate these modern theories.

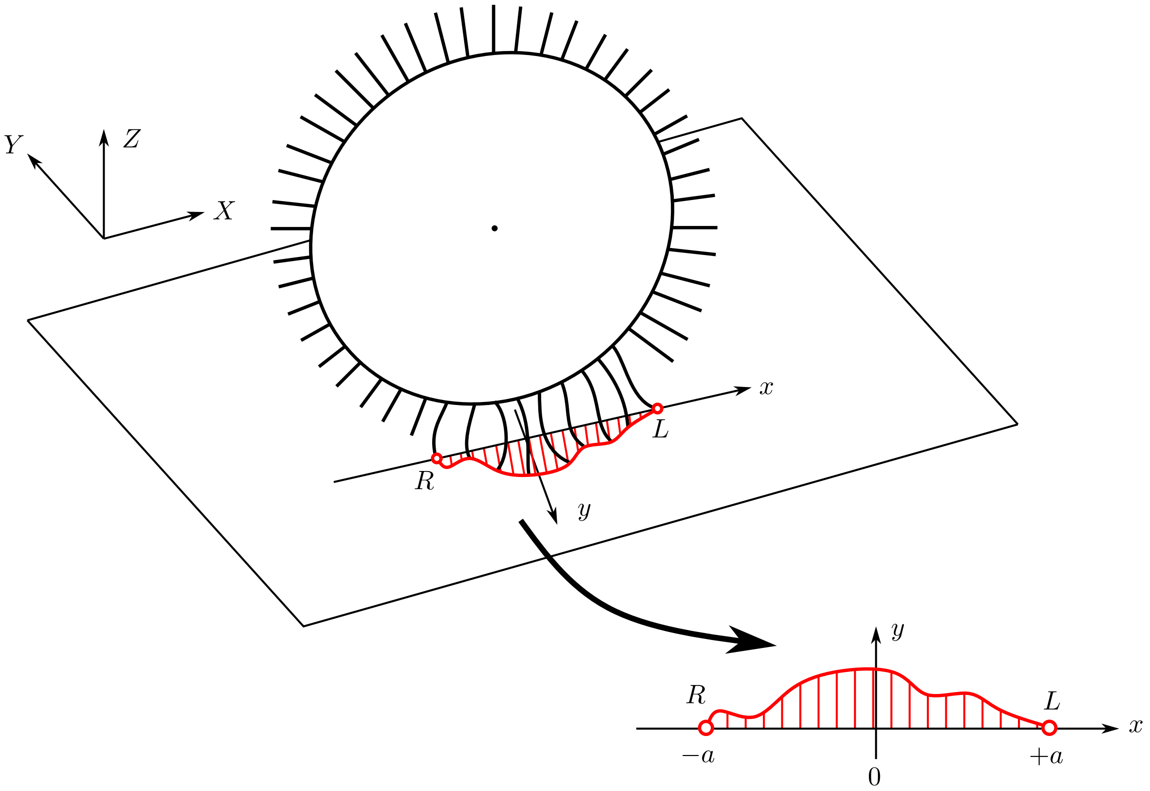

Figure 2.2: Schematic view of the brush tire model. The leading edge is noted by L and the rear edge by R. The in-plane deformation within the contact patch is also illustrated.

For the investigations, the brush tire model was selected [2], which is a popular analytical approach to model torques and forces resulting from the deformation of tires. Although more complex, thus more accurate analytical models can be found in the literature (e.g. the stretched string model [14]), the brush model is simple enough to develop a real-time estimation method for the coefficient of friction based on the equations that can be derived from this model. The main advantage of analytic approaches is that they are based on physical principles, therefore no experimental data is needed to describe the system. The schematic view of the brush tire model can be seen in Figure 2.2. The model consists of tread elements (also called bristles) connected to the carcass. The carcass is represented as a rigid disk. The thread elements are modeled as linear springs and their deformation are independent from each other, therefore outside of the contact patch, zero deformation can be assumed.

An in-plane model of the brush model can be defined, where the deformation of the elastic bristles are calculated in the $x - y$ plane, as shown in Figure 2.2 and 2.3. Inside the contact patch, the deformation is limited by the available friction between the treads and the road surface. Assuming parabolic normal force distribution (which assumption was proven by measurements in [15]) in the contact region, the limit of the deflection (q_{cr}) is also parabolic

$$q_{cr}^{\pm} = \pm \frac{3F_N\mu}{4a^3k}\left(a^2 - x^2\right), \tag{2.1}$$

where F_N is the normal force, μ is the coefficient of friction, and k [N/m^2] is the distributed lateral stiffness of the elastic bristles (it is assumed to be homogeneous around the carcass).

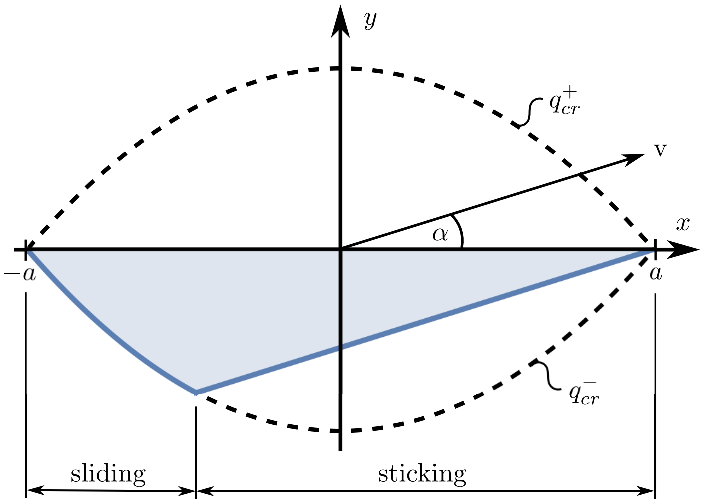

Figure 2.3: In-plane model of the tire brush model, in case of non-zero longitudinal velocity.

Originally, the brush tire model was developed to model tire forces in case of non-zero longitudinal vehicle velocity. In this work, the concept is used to model tire deformations in a quasi-static case, where the longitudinal speed is assumed to be zero. In Figure 2.3, the deformation of an elastic tire is illustrated by the original idea with non-zero longitudinal speed. The sliding and sticking regions within the contact patch are also shown in Figure 2.3. Tire elements enter the contact patch at the leading edge L with zero deformation. In the quasi-stationary case, the brush elements start to be deformed according to the side slip angle α, which measures the angle of the wheel center point velocity relative to the wheel center plane. When the deformation of an element reaches the limit of deflection, it enters the sliding zone, and their deformation is limited by the above defined q_{cr}. In the sticking region, the deformation of the bristles can be described as $q_r(x) = \tan\alpha \cdot (x - a)$. It is important to emphasize that q_r is only valid in this particular case, later on the accurate deformation functions will be derived. In an arbitrary position x, the deformation of the tread elements (q) can be expressed as

$$q(x) = \begin{cases} q_{cr}^{-}, & \text{when sliding,} \\ q_r, & \text{when sticking.} \end{cases} \tag{2.2}$$

The deformation of the elements causes a torque, namely the self-aligning torque, that acts against the steering torque. Assuming the deformation function is known for $t \in [t_0,\, t_{\text{end}}]$, the self aligning torque can be expressed as

$$M_z(t) = \int_{-a}^{a} k \cdot q(x,t) \cdot (x - e)\, \mathrm{d}x\,. \tag{2.3}$$

2.2 Numerical simulations based on the brush model

For the investigation of the tire-ground relation, a simulation environment was set up based on the brush model. Based on Figure 2.4, let us consider an arbitrary point P in the sticking region. The wheel is towed by the rigid caster with constant (zero) velocity in the X direction. The lateral deformation of the tire can be described with the $q(x,t)$ function. It is known that the kinematic constraint of sticking requires the absolute velocity to be zero, therefore $\mathbf{v}_P = \mathbf{0}$.

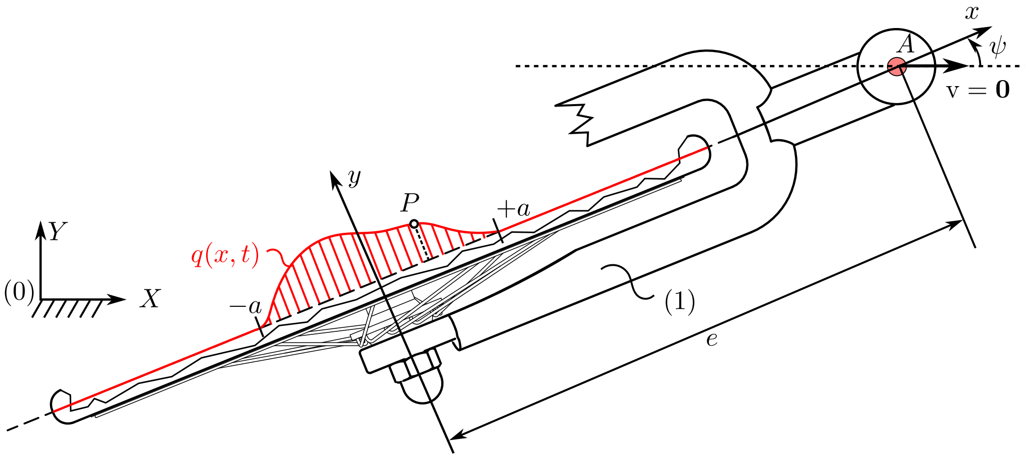

Figure 2.4: Illustrating the mechanical system for deriving the equation for the kinematic constraint of sticking.

Using the notations of relative kinematics

$$\mathbf{v}_{P20} = \mathbf{v}_{P10} + \mathbf{v}_{P21}, \tag{2.4}$$

where $\mathbf{v}_{P20}$ is the absolute velocity of point P, $\mathbf{v}_{P10}$ is the carrier velocity and $\mathbf{v}_{P21}$ is the relative velocity.

The absolute velocity of the carcass, or in other words, the carrier velocity of the tire, can be expressed as

$$\mathbf{v}_{P10} = \mathbf{v}_{A10} + \omega_{10} \times \mathbf{r}_{AP}. \tag{2.5}$$

Since the towing speed is zero in our study, therefore $\mathbf{v}_{A10} = \mathbf{0}$. As a result, $\mathbf{v}_{P10}$ can be expressed in the $(x,\, y,\, z)$ coordinate system as

$$\mathbf{v}_{P10} = \begin{bmatrix} 0 \\ 0 \\ \dot{\psi} \end{bmatrix} \times \begin{bmatrix} -(e - x) \\ q(x,t) \\ 0 \end{bmatrix} = \begin{bmatrix} -q(x,t) \cdot \dot{\psi} \\ -(e - x) \cdot \dot{\psi} \\ 0 \end{bmatrix} \tag{2.6}$$

The relative velocity between the tire and the carcass can be attained by the time derivation of the relative position vector $\mathbf{r}_{P21}$, as

$$\frac{\mathrm{d}}{\mathrm{d}t}\mathbf{r}_{P21} = \frac{\mathrm{d}}{\mathrm{d}t}\begin{bmatrix} x \\ q(x,t) \\ 0 \end{bmatrix} = \begin{bmatrix} \dot{x} \\ \dot{q}(x,t) + q'(x,t)\cdot\dot{x} \\ 0 \end{bmatrix}, \tag{2.7}$$

where $\dot{\square}$ notes the partial derivative with respect to time and $\square'$ notes the partial derivative with respect to coordinate x. Thus the time derivative of $q(x,t)$:

$$\frac{\mathrm{d}}{\mathrm{d}t}q(x,t) = \underbrace{\frac{\partial}{\partial t}q(x,t)}_{\dot{q}(x,t)} + \underbrace{\frac{\partial q(x,t)}{\partial x}}_{q'(x,t)} \cdot \underbrace{\frac{\partial x}{\partial t}}_{\dot{x}}\,. \tag{2.8}$$

From (2.7), the kinematic constraint equations of sticking can be expressed as

$$-\,q(x,t)\cdot\dot{\psi} + \dot{x} = 0, \tag{2.9}$$

$$-\,(e-x)\cdot\dot{\psi} + \dot{q}(x,t) + q'(x,t)\cdot\dot{x} = 0, \tag{2.10}$$

where $x \in [-a,\, a]$, assuming the whole contact region is sticking.

From (2.9), the translational velocity can be determined:

$$\dot{x} = q(x,t)\cdot\dot{\psi}(t). \tag{2.11}$$

From (2.10), the differential equation for the lateral deformations of the elastic tire elements can be expressed as

$$\dot{q}(x,t) = (e-x)\cdot\dot{\psi}(t) - q'(x,t)\cdot q(x,t)\cdot\dot{\psi}(t), \tag{2.12}$$

where the last term is nonlinear. Considering small deformations and motions, it represents a third-order small term that can be neglected in the analysis.

The equation of motion for the caster-wheel system can be expressed using Newton's second law, as

$$J_A\ddot{\psi}(t) = -b_t\dot{\psi}(t) - M_z(t) + M(t), \tag{2.13}$$

where J_A is the mass moment of inertia with respect to point A, b_t is the torsional damping of the kingpin, M_z is the self-aligning torque of the tire and M is the steering torque.

The governing equation of the system consists of the integro-differential equation (2.13), where the self-aligning moment can be calculated by (2.3), while the lateral deformation is described by the partial differential equation (2.12). Moreover, the sliding in the contact patch is also considered since the deformation is maximized within the contact patch based on (2.1). The equations necessary for the numerical simulation can be summarized as

$$J_A\ddot{\psi}(t) = -b_t\dot{\psi}(t) - \int_{-a}^{a} k\cdot q(x,t)\cdot(x-e)\,\mathrm{d}x + M(t), \tag{2.14}$$

$$\dot{q}(x,t) \approx (e-x)\cdot\dot{\psi}(t), \tag{2.15}$$

$$|q(x,t)| \leqslant \frac{3F_N\mu}{4a^3k}\left(a^2 - x^2\right),\ \forall\, t \in [t_0,\, t_{\mathrm{end}}]\,. \tag{2.16}$$

2.3 Results of simulation

For the numerical simulations, the steering torque input has to be defined by the user. The parameters used in the simulations are summarized in Table 2.1.

Parameter	Notation	Value
Caster length (trail)	e	0.01 m
Contact patch half-length	a	0.02 m
Lateral tire stiffness	k	60000 N/m^2
Mass moment of inertia with respect to A	J_A	0.1 kgm^2
Torsional damping	b_t	0.4827 Nms
Vertical tire load	F_N	180 N
Coefficient of friction	μ	0.5

Table 2.1: List of parameters used in the numerical simulations.

The simulation was set up to calculate the deformation of the contact patch at every time step, and after the simulation procedure, an animation shows the results. An example steering torque input is shown in Figure 2.5, with the time instants, for which the deformation function $q(x, t)$ is illustrated in Figure 2.6.

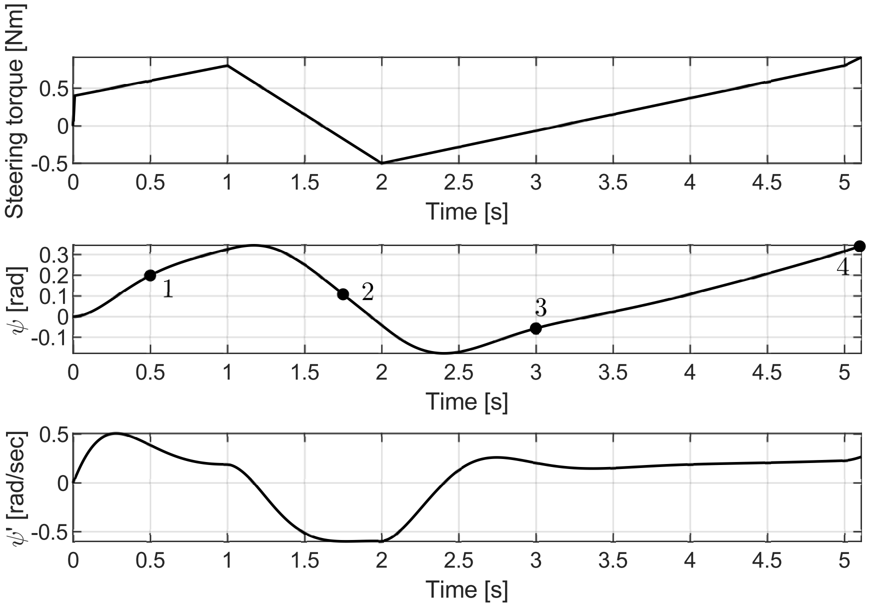

Figure 2.5: Results of the numerical simulation, regarding the yaw angle, angular velocity, and steering torque.

It is visible in Figure 2.5, that there was a direction change in the angular motion at about $t = 1.25$ s, and then at $t = 2.4$ s. In Figure 2.6 the first deformation function is shown at $t = 0.5$ s, where three fragmentation zones appear in the contact patch. Then after the first direction change, at $t = 2.75$ s it is shown that five zones are present in the contact patch. Between the first and second direction change, the tire was not steered enough to terminate the fourth and fifth zones, therefore after the second change of rotational direction, another two deformation zones are generated, as it is shown at $t = 3$ s. Then the tire is turned continuously in the same direction, hence by the end of the simulation, only three fragmentation zones remain, as it is illustrated at $t = 5.1$ s.

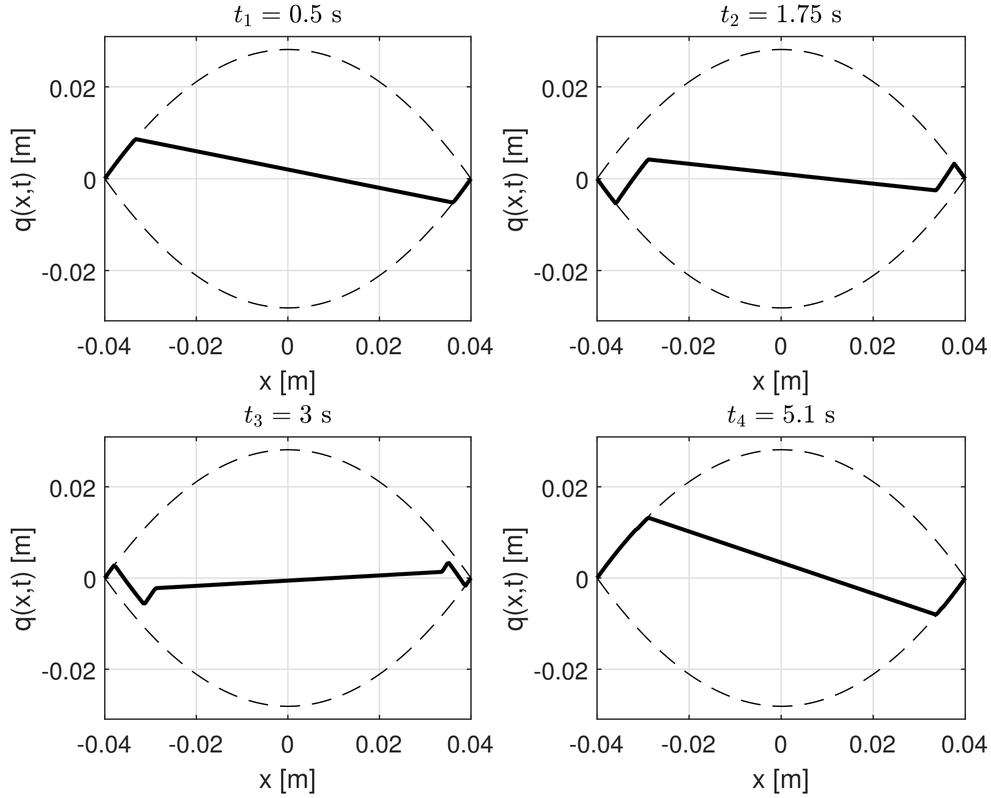

Figure 2.6: The deformation function of the center-line of the tire, illustrated at the given time instants.

The above discussed simulation environment made it possible to test the later derived friction estimation methods. The calculation procedure was later implemented into the simulation scripts, therefore it is possible to compare the identified coefficient of friction with the simulation values, within the simulation tool.

3 Estimation of the coefficient of friction based on the brush tire model

Three methods are being derived for estimating the coefficient of friction between the tire and the ground. The first method is based on an analytic tire model - namely the previously introduced brush tire model. The second method is based on a neural network machine learning algorithm, therefore the coefficient of friction is estimated by data-driven modeling, and the knowledge about the physical system is neglected. The third algorithm incorporates the principle of the previous two, besides calculating from the physical model of the system, the unmodeled effects are compensated with a machine learning technique.

In the previous section, the brush tire model was introduced in order to model the self-aligning torque resulting from the deformation of the tire. Although the method was originally developed for vehicles with longitudinal motion, the principle of the mechanical model remains the same, when the wheel is standing still and the only actuation is the steering torque.

The principle of the estimation method is based on (2.14). Assuming $\dot{\psi}(t)$, $\ddot{\psi}(t)$, $M(t)$ can be measured and J_A, k, b_t, a, e constants are known, the only unknown in the equation of motion is the deformation function of the contact line. It was previously discussed that the deflection of the elastic elements is dependent on the coefficient of friction between the ground and the tire. Assuming $q(x,t)$ can be expressed as a function of the friction coefficient and known or measured physical properties, μ could be calculated theoretically. In the following chapter, this method will be derived, later on, it will be tested with simulated and measured signals.

3.1 Analytical approximation for the contact line deformation function

From (2.14), it is clear that the first task is to express the deformation function with the coefficient of friction. From now on, at $t = 0$ s zero deformation will be assumed and in general, the angular rotation will begin with a positive direction. From Figure 2.1 it is visible that point A is on the axis of rotation, therefore zero deformation will occur at that point. In the sticking region, the tread elements will remain in the same position in the ground-fixed reference frame, but in the caster-fixed (x, y, z) system they will be revolved with ψ angle around A. And when the deformation reaches q_{cr}, then it will be limited by the available frictional forces.

From Figure 3.1, it is visible, that the deformation function of this type can be expressed

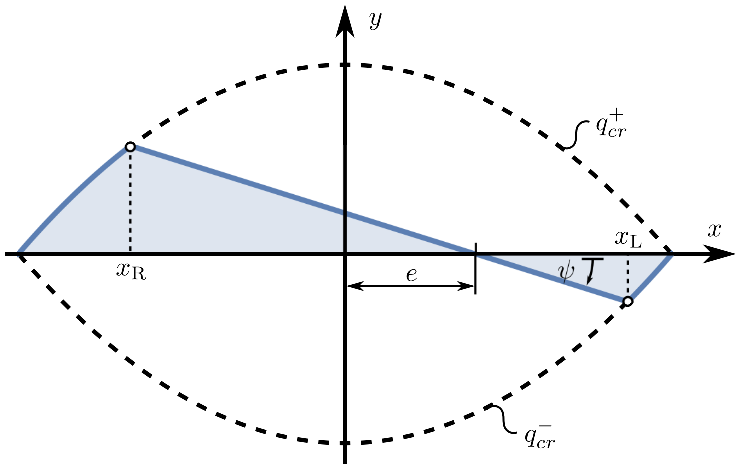

Figure 3.1: In-plane brush model representation of the tire elements deformation. Three distinct zones can be visibly identified, therefore three different equations are needed to describe the deformation function.

as

$$q(x) = \begin{cases} \dfrac{3\,F_{\mathrm{N}}\,\mu}{4\,a^3\,k} \cdot (a^2 - x^2)\,, & \text{if } x \in [-a,\, x_{\mathrm{R}}), \\ -\tan\psi \cdot (x - e)\,, & \text{if } x \in [x_{\mathrm{R}},\, x_{\mathrm{L}}), \\ \dfrac{-3\,F_{\mathrm{N}}\,\mu}{4\,a^3\,k} \cdot (a^2 - x^2)\,, & \text{if } x \in [x_{\mathrm{L}},\, a], \end{cases} \tag{3.1}$$

where x_{R} and x_{L} are the points, where the sticking turns into sliding as a result of reaching the critical deformation limit. The values of these variables can be calculated analytically by solving simple algebraic equations, which can be found in the Appendix.

Equation (3.1) is only valid for deformations, where only three sections are generated by the angular motion and the direction of the revolution is positive at the beginning. For negative directions with three deformation zones, a similar expression can be derived. For the sticking region, the deformation can be characterized with the same function as before, but it will reach the deformation limits at different points, therefore

$$q(x) = \begin{cases} \dfrac{-3\,F_{\mathrm{N}}\,\mu}{4\,a^3\,k} \cdot (a^2 - x^2)\,, & \text{if } x \in [-a,\, x_{\mathrm{R}}), \\ -\tan\psi \cdot (x - e)\,, & \text{if } x \in [x_{\mathrm{R}},\, x_{\mathrm{L}}), \\ \dfrac{3\,F_{\mathrm{N}}\,\mu}{4\,a^3\,k} \cdot (a^2 - x^2)\,, & \text{if } x \in [x_{\mathrm{L}},\, a] \end{cases} \tag{3.2}$$

deformation function can be derived. Thus, in general, when three deformation zones are expected, the analytical formula for the contact line deformation can be expressed as

$$q(x) = \begin{cases} \operatorname{sgn}(\psi)\,\dfrac{3\,F_{\mathrm{N}}\,\mu}{4\,a^3\,k} \cdot (a^2 - x^2)\,, & \text{if } x \in [-a,\, x_{\mathrm{R}}), \\ -\tan\psi \cdot (x - e)\,, & \text{if } x \in [x_{\mathrm{R}},\, x_{\mathrm{L}}), \\ -\operatorname{sgn}(\psi)\,\dfrac{3\,F_{\mathrm{N}}\,\mu}{4\,a^3\,k} \cdot (a^2 - x^2)\,, & \text{if } x \in [x_{\mathrm{L}},\, a], \end{cases} \tag{3.3}$$

where sgn notes the signum function.

With the numerical simulation, that was introduced in section 2.2, it is possible to test, whether the above described formulas are correct or not. In our analysis, we consider that both the deformations and the angle ψ are small, hence the sticking part can be linearized:

$$q(x) = \begin{cases} \operatorname{sgn}(\psi)\,\dfrac{3\,F_\mathrm{N}\,\mu}{4\,a^3\,k}\cdot(a^2-x^2)\,, & \text{if } x\in[-a,\,x_\mathrm{R}),\\ -\psi\cdot(x-e)\,, & \text{if } x\in[x_\mathrm{R},\,x_\mathrm{L}),\\ -\operatorname{sgn}(\psi)\,\dfrac{3\,F_\mathrm{N}\,\mu}{4\,a^3\,k}\cdot(a^2-x^2)\,, & \text{if } x\in[x_\mathrm{L},\,a]. \end{cases} \tag{3.4}$$

The linearization caused small errors compared to the simplifications made during the model creation, therefore it was decided to calculate with the linearized equations from now on. In Figure 3.2, it is shown that the previously derived analytical functions are able to accurately describe the deflection of the contact line if the deformation function has only three zones.

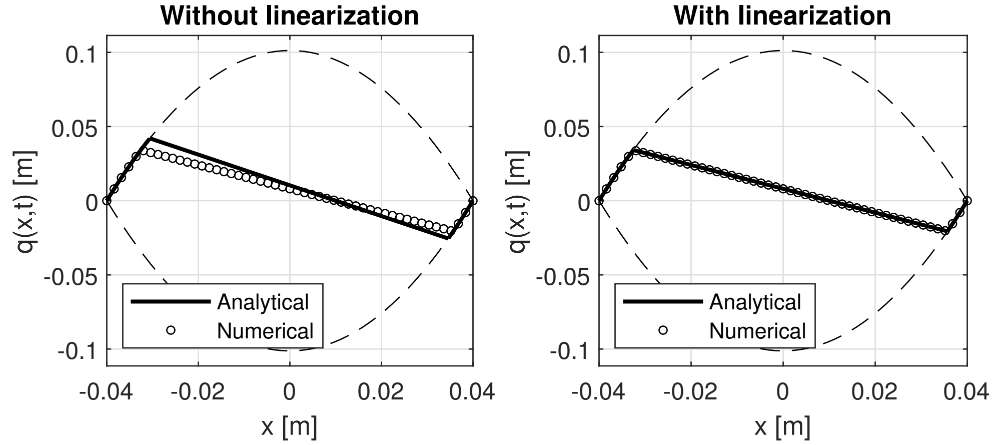

Figure 3.2: Analytical deformation functions compared to results obtained by numerical simulation at a given time-step. On the left, the nonlinear form can be seen. On the right the results after linearization are visible.

From Figure 2.6, it can be seen, that more than three deflection zones can occur in the contact line of an elastic tire. For example, when the direction of rotation is changed, the thread elements, that are in the sliding region can revolve back into the sticking region. As a result, in the deformation function parabolic sections appear, which are revolved around point A. An example of a deformation function with such zones can be found in Figure 3.3.

Let us suppose that three deflection zones are present in the contact patch. At a given time step, the direction of the rotation is changed from positive to negative direction. At that given time, the yaw angle is defined as ψ_max, thus the deformation function can be

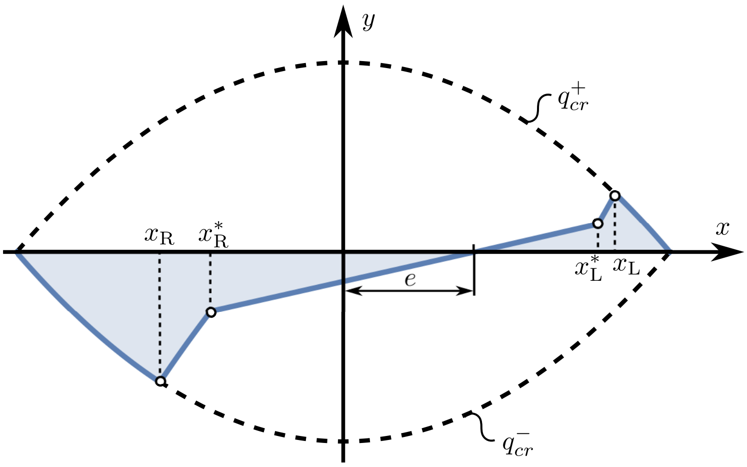

Figure 3.3: In plane model showing five deformation zones. The limits of each section are noted in the figure with the appropriate notation, also used in the equations.

expressed as

$$q(x) = \begin{cases} \dfrac{-3\,F_{\mathrm{N}}\,\mu}{4\,a^3\,k}\,\left(a^2 - x^2\right), & \text{if } x \in [-a,\, x_{\mathrm{R}}), \\ \dfrac{3\,F_{\mathrm{N}}\,\mu}{4\,a^3\,k}\,\left(a^2 - x^2\right) + m_{\mathrm{R}}\,x - m_{\mathrm{R}}\,e & \text{if } x \in [x_{\mathrm{R}},\, x_{\mathrm{R}}^{*}), \\ -\psi\,\left(x - e\right), & \text{if } x \in [x_{\mathrm{R}}^{*},\, x_{\mathrm{L}}^{*}), \\ \dfrac{-3\,F_{\mathrm{N}}\,\mu}{4\,a^3\,k}\,\left(a^2 - x^2\right) + m_{\mathrm{L}}\,x - m_{\mathrm{L}}\,e & \text{if } x \in [x_{\mathrm{L}}^{*},\, x_{\mathrm{L}}), \\ \dfrac{3\,F_{\mathrm{N}}\,\mu}{4\,a^3\,k}\,\left(a^2 - x^2\right), & \text{if } x \in [x_{\mathrm{L}},\, a], \end{cases} \tag{3.5}$$

where x_{R}^{*} and x_{L}^{*} are the point of the contact line, where the linear deformation zone crosses the rotated parabolic zones. The rotated parabolas can be calculated as the addition of the parabolic limits of deflection and linear functions that can be parameterized with m_{L} and m_{R}. The values of x_{R}^{*} and x_{L}^{*} can be obtained by calculating x_{R} and x_{L} for $\psi_{\max}$ for three deflection zones (equation (3.4)). Then the values of m_{R}, m_{L}, x_{R} and x_{L} can be obtained by solving simple algebraic equations. The derived analytic formulas can be found in the Appendix.

Similarly to Figure 3.2, the above described formulas can be compared to the numerical results. In Figure 3.4 the analytical results are shown next to the numerical deformation values and it is visible that the analytically derived formulas are able to accurately describe the deflections that occur in the contact patch.

The same principle can be used, when the angular direction changes from negative to positive. Three deflection zones turn into five zones, and the deformation function can be

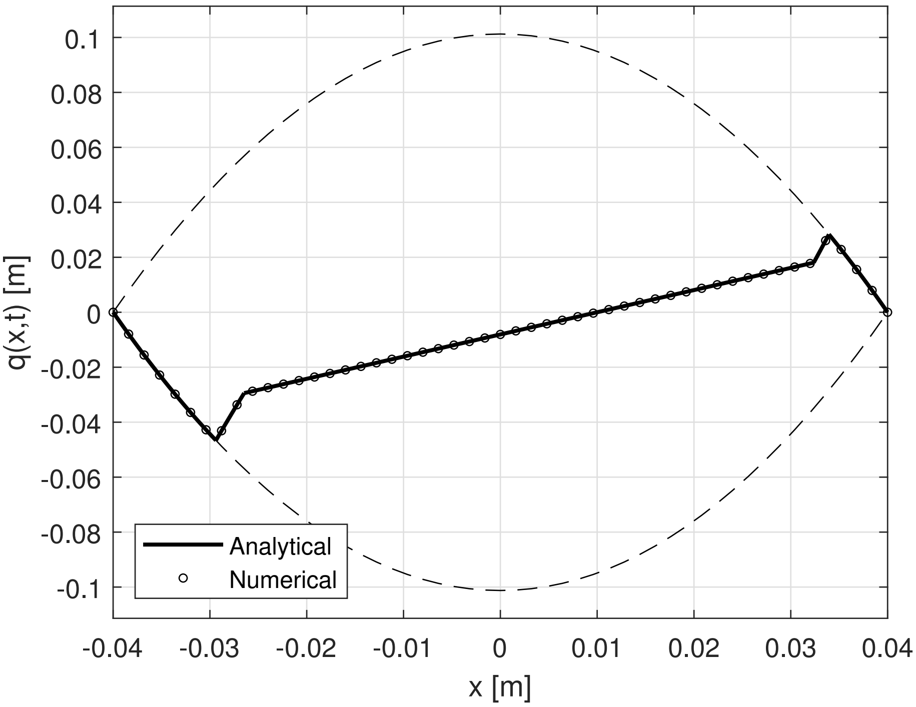

Figure 3.4: Comparing the analytical deformation function with the results obtained by numerical simulation.

expressed as

$$q(x) = \begin{cases} \dfrac{3\,F_{\mathrm{N}}\,\mu}{4\,a^3\,k}\,(a^2 - x^2)\,, & \text{if } x \in [-a,\, x_{\mathrm{R}}), \\ \dfrac{-3\,F_{\mathrm{N}}\,\mu}{4\,a^3\,k}\,(a^2 - x^2) + m_{\mathrm{R}}\,x - m_{\mathrm{R}}\,e, & \text{if } x \in [x_{\mathrm{R}},\, x_{\mathrm{R}}^*), \\ -\psi\,(x - e)\,, & \text{if } x \in [x_{\mathrm{R}}^*,\, x_{\mathrm{L}}^*), \\ \dfrac{3\,F_{\mathrm{N}}\,\mu}{4\,a^3\,k}\,(a^2 - x^2) + m_{\mathrm{L}}\,x - m_{\mathrm{L}}\,e, & \text{if } x \in [x_{\mathrm{L}}^*,\, x_{\mathrm{L}}), \\ \dfrac{-3\,F_{\mathrm{N}}\,\mu}{4\,a^3\,k}\,(a^2 - x^2)\,, & \text{if } x \in [x_{\mathrm{L}},\, a], \end{cases} \tag{3.6}$$

where m_{R}, m_{L}, x_{R}, x_{L}, x_{R}^* and x_{L}^* can be calculated similarly as before. The exact analytical formulas can be found in the Appendix.

A similar process can be observed if five deformation zones are present in the contact line and a direction change occurs in the angular motion. As a result, more rotated parabolic zones are generated in the sticking region, but the effect of those deformation zones is assumed to be negligible, therefore it was not modeled in this work.

Although previously only those cases were discussed, when more and more zones are generated in the deformation function of the contact line, in other words, fragmentations are created with the change of angular direction. The moment when this happens, the yaw angle was defined to be $\psi_{\max}$. When the yaw angle's absolute value exceeds $\psi_{\max}$ ($\psi > -\psi_{\max}$), the fragmented zones reach q_{cr} limit of deflection, therefore the fragmentation disappears. The process of the deformation modeling is summarized with a state machine, and it is illustrated in Figure 3.5.

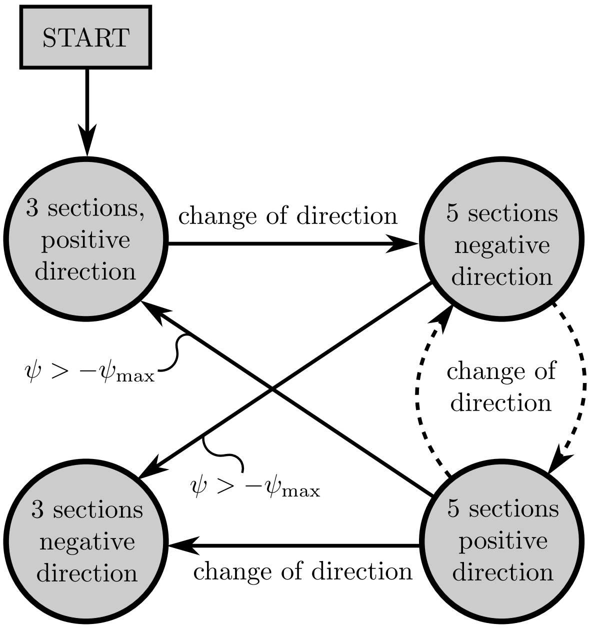
START
3 sections, positive direction
change of direction
5 sections negative direction
$\psi > -\psi_{\max}$
change of direction
$\psi > -\psi_{\max}$
3 sections negative direction
change of direction
5 sections positive direction

Figure 3.5: State machine representation of the approximation process for the deformation function. The dotted line represents the neglected seven zone fragmentation, which is not a true analytical description, but an assumption.

The state machine in Figure 3.5 is suitable for illustrating the deformation function's analytical approximation, but the scheme was also applied in the simulation environment - presented in section 2.2 - and an animation function was programmed to be able to examine the numerically simulated and the analytically calculated deformations through the simulation time interval.

3.2 Estimation method for the coefficient of friction

After describing the deformation function $q(x,t)$ in the previous subsection, now all the terms are known in the equation of motion - equation (2.14). The expressions for the deformation contain known or observable physical quantities, only the coefficient of friction remains unknown. The definite integral in the equation of motion can be evaluated analytically, because the deformation function is known, if the yaw angle is measured and the history of measurements is stored (the "memory effect" of an elastic tire is considered), an algebraic equation can be formed for the coefficient of friction, as

$$f(\mu) := -J_A\,\ddot{\psi}(t) - b_{\mathrm{t}}\,\dot{\psi}(t) + M(t) - \int_{-a}^{a} k\,q(x,t)\,(x-e)\,\mathrm{d}x = 0, \tag{3.7}$$

where $f(\mu)$ is defined as the algebraic expression (which equals zero), that needs to be solved in order to acquire the value of the coefficient of friction. This function cannot be solved analytically, but it is possible to solve it with numerical schemes. The chosen numerical solver was the built-in `fsolve` function of Matlab [16], using a trust region algorithm.

As previously discussed, with the help of the created simulation environment, it is possible to test the developed estimation algorithm. The mechanical system was simulated with the physical properties summarized in Table 3.1, then the coefficient of friction can be calculated for each time step.

Parameter	Notation	Value
Towing length	l	0.01 m
Contact patch half-length	a	0.04 m
Lateral tire stiffness	k	60000 N/m^2
Mass moment of inertia with respect to joint A	J_A	0.1 kgm^2
Torsional damping	b_t	0.4827 Nms
Vertical tire load	F_N	180 N
Coefficient of friction	μ	0.5

Table 3.1: List of parameters used in the numerical simulations for testing the developed estimation algorithm.

In order to test whether the equation for the coefficient of friction (Eqn. (3.7)) is correct, first the value of μ was provided to the algorithm, but the yaw angle was not, therefore the output of the numerical solver was the estimation for ψ. The results can be seen in Figure 3.6. The test was successful, therefore equation (3.7) can be considered accurate. It is now visible that the estimation algorithm can accurately identify the yaw angle. However, ψ can be measured easily, on the other hand, the calculation method used the value of the coefficient of friction, which can not be observed.

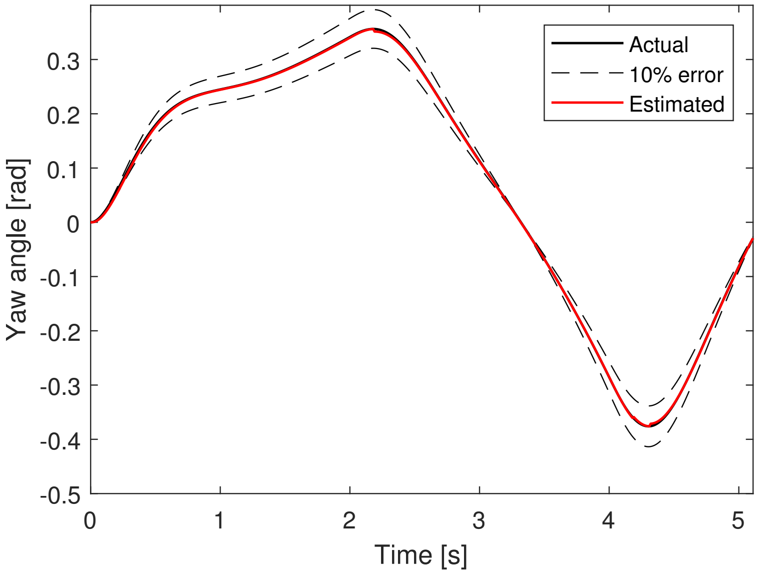

Figure 3.6: Estimating the yaw angle, with the value of the coefficient of friction given to the algorithm. Except for small oscillations around the peaks of the true yaw angle function, no visible differences can be seen between the actual and the estimated signals.

The next step is to check, whether the developed estimation algorithm can identify the coefficient of friction correctly. In equation (3.7), after expressing the definite integral, the coefficient of friction appears in nonlinear terms, thus it is harder to solve the equation numerically for μ. With the same physical properties, the result of the estimation can be seen in Figure 3.7. The estimation process was also tested for simulation cases with $\mu = 1$ and $\mu = 1.8$, the figures illustrating the results can be found in the Appendix.

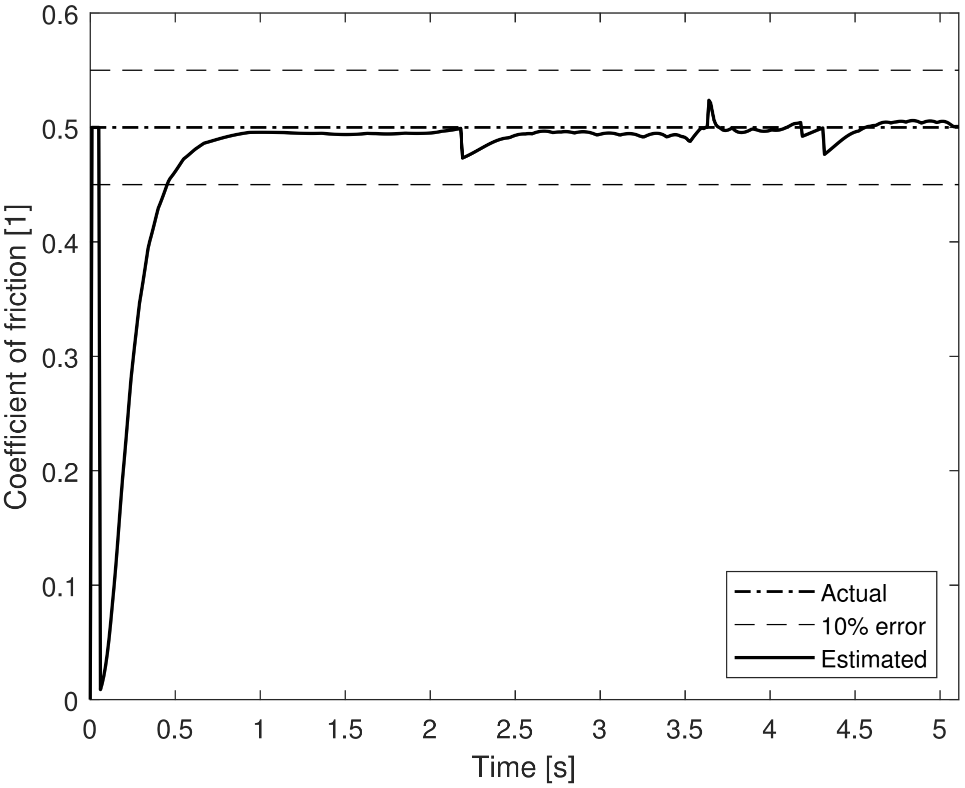

Figure 3.7: Estimation results for the coefficient of friction using simulated data sets.

In Figure 3.7 big errors are visible in the beginning (approx. until $t = 0.5$ s), but those errors can be explained with the small angle differences. In the beginning, only the two sliding ends of the contact line are dependent on the friction. When small angle differences occur, the terms that depend on the friction are so small, that it is hard for the numerical solver to accurately approximate the coefficient of friction. Apart from that, only small oscillations are visible, which occur when changing the direction of the angular motion. If five (or more) segmentation can be found in the contact region, the memory effect of the tires needs to be considered, therefore $f(\mu)$ depends on the local minima/maxima of the yaw angle (previously defined as $\psi_{\max}$). With the time discretization, the true local minimum or maximum cannot be determined, but only approximated, that is the reason for those errors.

Another problem occurred, which originates from the numerical precision of the calculation. In Figure 3.8, $f(\mu)$ is illustrated with the sought value of $f(\mu) = 0$. On the left, a "normal" case is visible, where the numerical solver had no problem with finding the appropriate solution. On the right side of the figure, a "problematic" case is visible. The function never reaches the value of zero, because of the numerical inaccuracies, therefore the solver approximates the solution with the point of the curve, which is nearest to the x-axis.

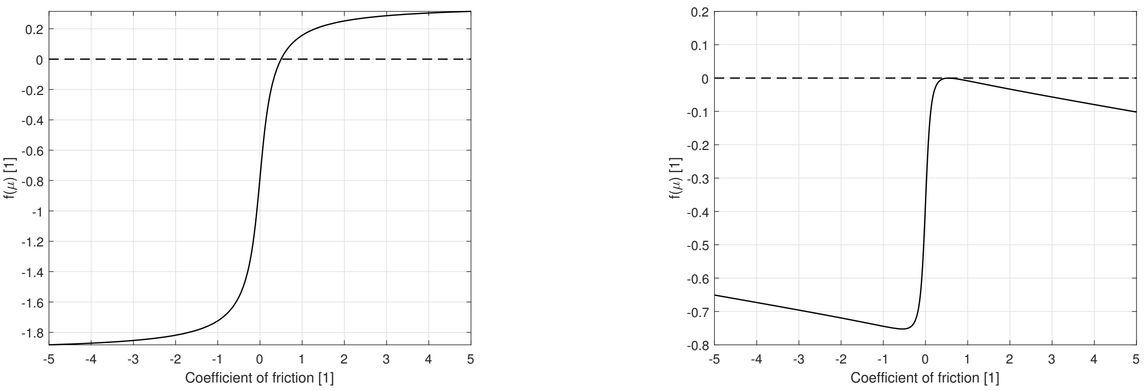

(a) Solving $f(\mu) = 0$ numerically, "normal" case.

(b) Solving $f(\mu) = 0$ numerically, "problematic" case.

Figure 3.8: Illustrating $f(\mu)$ at two different time instances. The dashed line represents the sought $f(\mu) = 0$ value.

After identifying all the causes of inaccuracies, the same graph as in Figure 3.7 is shown with the noted errors in Figure 3.9.

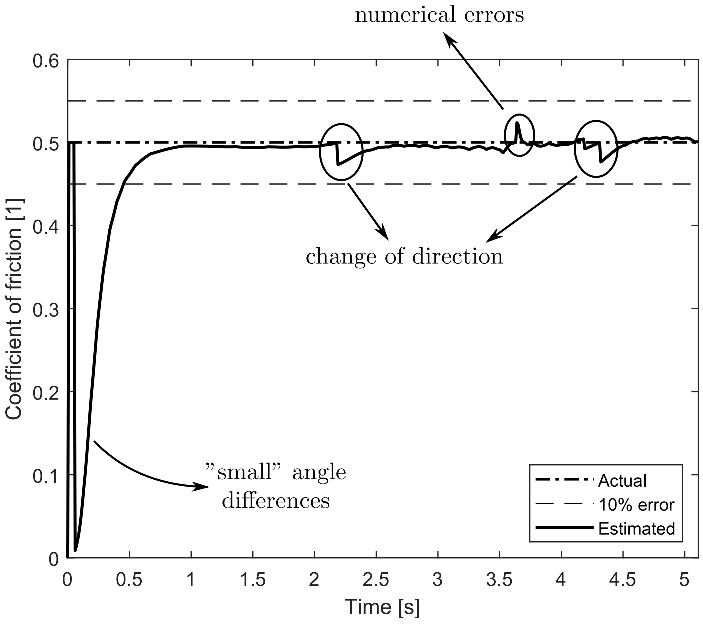

Figure 3.9: The results of the estimation showing the causes of inaccuracies.

Although the proposed estimation process has its limitations and some inaccuracies, it can estimate the coefficient of friction for simulated data sets. The biggest advantage of the method is that the results and the errors are easy to interpret, because the method is based on a physical model, and the equations are derived from physics-based expressions.

4 Estimation of the coefficient of friction using machine learning

4.1 Estimating with neural networks

4.1.1 A brief introduction to artificial neural networks

Nowadays, machine learning algorithms and artificial neural networks (ANNs, or just shortly NNs) are well-known terms for the majority of academic society. The idea of creating computational systems based on neurons in the human brain was first introduced about 60 years ago, but in the last 35-40 years, the usage of previously mentioned algorithms spread worldwide [17]. The main reason for the growing applications is that the growing computational power made it possible.

The most important property of ANNs is the capability to learn complicated connections between patterns from (measured) data. The main application fields are classification or regression tasks, moreover, predictions of time-series events are even possible. The usage of neural networks can be divided into two phases. First, during the learning phase, the final operation of the system is formed, by processing given data structures. During the second phase, the evolved working of the network can be utilized for the prescribed purpose [18].

The basic building blocks of neural networks are so-called neurons, which form layers within the network. The layers can be classified into three main classes, based on their positions in the network. The first layer is called the input layer, the last is the output layer, and all the other ones are called hidden layers. A typical representation of this structure can be seen in Figure 4.1. The duty of the input layer is to forward the incoming data, this layer does not take part in the processing of information. The output layer generates an output for each inherent neuron, therefore the number of neurons must match the output of the given task. The number of neurons in each layer and the connection between them can be modified almost arbitrarily.

The layers can also be classified based on their function. Layers are usually divided into categories based on their connection with other layers and how the output of the given layer is calculated. A few common examples are listed below.

- Dense layer: the output is calculated as the linear combination of the input and a constant weight vector.
- Recurrent layer: the layer receives some of the previously calculated outputs with the current input. The memory effect can be modeled this way.
- Convolutional layer: in contrast with the dense layer, the neurons inside a convolutional layer receive only a part of the input.

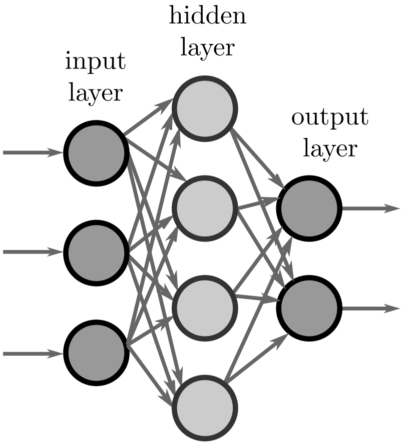

Figure 4.1: Representation of the layers in neural networks.

The connection between distinct layers is calculated with the help of weight vectors and activation functions. Let us consider a NN with L layers, then the output of an arbitrary k^{th} layer $(1 < k < L)$ can be expressed as

$$\mathbf{y}_{\mathrm{k}} = \mathbf{h}_{\mathrm{act,k}} \left(\mathbf{W}_{\mathrm{k}} \cdot \mathbf{y}_{\mathrm{k}-1} + \mathbf{b}_{\mathrm{k}} \right), \tag{4.1}$$

where $\mathbf{h}_{\mathrm{act,k}}$ is the activation function of the given layer, $\mathbf{W}_{\mathrm{k}}$ is the weight matrix of the layer, $\mathbf{y}_{\mathrm{k}-1}$ is the output of the $(k-1)^{\mathrm{th}}$ layer and $\mathbf{b}_{\mathrm{k}}$ is the bias vector of the layer. Assuming that the k^{th} layer has N_{k} neurons, similarly the $(k-1)^{\mathrm{th}}$ layer consists of $N_{\mathrm{k}-1}$ neurons, the output vectors $\mathbf{y}_{\mathrm{k}} \in \mathbb{R}^{N_{\mathrm{k}}}$ ans $\mathbf{y}_{\mathrm{k}-1} \in \mathbb{R}^{N_{\mathrm{k}-1}}$. Also the weight matrix and the bias vector $\mathbf{W}_{\mathrm{k}} \in \mathbb{R}^{N_{\mathrm{k}} \times N_{\mathrm{k}-1}}$, $\mathbf{b}_{k} \in \mathbb{R}^{N_{\mathrm{k}}}$. The relation between the inputs and the output of a single neuron is illustrated in Figure 4.3. Thus, the output of the entire neural network can be expressed as a nested function

$$\mathbf{y} = \mathbf{y}_{\mathrm{L}} = \mathbf{h}_{\mathrm{act,L}} \circ \cdots \circ \mathbf{h}_{\mathrm{act,2}} \circ \mathbf{h}_{\mathrm{act,1}} \left(\mathbf{x} \right), \tag{4.2}$$

where $\mathbf{x} \in \mathbb{R}^{N_0}$ is the input vector of the network [3]. In the learning phase, the aim is to find the optimal elements of the weight matrices and the bias vectors in order to minimize the difference between the calculated output of the system and the expected, pre-defined output. For activation functions, usually nonlinear functions are chosen. Typical examples are rectified linear (relu, noted with r), sigmoid (in other words logistic, noted with σ), or hyperbolic tangent (tanh) functions. Mathematically, these functions can be expressed as,

$$r(x) = \max\left(0,\, x\right), \tag{4.3}$$

$$\sigma(x) = \frac{1}{1 + e^{-x}}, \tag{4.4}$$

$$\tanh(x) = \frac{2}{1 + e^{-2x}} - 1. \tag{4.5}$$

The above mentioned activation functions are illustrated in Figure 4.2.

In the field of machine learning, several learning algorithms are used, usually optimization techniques, that minimize the difference between the user-defined output of the

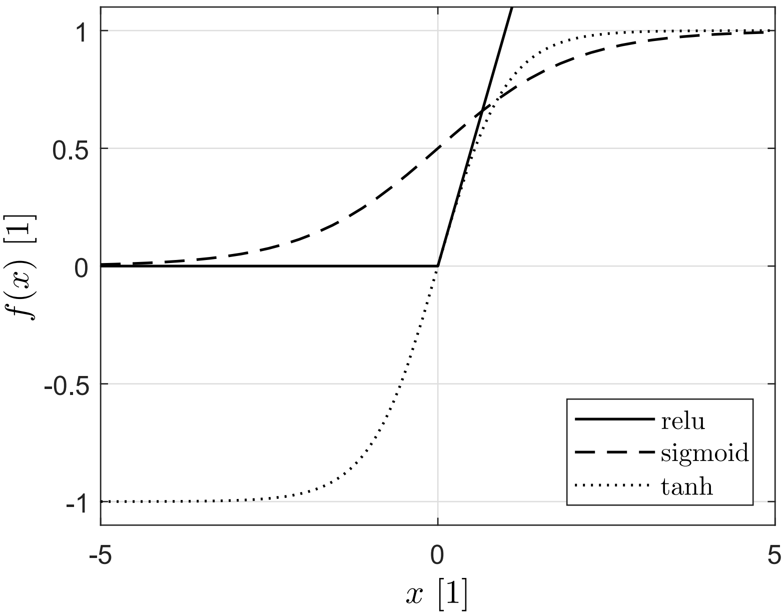

Figure 4.2: Different activation functions illustrated.

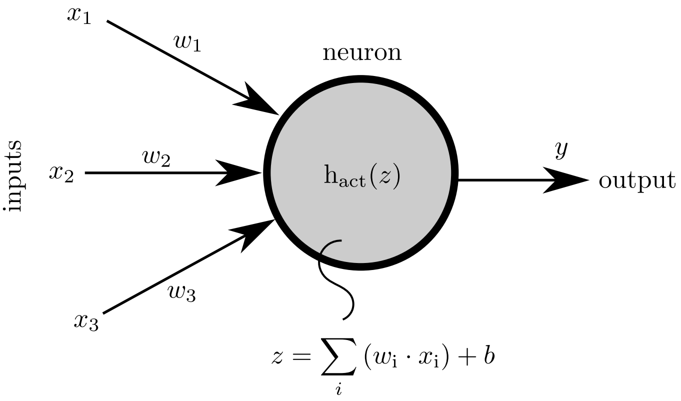

Figure 4.3: A single neuron with three inputs. The inputs, input weights, activation function, bias and output are all illustrated.

system and the actually calculated output. Neural networks are often used with iterative optimization algorithms, for example, the gradient descent method. The principle of the method is a pre-defined cost function, that compares the actual and the predicted output of the system, for example, the root mean square error of the data sets. The parameters of the cost function are the so-called hyper-parameters of the neural network. First, the network initializes the hyper-parameters randomly, then it tunes the parameters iteratively to get closer and closer to the global minima of the cost function. The values of the parameters in the next iteration step are calculated as the difference between the previous parameter vector and the gradient vector multiplied by the learning rate. The learning rate is a constant number, which is defined at the start of the learning process.

An iteration step of the optimization algorithm is called an epoch, therefore if the gradient descent method found the minima of the cost function with 16 iterations, the neural network was trained for 16 epochs. But it is not time effective to calculate the gradient for the whole training set, therefore the gradient is only calculated for a small, randomly selected set, called the mini-batch or simply batch, at every iteration step [19].

4.1.2 Estimating the coefficient of friction using neural networks

The neural network was programmed in Python, using the built-in functions from the libraries TensorFlow [20] and Keras [21]. The aim was to create a simple neural network, that can estimate the coefficient of friction without knowing anything from the physical system. The activation functions and the neuron count of the given layers were tuned empirically by checking the results of the estimation for three different activation functions (seen in Figure 4.2). Therefore the structure of the network is quite plain:

- input dense layer with 1024 neurons, sigmoid activation function,
- one dense hidden layer with 512 neurons and also sigmoid activation function,
- output dense layer of 1 neuron with no activation function (the output is the linear combination of the weights and inputs added by the bias of the layer).

The inputs of the neural network at a given time step were the yaw angle ψ, the previous local minima or maxima of the yaw angle signal $\psi_{\max}$ and the actual steering torque M. The output of the system is the estimated coefficient of friction. The training data set is illustrated in Figure 4.4.

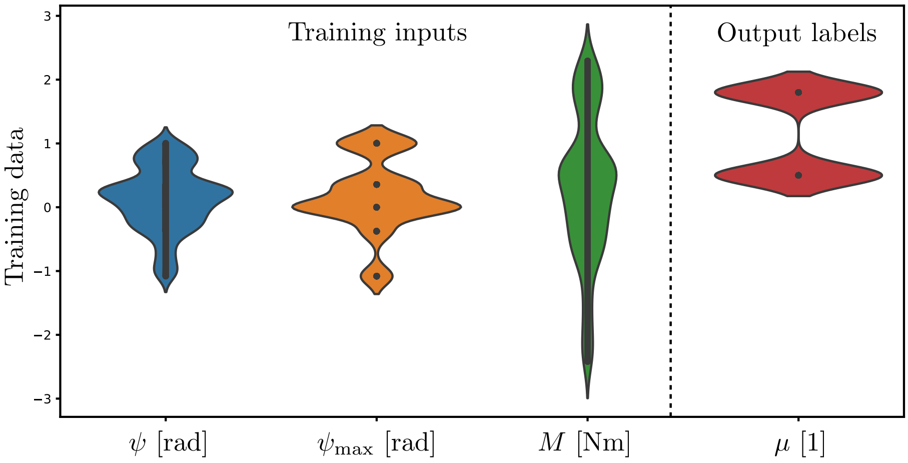

Figure 4.4: Training inputs of the neural network. The violin plot shows the distribution of the data, while the black dots represent the actual data points, therefore it is visible that the yaw angle and the steering torque are continuous functions, while $\psi_{\max}$ and μ are discrete values.

Before setting up the environment for the machine learning part, three different simulations were made using the simulation process introduced in Section 2.2. The simulations were made with three different coefficients of friction, with $\mu = 0.5$, $\mu = 1$ and $\mu = 1.8$. The other physical properties remained the same as in Table 3.1. The data sets with the smallest and largest coefficient of friction were used for training the network, and the simulation case with the middle value was used for testing the trained neural network.

The training data set was imported in a shared data frame, and the rows were shuffled in order to prevent over-fitting. The batch size was selected to be 32, because several studies imply that small batch sizes result in better results with less training time [22]. The network was trained for 30 epochs, using the Adam optimizer from the Keras library with a learning rate of 0.001. These options were selected because the optimizer usually found the best fitting parameters by the fifteenth epoch (as it is visible in Figure 4.5), but then fifteen more epochs were trained to ensure that the optimizer could not find any best solution. The stochastic nature of the Adam optimizer and the mini-batch method was the motivation for setting the training process two times as long as necessary, therefore guaranteeing that not a local, but the global optimum has been found. During the training, 10% of the data was used for validation to determine the error of the network after each iteration. The error was monitored with the root-mean-squared error (RMSE) metric. A so-called call-back was also defined to restore the weights after the iteration process ended, to match the best validation error achieved during training. The errors of a typical training process can be seen in Figure 4.5. The training error corresponds to the error of the neural network on the data set, that was used for training, while the validation error was calculated for the validation split, which did not take part in training the model.

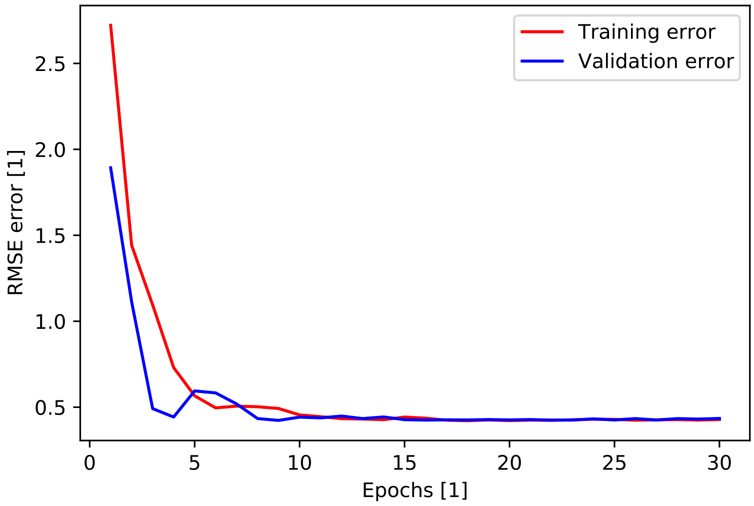

Figure 4.5: Error of the models during a typical training process.

As previously mentioned the sigmoid activation function was chosen with the given neuron counts to provide the most accurate estimation of the friction coefficient. To determine these three parameters (number of neurons in the first and second layer and the activation function), the model was trained with a lot of different settings to find which one provides the best approximation. The two layers were both tested with 2, 4, 8, 16, 32, 64, 128, 256, 512 and 1024 neurons with all available variations of layer two and layer one neuron counts. Three activation functions were used: relu, sigmoid and tanh, as in Figure 4.2. The trained models were all tested on the same data set and were ranked based on the RMSE values of the approximations. The best model architecture for each activation function is listed as:

- Sigmoid activation function, first layer with 1024 neurons, second layer with 512 neurons. The RMSE value was 0.015.
- Relu activation function, first layer with 256 neurons, second layer with 512 neurons. The RMSE value was 0.0716.
- Tanh activation function, first layer with 1024 neurons, second layer with 64 neurons. The RMSE value was 0.0866.

To see the effect of the neuron count on the whole estimation process, the RMSE values for all the layer count variations can be illustrated as a three-dimensional surface for a given activation function. In Figure 4.6, the RMSE values for the best fitting activation function, namely for the sigmoid function, are visible. For better visibility, the layer counts are illustrated on a logarithmic scale. Apart from three-dimensional surfaces, two-dimensional contour plots can also represent the examined phenomena. In Figure 4.7, the contour plots of RMSE values for the other two activation functions (relu and tanh) can be seen.

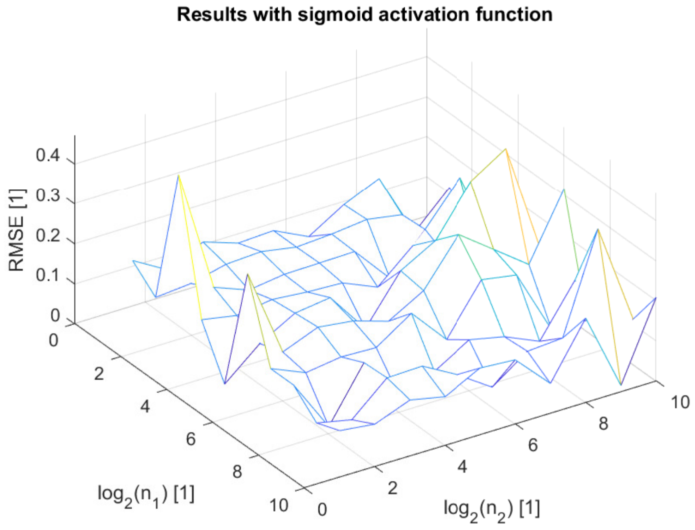

Figure 4.6: RMSE values for all the neuron count variations in case of the sigmoid activation function. The first layer's neuron count is denoted by n_1, the second layer's by n_2.

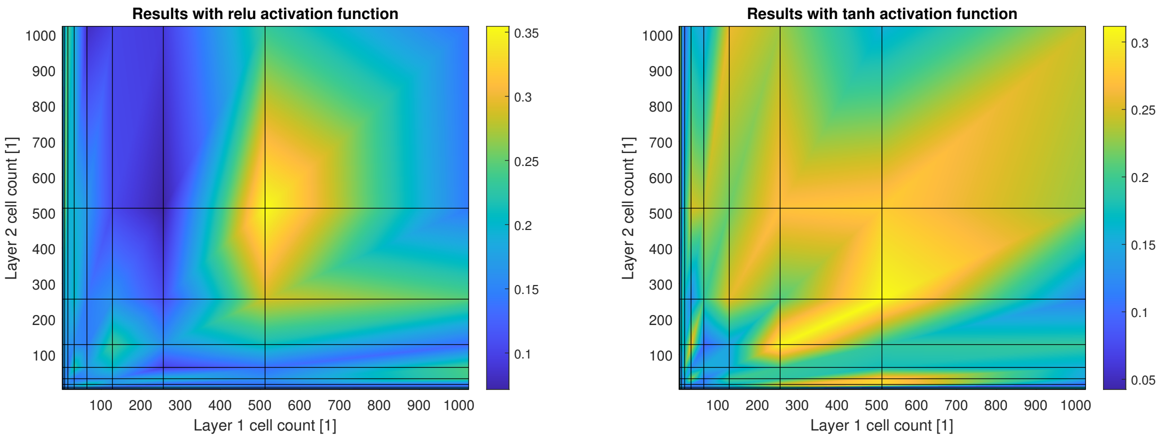

(a) **(b)**

Figure 4.7: Illustrating the RMSE values for all the possible neuron count variation. In (a) the RMSE values for the relu activation function, in (b) the RMSE values for the tanh activation function are visible.

After training the neural network, the accuracy of the estimation was tested on the simulated data set with $\mu = 1$. The error of the estimation was 0.1068 using the RMSE metric, which is around 10% relative error. The results of the estimation can be seen in Figure 4.8.

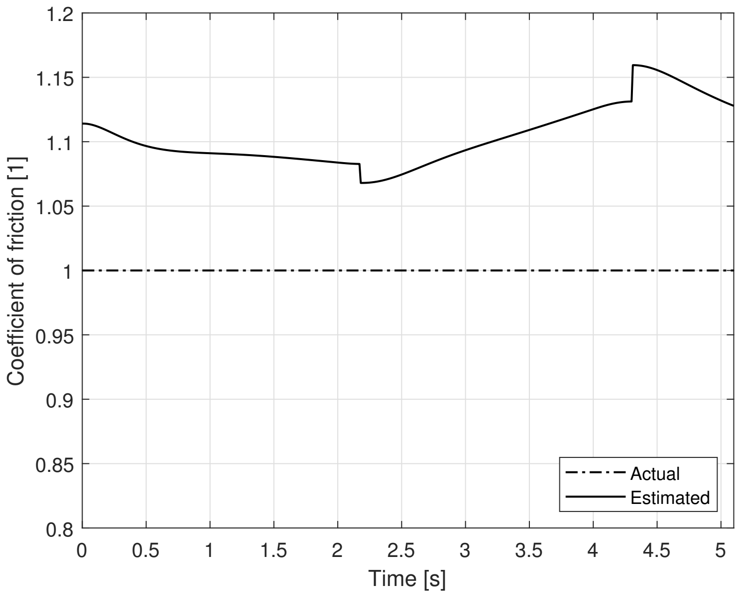

Figure 4.8: Results of the estimation with the simple neural network model.

A comparison can be made with the derived analytical estimation method on the left side of Figure 4.9. It is visible that the analytical approach (apart from the errors in the beginning) is more accurate than the neural network. But it is important to mention that the test case was simulated with a steering torque characteristic similar to the simulation cases that were used for training the model. On the left-hand side of Figure 4.9, the estimation methods were compared using a different steering torque input. At the end of the simulated time interval, huge errors are visible for the analytical method, because there are more than five fragmentation zones in the deformation function, for which the method was not derived. Also, the neural network estimation is not sensitive to small yaw angles, therefore it provides a more accurate solution at the beginning of the simulation time. Consequently, the proposed analytical estimation method is more accurate, but the neural network is more robust.

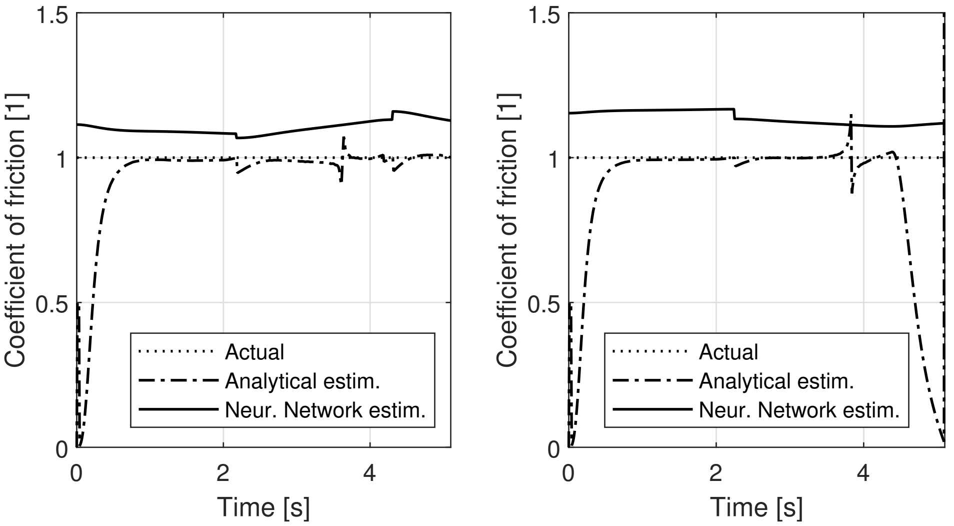

Figure 4.9: Comparing the results of the estimation with neural network with the results from analytical method. On the left, the input steering torque characteristic is similar to the steering torque in the training data. On the right different steering torque input was applied, therefore more fragmentation zones formed in the deformation function, thus the analytical approach was not accurate in the end.

4.2 Estimation process implementing a Scientific Machine Learning (SciML) model

While traditional machine learning (ML) algorithms are shown to be able to model nonlinear dynamical systems, there are some essential problems that are still not solved. Most importantly machine learning structures need large sets of training data for accurate operation. Although in some cases it is possible to acquire such big data sets via measurements, usually it is not the case. The next problem is that ML models cannot extrapolate out of the training data set well, and lastly the results are hard to interpret. For example, after training a neural network, the weight and bias values can be obtained, but there is no clear expression that can describe the investigated physical system.

In contrast to traditional ML models, scientific machine learning (SciML [23]) is a quite unique and new field of machine learning research. The basic principle of the method is to incorporate the knowledge about the investigated physical system, but the effects of the unmodeled terms are compensated with a machine learning structure (e.g. neural networks).

4.2.1 Universal differential equations within scientific machine learning

Within SciML, the use of universal differential equations (UDEs) is a newly applied approach [24]. UDEs are standard differential equations supplemented with machine-learnable parts. A non-general form of universal differential equations can be expressed as

$$\dot{\mathbf{x}} = \mathbf{f}\left(\mathbf{x}, \mathbf{p}\right) + \mathbf{U}\left(\mathbf{x}, \mathbf{p}, \mathbf{q}\right), \tag{4.6}$$

where $\mathbf{x}$ is the unknown vector, $\mathbf{f}$ describes the system with the physics-based modeling method, $\mathbf{p}$ vector contains the physical parameters of the mechanical system (assumed to be constant) and $\mathbf{U}$ is the machine learnable part with $\mathbf{q}$ parameters of the machine learning structure (e.g. the hyperparameters of a neural network). Also in equation (4.6) the noise terms are neglected and the state variable $\mathbf{x}$ is assumed to be observable.

A typical workflow of applying a SciML method with UDEs is to first derive the analytical differential equations that describe the system, then gather measurement data. After fitting the physical properties (noted with $\mathbf{p}$ in equation (4.6)) in a way to match the physics-based approximation with the measurement data the best way. Then finally, the only unknowns are the machine learning model parameters, which can be obtained by training the model, for example, a neural network with gradient descent.

For the model presented in Section 2.2, the following UDE system can be derived, but first, define the unknown vector as

$$\mathbf{x} = \begin{bmatrix} q(x,t) \\ \dot{\psi}(t) \end{bmatrix}. \tag{4.7}$$

Then from equation (2.12), (2.13) and (2.3) the universal differential equation can be derived, neglecting the nonlinear term:

$$\begin{bmatrix} \dot{q}(x,t) \\ \ddot{\psi}(t) \end{bmatrix} = \begin{bmatrix} (e-x)\cdot\dot{\psi}(t) \\ -\left(b_t/J_A\right)\cdot\dot{\psi}(t) - \left(1/J_A\right)\cdot\int_{-a}^{a} k\, q(x,t)\, (x-e)\,\mathrm{d}x + \left(1/J_A\right)\cdot M(t) \end{bmatrix} + \\ + \mathbf{U}\left(\mathbf{x}, \mathbf{p}, \mathbf{q}\right), \tag{4.8}$$

where $\mathbf{p}$ vector contains e, b_t, J_A, a and k.

Using the UDE structure in (4.8), with appropriate measurement data, the machine learning algorithm parameters could be calculated, but there is a problem originating from the assumption, that the state variable of the system is observable, which is not the case. Experiments showed, that it is possible to examine the contact line parameters during static load [25], but this method could not be applied with angular motion, therefore a modification for the UDE SciML method had to be made.

4.2.2 Using scientific machine learning to estimate the coefficient of friction

As previously mentioned, the SciML method works well with universal differential equations, but due to the nature of the investigated mechanical system, the UDE approach cannot be applied. Thus, a new method was developed, similar to the UDEs, but for nonlinear algebraic equations, that express a physical meaning. Using the derived analytical approach in Section 3, a universal nonlinear algebraic equation can be defined as

$$\mu = n(\mathbf{p}) + U(\mathbf{p}, \mathbf{q}), \tag{4.9}$$

where n is the numerical solution of $f(\mu) = 0$, $\mathbf{p}$ vector contains all the physical parameters that need to be provided in order to solve the nonlinear equation $f(\mu) = 0$ and $\mathbf{q}$ is the parameter vector of the machine learning system.

Solving the physics-based part happens the same way, as discussed in Section 3. The neural network-based part of the solution was determined with a similar machine learning model as in Section 4.1.2, the only difference is that the network gets all of the physical parameters of the system as an input (namely ψ, ψ_{max}, M, e, F_{N}, the direction of rotation, the number of fragmented zones, a, k and of course the analytically estimated μ), therefore a more robust architecture was found to be more efficient. The best activation function and neuron count were determined with an empirical study, similar to the simple neural network. Interestingly, in this case, the tanh function proved to be a better choice. The structure can be summarized as

- input dense layer with 2048 neurons and tanh activation function,
- one hidden layer with 1024 neurons and also tanh activation function,
- output dense layer (1 neuron), with no activation function.

The model is trained with simulation data sets of $\mu = 0.5$ and $\mu = 1.8$, while the test case is the $\mu = 1$ simulation. Similarly to the neural network validation, another test case was defined, for a steering torque characteristic, where more than five fragments appear in the deformation function in order to test, how will the model react to a case, where the analytic approach is not derived. The results are shown in Figure 4.10.

Consequently, as Figure 4.10 also shows, the proposed SciML method's accuracy is compatible with the analytic estimation, moreover the numerical errors and the unmodeled effects can be also compensated, thus this technique can be utilized to provide a robust and accurate estimation of the coefficient of friction.

4.3 Sensitivity analysis of the three methods

The previously proposed methods can be compared based on a lot of aspects, one of them being how much difference can they tolerate in the input signals in order to still

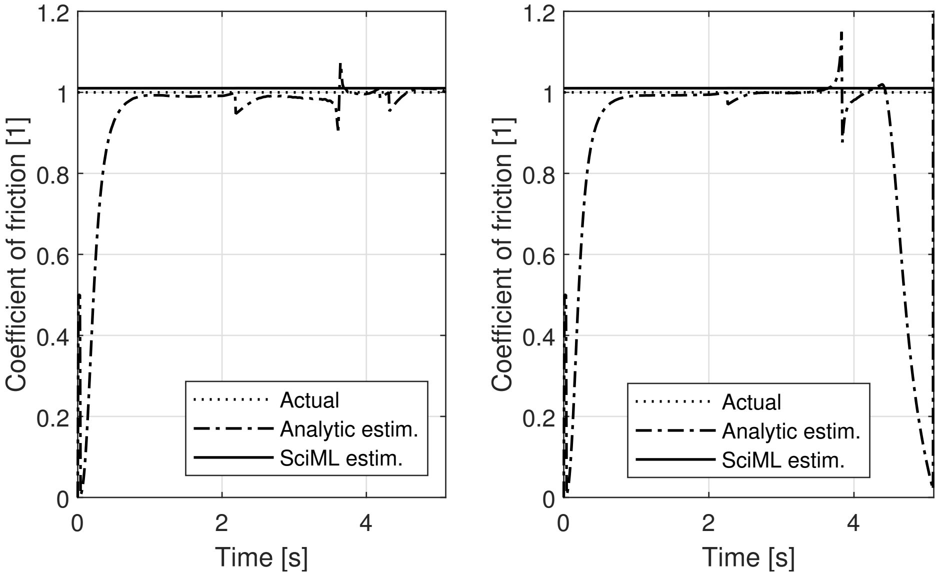

Figure 4.10: The results of the coefficient of friction estimation with the proposed SciML method. The method is tested on a steering torque characteristic, for which the analytic estimation was derived (left), and another steering torque input for which the analytic method is not accurate (right). The results of the analytic estimation method are also shown.

provide an accurate estimation. For example, if the yaw-angle signal is heavily influenced by measurement noise can they still approximate the coefficient of friction with relatively high accuracy? For testing this, from one of the simulation cases with $\mu = 1$, a time interval was chosen right after a direction change with $\psi_{\max} = 0.7126$ rad. The yaw angle and steering torque during this time period are illustrated in Figure 4.11.

The minimum steering torque is -1.5669 Nm, and the maximum is 1.5129 Nm. For the yaw angle, these values are respectively -0.7521 rad and 0.7126 rad. A mesh has been defined as the steering torque is scaled from -1.5 Nm to 1.5 Nm and the yaw angle is from -0.75 rad to 0.75 rad both with a hundred elements. Along this numerical surface defined by the two physical properties, the estimation methods have been evaluated for each mesh point (all the other physical parameters have been kept constant). Of course, the majority of this surface is physically not achievable, but for curiosity, the methods have been tested for all the mesh points. The resulting coefficient of friction can be illustrated as the third coordinate to form a three-dimensional surface. For the analytical approach, this surface is illustrated in Figure 4.12. The coefficient of friction values that are fallen into the maximal of 10% error zone are illustrated with green color. The yaw angle and steering torque pairs that are a result of the simulation (shown in Figure 4.11) are illustrated with a red line. From Figure 4.12 it is visible, that the analytic estimation provided accurate results for the physically achieved values, and can even handle small inaccuracies of the input values.

A similar surface could be presented for the neural network-based estimation, but the

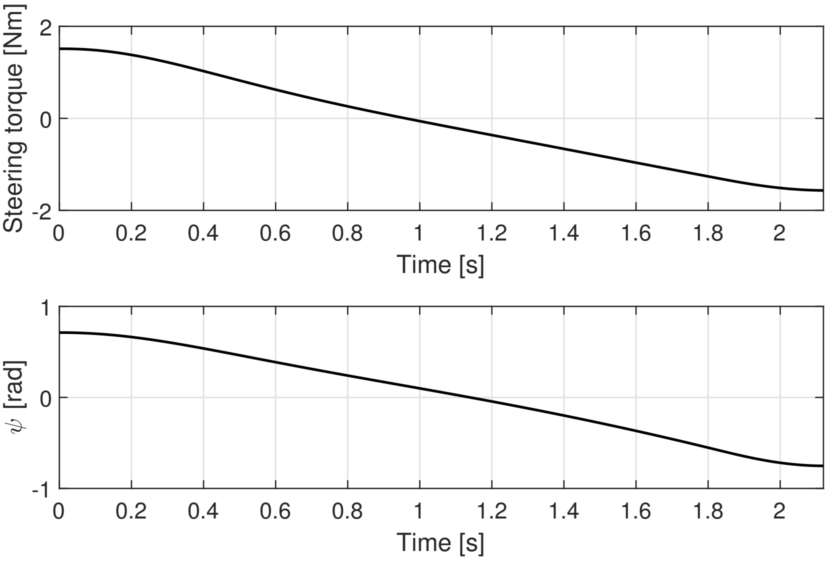

Figure 4.11: Yaw angle and steering torque signals for the investigated duration in the sensitivity analysis.

evaluation of this method resulted in a more "flat" surface, with nearly all of the values on the boundary of the 10% error range, therefore this plot is not shown here, but it is interesting to notice that the neural network based estimation provided quite accurate results even for the physically unachievable parts of the mesh. This problem was mentioned earlier, that neural networks are capable of universally approximating all sorts of physical phenomena, but the internal working of the network cannot be interpreted on a physical level. Thus, the SciML method was mentioned earlier as a possible solution, and it is visible in Figure 4.13, that physically unachievable parts have an impact on the SciML estimation method, but the possible inaccuracies of the input parameters (in this case only the yaw angle and the steering torque) have influenced the estimation less, compared to the analytic case. Apart from the known limitations of the machine learning-based methods, the main consequence of this sensitivity analysis is that not enough training data was provided for the neural networks. In Section 5, an experiment will be performed in order to validate the proposed methods on measurement data. The lesson has been learned from the simulation cases, therefore significantly more training data will be provided for the neural networks in order to achieve the maximum accuracy.

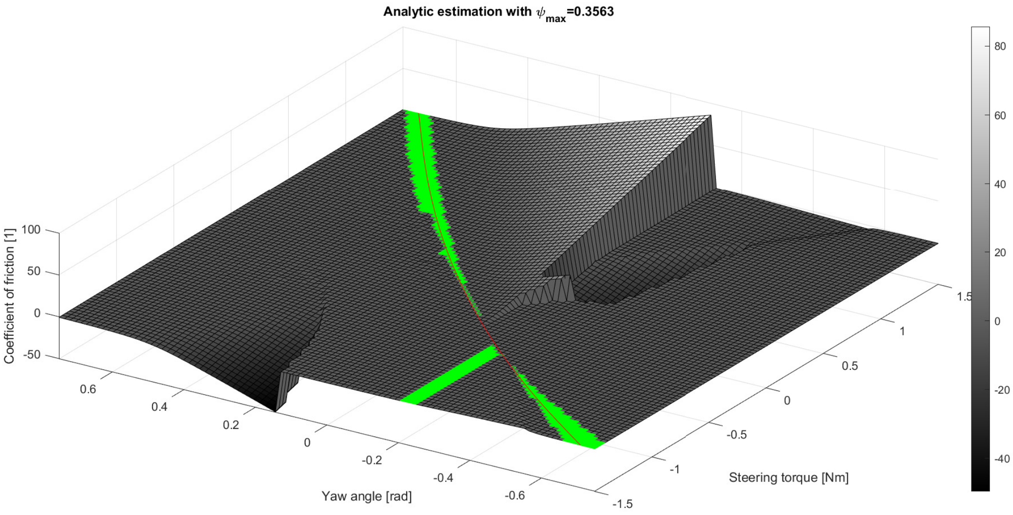

Figure 4.12: Results of the sensitivity analysis for the analytic estimation method. The green surfaces show the values that belong in the 10% error region. The red line shows the physically achieved part during the simulation.

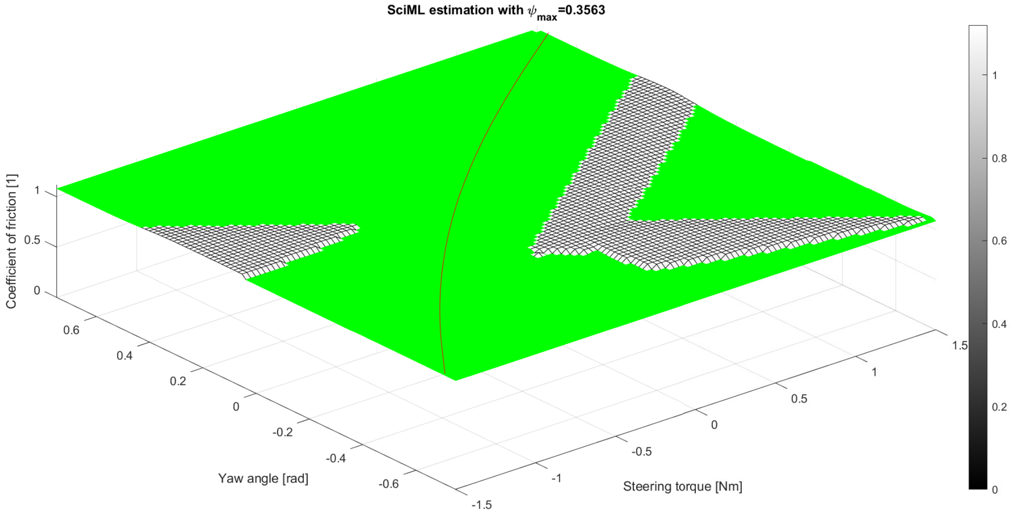

Figure 4.13: Results of the sensitivity analysis for the SciML-based estimation.

5 Measurement

To validate the previously proposed estimation methods, it is not enough to test with simulated data, therefore a measurement setup needs to be developed. Fortunately, experiments have been carried out for a long time at the Department of Applied Mechanics to investigate the dynamical properties of towed wheels [26]. Thus, an already established experimental set-up was used with some modifications, which will be detailed in this section.

5.1 Measurement set-up

At the Department of Applied Mechanics, an experimental rig has been developed, that was used during this work. The experimental setup can be seen in Figure 5.1. The investigated bicycle wheel is mounted in a way that allows the modification of the towing length e. The caster can be rotated about the rigid kingpin, where oil lubrication ensures that the effect of dry friction can be neglected, and low torsional damping is expected. The length of the contact patch can be modified by changing the vertical distance between the kingpin and the "road" surface.

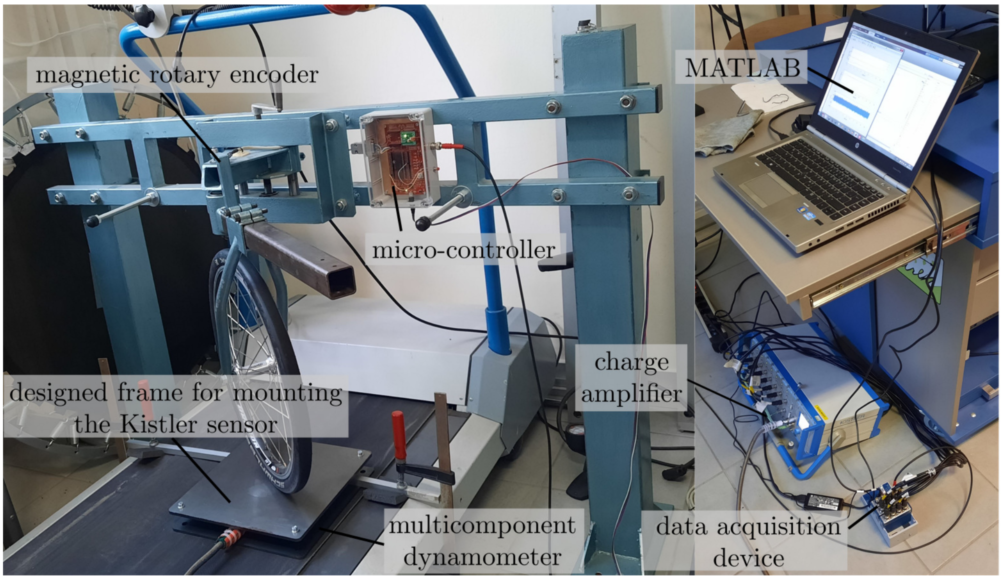

Figure 5.1: Experimental rig with the used devices.

The experimental setup allows measurements with non-zero towing speed, but the previously derived estimation methods were developed for tires standing still. The steering torque needs to be measured in order to estimate the coefficient of friction, but using this set-up the direct measurement was not possible, because the steering torque was actuated by hand, therefore a Kistler 9129AA Multicomponent Dynamometer was used to measure the self-aligning torque. With zero towing speed, the conveyor belt was not moving, thus it was possible to place the force sensor below the tire. To do so, a special experimental frame was designed and manufactured from metal sheets, to mount the Kistler sensor onto the conveyor belt. For the force sensor, a Kistler Type 5080A charge amplifier was also used. The yaw angle $\psi(t)$ was measured with a magnetic rotation sensor placed at the joint (AMS AS5048A magnetic rotary encoder, 14-bit resolution). For detecting and digitizing the measured angle signals, a PIC microcontroller was used (part of the experimental rig). The measurement data was gathered using a National Instruments USB-6216 (BNC) data acquisition device, but the measured signals were processed in MATLAB.

For testing the estimation methods, different surfaces need to be used during the measurements. The designed frame made it possible to attach an extra plate to which different surfaces could be cemented. Three different plates were selected with different frictional characteristics. One plate was plain steel, the other two plates had emery papers glued on, with different surface roughness.

5.2 Identification measurements

For the analytical estimation model, some physical properties have to be provided. The towing length can be measured on the experimental rig, for all measurements $e = 0.009$ m was preset. The vertical load force was measured by the Kistler 9129AA device, while the length of the contact patch was measured with a vernier caliper. The yaw angle and the self-aligning torque was gathered as previously mentioned.

The only remaining input of the model is the lateral stiffness k, which can be only determined via identification measurements. In practical applications, it would be hard to identify k, but the value of the lateral stiffness is constant for constant internal tire pressure, therefore by measuring the tire pressure, k could be estimated. But in this experiment, the lateral stiffness value is identified from the natural frequency of the system, which can be determined experimentally.

For the neural network-based estimation methods, while training the models, an accurate coefficient of friction value needs to be provided. Moreover, it is necessary to know the exact value of μ for validation purposes, thus the coefficient of friction also needs to be identified.

5.2.1 Identifying the coefficient of friction for different measurement plates

As mentioned before three different plates were used during the experiments, with three different coefficients of friction. A simple experiment was applied in order to estimate the values of the coefficients of friction. A wooden object with rubber material glued onto the surfaces was towed on the measured plates, while measuring the forces with the Kistler Multicomponent Dynamometer. The rubber material was chosen to be similar to the elastic rubber of the measured tire. The experiment setup can be seen in Figure 5.2.

The experiments were carried out with different normal forces for each plate to estimate the coefficient of friction. As mentioned in section 2, the static and dynamic friction

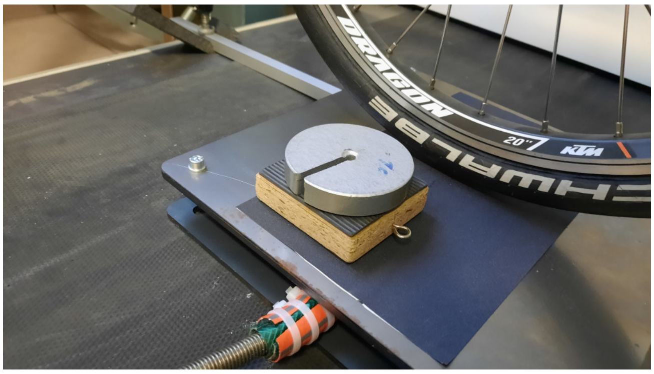

Figure 5.2: Experiment set-up for measuring the coefficients of friction

properties are assumed to be the same, therefore as all three force components were measured (F_x, F_y and F_z), the measured data is fitted to the function expressed as

$$F = \mu N, \tag{5.1}$$

where $F = \sqrt{{F_x}^2 + {F_y}^2}$ and $N = F_z$.

The measurement has been carried out for all three plates with different normal loads. The results for one plate (black emery paper) can be seen in Figure 5.3. The fitted curve can be considered accurate, therefore the values of each coefficient of friction (summarized in Table 5.1) are appropriate for validating the estimation methods.

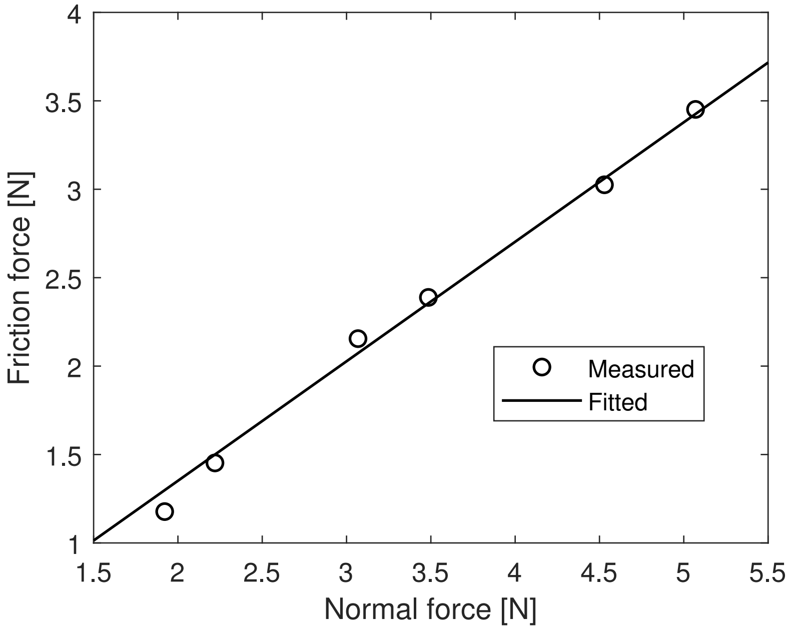

Figure 5.3: Results of the coefficient of friction identification measurement for one of the emery papers.

Plate	Coefficient of friction [1]
Metal plate	1.674
Emery paper (red)	1.9003
Emery paper (black)	0.6757

Table 5.1: Identified coefficients of friction.

5.2.2 Identifying the lateral stiffness of the tire

To identify the distributed lateral stiffness of the tire, the system is modeled as one degree-of-freedom damped oscillator, then the relative damping ratio ζ and the damped natural angular frequency ω_d was calculated from the measurement data. During the identification measurements, the caster was perturbed by an impact, and it was repeated five times for each different contact patch length. The measurement signals for one of the contact patch lengths can be seen in Figure 5.4.

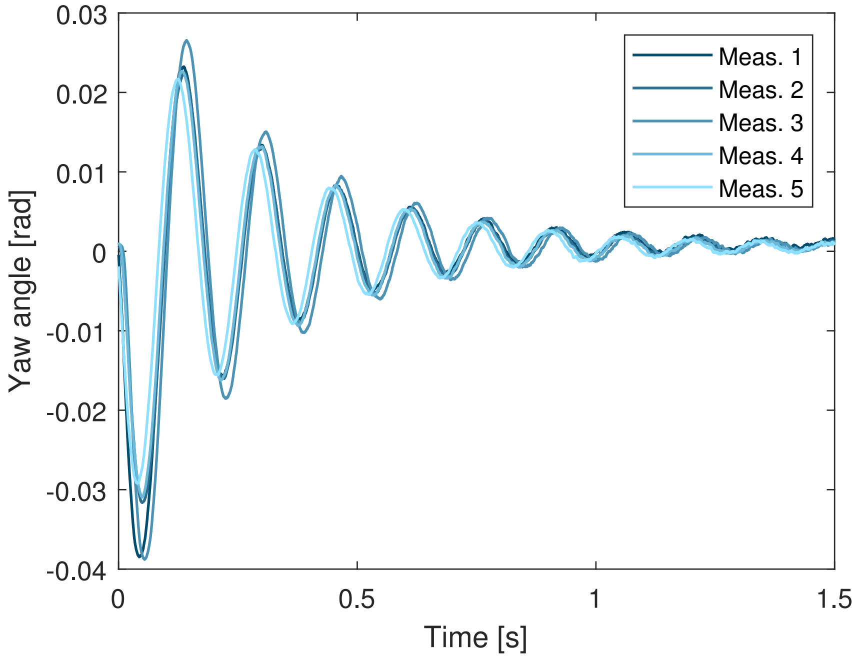

Figure 5.4: Five measurement signals for one of the contact patch lengths. All of the mechanical parameters are the same, only the initial excitation is different, thus the damping and the damped natural frequency are visibly identical.

The natural frequency of the damped system was determined by using the built-in Fast Fourier Transformation (FFT) function in MATLAB, and the natural angular frequency ω_d can be calculated as

$$\omega_\mathrm{d} = 2\pi f_\mathrm{d}, \tag{5.2}$$

where f_d is the natural frequency of the damped system. The relative damping ratio was calculated with the method of logarithmic decrements as [27]

$$\Lambda = \frac{1}{n} \ln\left(\frac{A_1}{A_{n+1}}\right), \tag{5.3}$$

$$\zeta = \frac{\Lambda}{\sqrt{4\pi^2 + \Lambda^2}}, \tag{5.4}$$

where Λ is the logarithmic decrement, A_n notes the n^{th} maximal deflection for a given direction and ζ is the relative damping ratio. Then the natural angular frequency of the undamped system ω_n can be determined with the following expression:

$$\omega_\text{n} = \frac{\omega_\text{d}}{\sqrt{1-\zeta^2}}. \tag{5.5}$$

Thus, the natural angular frequency of the undamped system and the relative damping ratio is known, now the lateral stiffness value needs to be calculated. From [28], the equation of motion with v towing speed, taking into account the delayed effect of the self-aligning torque can be expressed as

$$J_A\,\ddot{\psi}(t) + b_\text{t}\,\dot{\psi}(t) + 2ak\left(e^2 + \frac{a^2}{3}\right)\psi(t) = (e-a)\,vk\int_0^{\frac{2a}{v}} (e-a+v\tau)\;\psi(t-\tau)\,\mathrm{d}\tau\,, \tag{5.6}$$

with the previously used notations and τ is the time delay. Thus the natural angular frequency of the undamped system can be expressed as

$$\omega_\text{n} = \sqrt{\frac{2ak\left(e^2 + \frac{a^2}{3}\right)}{J_A}}. \tag{5.7}$$

As well as the relative damping ratio:

$$\zeta = \frac{b_\text{t}}{2\omega_\text{n}}. \tag{5.8}$$

The experiment was repeated with seven different contact patch lengths, while keeping the towing length e the same. The value of k and b_t was calculated to fit the theoretical curves of (5.7) and (5.8) to the measurement results with the least error possible. The results of the experiment and the curve fitting can be seen in Figure 5.5.

While the undamped natural frequency can be identified quite accurately with the FFT algorithm, measuring the damping is much harder, therefore the deviation of the damping data set is larger compared to the natural angular frequency. In Figure 5.5, some outlier values are visible in the measured relative damping. Although by deleting those outlier values, probably a more accurate torsional damping value could be calculated, but the aim of this experiment was the identification of k, therefore the results were accepted and the identified values are summarized in Table 5.2.

All the remaining measurements were carried out with the same inner tire pressure of $p = 1$ bar, therefore the identified distributed lateral stiffness value is valid for all the latter experiments.

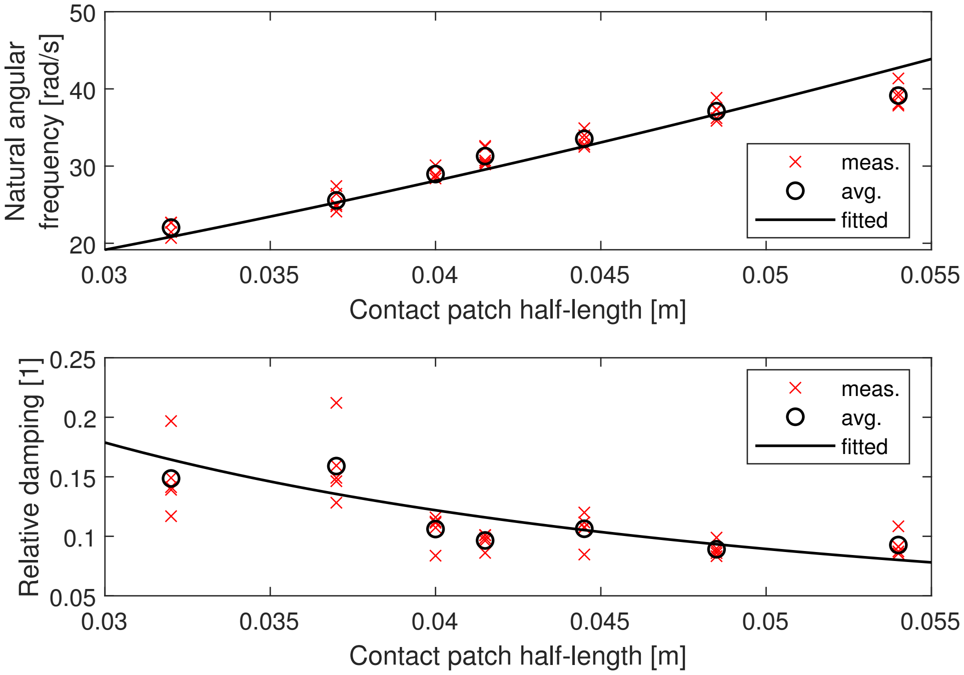

Figure 5.5: Identification results for the lateral stiffness and the torsional damping. The red crosses represent the measured data points, while the black circles are the average value for each contact patch half-length. The black line shows the fitted theoretical curve.

Physical property	Notation	Identified value
Distributed lateral stiffness	k	$2.438 \cdot 10^6$ N/m^2
Torsional damping	b_t	6.8509 Nms

Table 5.2: Identified lateral stiffness and torsional damping.

5.3 Evaluating the proposed calculation methods using the measured data sets

After the identification experiments, the validation measurements were carried out in order to test the proposed estimation methods. While the derived analytic calculation method can be applied for every measurement case, the machine learning-based techniques need training data as well, therefore the surfaces with the smallest and the largest coefficient of friction (the black and red emery papers) are used for training the models, then the results are validated on the third measurement case.

The measurements were carried out as discussed in section 5.1, then the post-processing was performed in MATLAB. First, the angle, force, and torque offsets were determined and the signals were corrected with it. The measurement was executed with 4000 Hz sampling frequency, but the evaluation of each data point would take too much time, therefore the signals were under-sampled to match the simulation frequency. Also, the angle signal needed to be filtered with a moving average filter, to provide smooth angle signals to the estimation methods.

The analytic estimation algorithm expects the previous local minima or maxima of the yaw angle (noted with ψ_{max}) as well as the number of fragmentation and the direction of angular motion at every time-step, therefore these values were calculated during the post-processing of the data. In Figure 5.6, the yaw angle signal of an arbitrary measurement case is visible with the determined ψ_{max}. In the first zone, the value of ψ_{max} is defined as zero, because there is no local extremum before the first direction change.

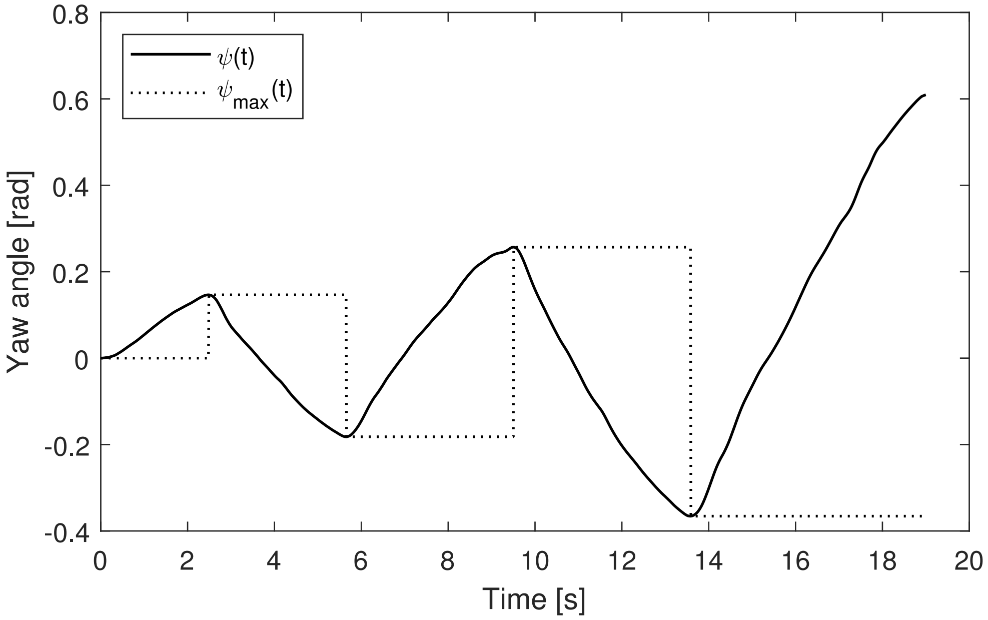

Figure 5.6: The yaw angle signal and the determined ψ_{max} values of an arbitrary experiment case.

The direction of motion could be easily determined, but for the fragmentation number, the previously proposed state machine (Figure 3.5) was used. The results are visible in Figure 5.7.

5.3.1 Estimation based on the analytic modeling approach

All of the necessary physical or nonphysical input properties have been determined for the analytic coefficient of friction estimation by measurements or during post-processing the measured data. Thus, the results of the estimations can be compared to the identified coefficients of friction.

The results of the estimation for both emery papers are reassuring, but the estimation for the metal sheet's coefficient of friction was quite inaccurate. The numerical problems causing big oscillations are similar to the ones in the simulation phase, but the errors caused by small angles and the sudden jumps in case of direction change disappeared. Although the previously identified coefficient of friction values (Table 5.1) seemed accurate,

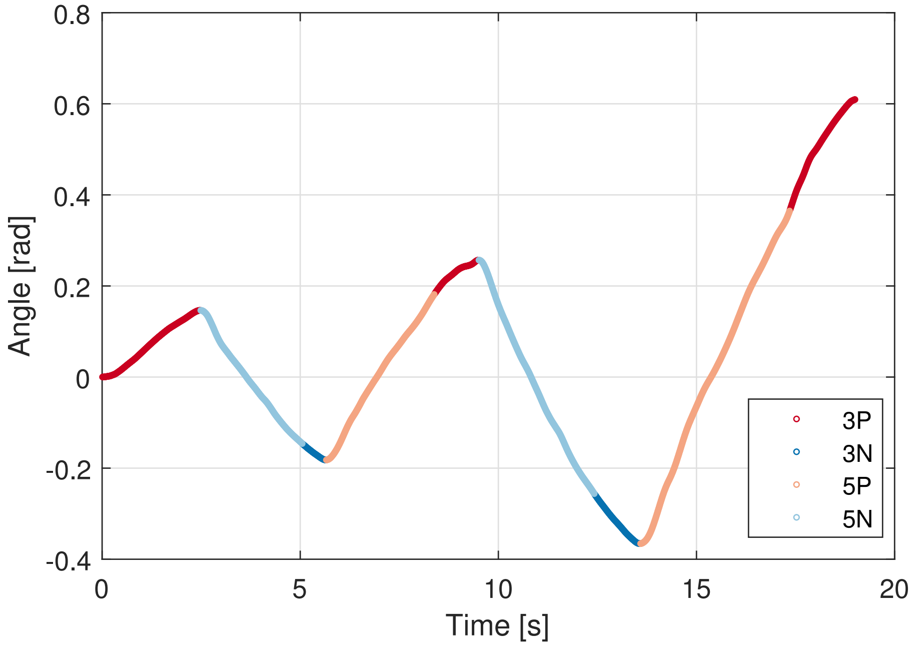

Figure 5.7: The fragmentation number and the direction of angular motion for an arbitrary measurement case. On the legend, the number represents the fragmentation count and the "P" stands for positive, and "N" is for negative direction.

there probably is some inaccuracy in the measurement, because the estimated friction coefficient values often tend to the same number, but not to the identified value. An example is shown in Figure 5.8 for one of the estimation cases. All of the other estimation results can be found in the Appendix.

In Figure 5.8 huge oscillations are visible in the estimated friction coefficient signal. A possible solution to this problem is the filtering of the signal, for example with an exponential smoothing filter. The exponential filtering method was chosen, because it is suitable for a possible real-time application, due to the fact, that at a given time step only the current and the directly previous signal values are needed for the calculations. The filtering can be characterised with α constant, as

$$\mu[k] = \alpha \cdot \mu[k-1] + (1-\alpha) \cdot \tilde{\mu}[k], \tag{5.9}$$

where $\mu[k]$ is the smoothed estimation at the k-th time step, and $\tilde{\mu}[k]$ is the raw estimation at the same time step. Generally α is chosen to be between 0.8 and 0.99 [29], but in this case, only quite small values ($\alpha \approx 0.01$) provided noticeable improvement in the accuracy of the estimation. An example is illustrated in Figure 5.9, with $\alpha = 0.01$. It can be seen, that although the oscillations are reduced, significant time-shift is realised, caused by the filtering. With zero longitudinal velocity, thus "standing still", the friction properties are not changing abruptly, therefore the time-shift is not a deal breaker. The main disadvantage of the filtering is that the transient process at the beginning of the motion is extended, therefore more time is needed for an accurate approximation.

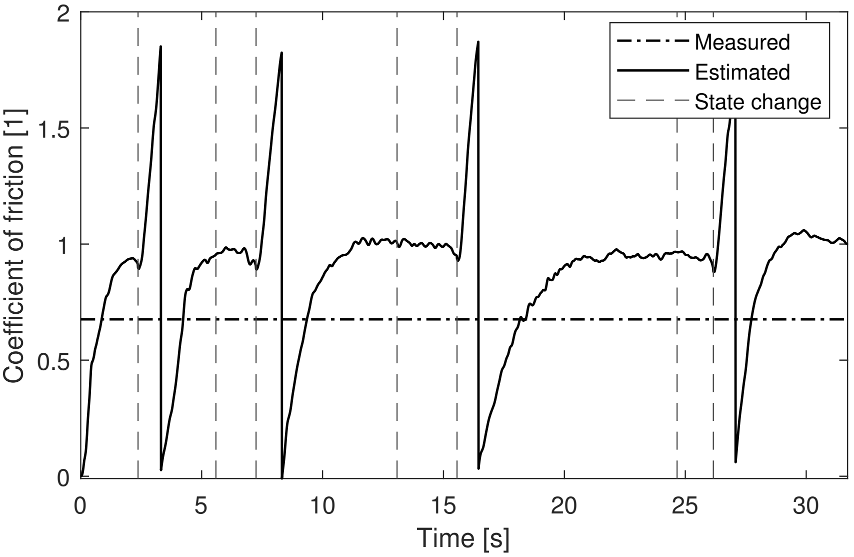

Figure 5.8: Results of the estimation for one of the measurement cases. The vertical dashed lines represent the change of state, according to the state machine derived previously.

In Figure 5.8, apart from oscillations caused by the numerical error, the value of the estimation tends to be around $\mu = 0.95\ldots$, but the identified coefficient value is 0.6757. To compare the accuracy of the estimation, the RMSE value was calculated for each estimation. Also, the time spent on calculating the estimated values was also monitored with a dimensionless value as

$$\vartheta = \frac{t_{\text{calculation}}}{t_{\text{measurement}}}, \tag{5.10}$$

where $t_{\text{calculation}}$ is the time cost of the estimation and $t_{\text{calculation}}$ is the duration of the measurement. The duration of each calculation was measured on the same computer, with an Intel(R) Core i5-8250U processor, 16 GB of RAM, and an NVIDIA GeForce MX150 GPU. The accuracy and the time cost of the estimation are illustrated in box charts in Figure 5.10, where the horizontal blue lines inside each box represent the median of the data set, the upper and lower ends of each box show the upper and lower quartiles and the horizontal black lines outside of the boxes correspond to the maximum and minimum of the data set.

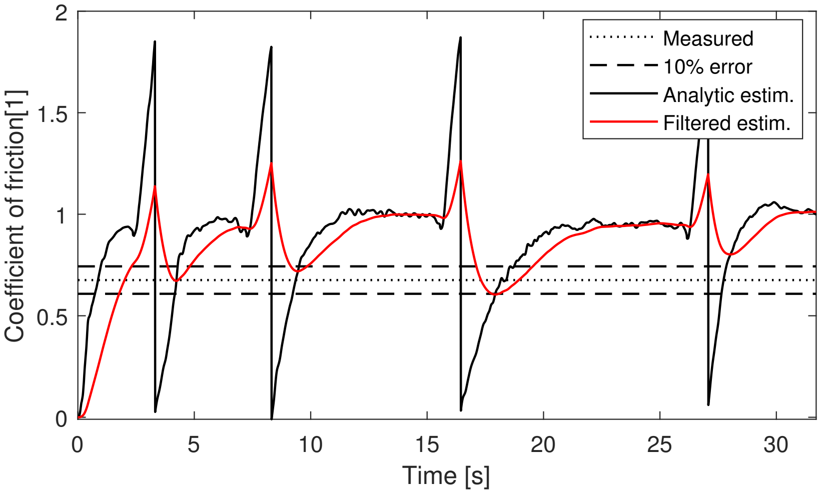

Figure 5.9: The results of the exponential filtering applied to the estimation shown in Figure 5.8

5.3.2 Estimation with machine learning based methods

The machine learning-based estimations were carried out with the same process. The training data set consisted of the measurements of the black and red emery paper, while the results were tested on the metal sheet measurements. Although the SciML method also considered the solution of the analytic estimation as well as other physical properties, the principle of the method is similar to the neural network estimation. After data post-processing and training the model, the estimation was made for the validation data sets. The training losses can be seen in Figure 5.11 for the training of the neural network model (the training of the SciML model produced similar loss values, but the convergence was faster). In Figure 5.11, it is also visible, that the results converged after around 5 epochs, but the training lasted for 30 epochs. As mentioned before, a call-back has been also implemented to restore the weights to match the best validation accuracy during training, to prevent over-fitting.

The results for a chosen measurement case can be seen in Figure 5.12. The analytic estimation is also shown, to be able to compare the results of all three methods. All the other validation results can be found in the Appendix.

It is visible from Figure 5.12, that the analytic estimation results could be the most accurate of the three methods, but the huge oscillations caused by the numerical calculation make the estimated signal noisy. Although the SciML estimation is not inside the interval of 10% relative error, the estimation is much smoother and the accuracy can be considered accurate (taking into account that in the literature there have been no better estimation methods found). And lastly, the neural network estimation provides a smooth, steady signal, however, the SciML implementation improved the results by a significant amount. The averaged RMSE error of the methods for all validation measurements is summarized in Figure 5.13, as well as the computational cost of each method.

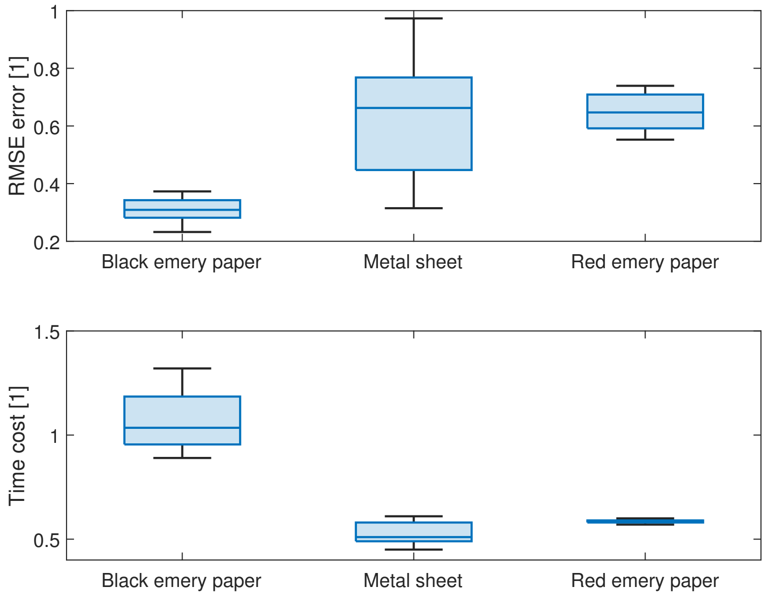

Figure 5.10: Box chart illustration of the estimation error and the time cost with the defined dimensionless time cost quantity.

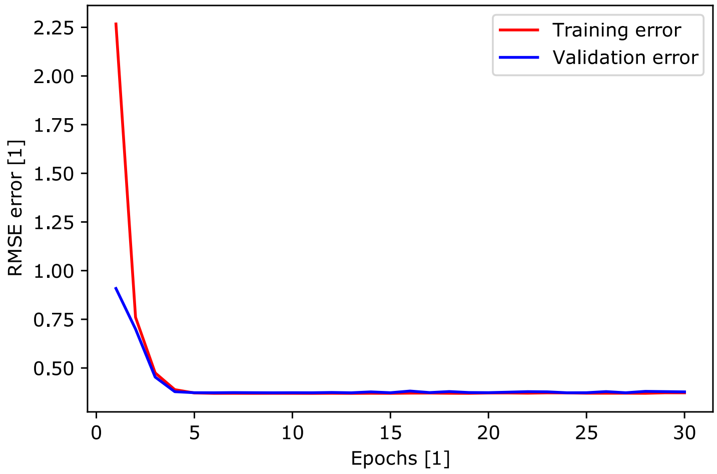

Figure 5.11: Error of the neural network model during training on the measurement data.

Although the error of the analytic estimation can be reduced to nearly half of their value using a SciML method, it is worth mentioning that the simple neural network approach provides moderately accurate estimation with much less computational time, therefore could be ideal for practical applications with real-time data processing. á

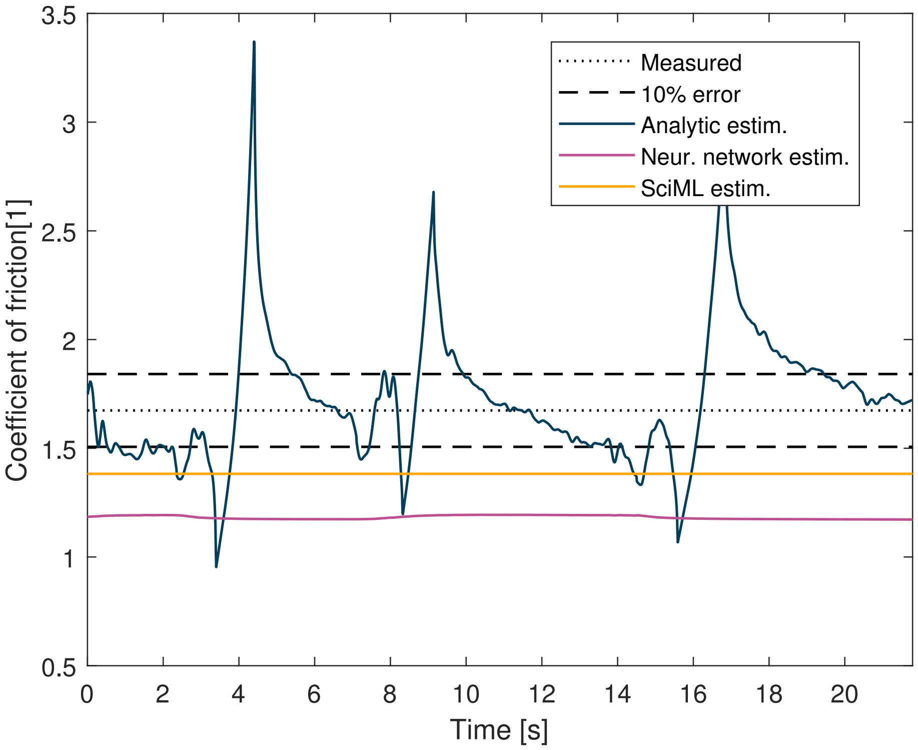

Figure 5.12: Results of the estimation methods for one of the validation measurements. The identified coefficient of friction value with the 10% relative error limits are also shown.

6 Summary

The goal of this thesis was to develop a method that is able to estimate the coefficient of friction between the road surface and elastic tire. In this work, the longitudinal dynamics of the vehicle were neglected, the focus of the thesis was to investigate the situation, when the towing speed is zero, thus only the angular motion is considered. A numerical simulation was successfully created that implements the equations provided by the brush tire model, in order to investigate the relationship between the road and tire surfaces. Then an analytic estimation method was developed for estimating the coefficient of friction based on the brush model. Besides analytic approaches, two machine learning-based algorithms were used to estimate the coefficient of friction. A simple neural network model, as well as a SciML method, that combines data-driven modeling with the physics-based part. All three methods were tested on simulation data, as well as measurement data, gathered by experiments organized by us. An experimental setup was created using already existent measurement equipment as well as custom-designed and manufactured gear. The measurement data was post-processed and transformed into such a form, that the estimation methods could be evaluated using the gathered data. Finally, the conclusions are drawn and some further improvements can be conceived.

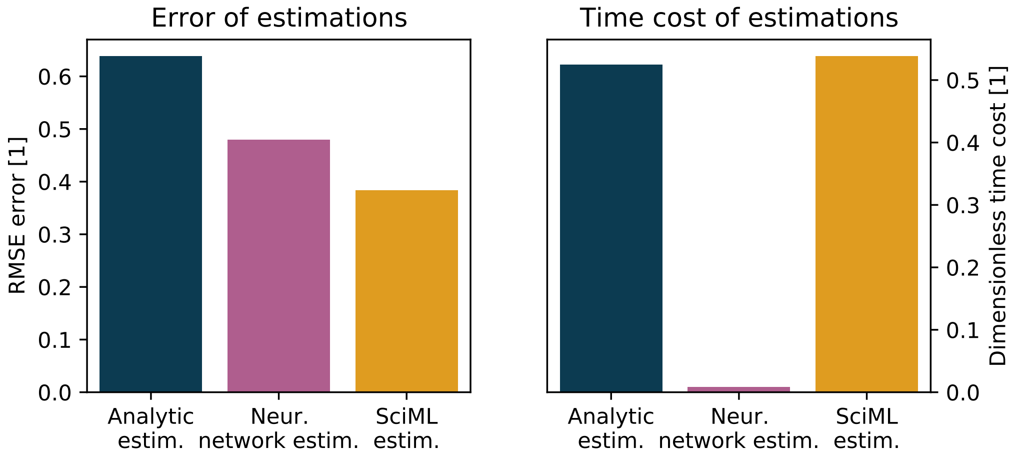

Figure 5.13: Comparing the accuracy of the estimations for the validation measurement cases, as well as the time cost of the computations.

6.1 Results

All three estimation methods were able to estimate the coefficient of friction reliably, using simulation data set. Although the analytic technique showed big oscillations around the desired value, from time to time, the effect of those numerical errors was negligible. The accuracy of the SciML implementation was as good as the accuracy of the analytic algorithm, but more robust, in terms of operational conditions. The analytic method was only derived for less than five fragmented zones in the deformation function of the contact patch, therefore gave false results when more zones were formed. In spite of this, the accuracy of the SciML method was not declined by that much during these conditions. The classical neural network method was not as accurate as the SciML implementation, but provided reasonable estimation with far less computational time.

On measured data, the numerical errors of the analytic calculation method caused much larger oscillations than previously on simulation data, therefore the accuracy of the method declined. The run time of the calculation was reasonable, but would require more modifications to the program for a possible real-time application. The neural network-based estimation proved to be moderately accurate on measurement data, but far less time was needed for the calculations compared to the previously discussed analytic method. And finally, the SciML implementation was the most accurate, but the time cost of the estimation was the largest for this algorithm. The error values, time cost, and robustness properties are summarized in Table 6.1.

	RMSE error [1]	Time cost (dimensionless) [1]	Robustness
Analytic method	0.638	0.525	for the derived cases
Neural network	0.4794	0.0085	✓
SciML method	0.3837	0.538	∼

Table 6.1: Summarized results of each estimation method.

6.2 Outlook, further development

The developed simulation environment modeled the relation of tire and road surface by the brush tire model, which is an accurate model during certain conditions. The performance of the model could be enhanced e.g. by considering different frictional properties in the sticking and sliding region [15]. Another improvement in the simulation accuracy would be to consider a more complex tire model, for example, the stretched string model [14], or a modern tire model [30].

To improve the results of the analytic estimation, some modifications would need to be made in the model. The linearization of the contact patch deformation function around $\psi = 0$ rad made the comparison of the simulation and the analytic calculation more convenient, but the estimation results could be improved by taking into account the nonlinear form of deflections.

The accuracy of the neural network models was optimized by tuning the model parameters of the networks, but the chosen architecture was not modified after a given complexity. The performance of these machine learning models could be even more improved by implementing complex network structures, but the aim of this study was to demonstrate the potential application of neural networks with relatively plain structures. Although the models worked quite well for simulation data, the nominal accuracy was not reached for validation measurements. The literature suggests the use of other machine learning structures (e.g. Gaussian processes [31]) for measurement data sets, because the neural network-based models may not be able to provide accurate solutions for noisy measurement data [3].

Studies have shown that vehicle path prediction [32], vehicle motion control [33] and antilock braking system (ABS) control [34] are more efficient if the estimated coefficient of friction signal is available. Moreover, the end goal of this work was to provide a method for estimating the coefficient of friction, in order to use the knowledge about the frictional characteristics for robust steering control. For precise steering control, the understanding of self-aligning torque (dependent on friction) is essential, thus the proposed estimation methods provide a solid foundation for the above mentioned applications.

Összefoglaló

A szakdolgozat kitűzött célja egy becslő eljárás kifejlesztése volt, mely képes megbecsülni a talaj és egy gumikerék közötti súrlódási együtthatót. A jármű longitudinális dinamikáját elhanyagolva, a gumikerék és a talaj kontakttartományában csupán az oldalirányú elmozdulásokra koncentrálva felállítottam egy numerikus szimulációt, amely segítségével zérus vontatási sebesség mellett is vizsgálható az adott probléma. A szimulációhoz a szakirodalomból vett, úgynevezett kefe gumimodellt használtam, amely egy analitikus modell a kerékben ébredő önbeálló nyomatékának leírására. A szimulációs vizsgálódás után felállítottam egy (szintén a kefe modellen alapuló) analitikus eljárást, amely képes megbecsülni a súrlódási tényezőt. Az analitikus modellek használatán kívül vizsgáltam gépi tanuláson alapuló módszerek alkalmazhatóságát is. Egy egyszerű neurális hálózatot is felállítottam a súrlódási együttható becslésére, mindemelett egy kifejezetten új kutatási terület, a tudományos gép tanulás (az angol "scientific machine learning" kifejezésből röviden: SciML) eredményeit felhasználva egy hibrid modellt is felállítottam. Ez a SciML modell effektíven ötvözi az adat alapú modellezést a fizikai úton történő modellezéssel.

Mindhárom eljárást teszteltem szimulált adatsorokon, és arra a következtetésre jutottam, hogy szimulált környezetben mindhárom metódus megbízható és pontos eredményeket ad. Az analitikus becslésben időnként oszcillációk mutatkoztak, amely numerikus hibákból ered, ám ez a hatás elhanyagolható. A SciML módszer hasonlóan az analitikus módszerhez, pontos becslést szolgáltatott, de robusztusabb megoldásnak bizonyult. Az analitikus megoldás csak olyan esetekre lett levezetve, ahol a kontakttartományban a gumikerék deformációs függvénye legfeljebb öt zónából áll, ennél több deformációs zóna esetén természetesen pontatlan megoldást szolgáltatott, míg a SciML módszert kevésbé befolyásolta ez a körülmény. A neurális hálón alapuló becslés kevésbé pontos, de még elfogadható eredményekhez vezetett, viszont lényegesen kevesebb számítási időre volt szüksége.

Szimulált adatokon kívül mérésekkel is teszteltem a módszerek hatásosságát, ehhez előbb egy mérési eljárás felállítására volt szükség. A Műszaki Mechanikai Tanszéken fellelhető kísérleti felszerelés, valamint egy újonnan gyártatott lefogatási keret felhasználásával méréseket végeztem, hogy vizsgálhassam a gumikerék és talaj közötti kapcsolat súrlódási viszonyainak változását. A mérések által gyűjtött adatokat feldolgozva olyan formára hoztam, hogy bemenő paraméterként felhasználhatóak legyenek mindhárom becslési algoritmus számára.

Mért adatokon tesztelve az analitikus becslés kiértékelésében fellépő numerikus hibák okozta oszcillációk nagyobbá váltak, így a módszer pontossága is csökkent. A szükséges számítási idő elfogadhatónak bizonyult, viszont valós idejű felhasználáshoz még fejleszteni kéne az eljárás gyorsaságán. Kizárólag neurális hálózaton alapuló eljárás esetében közepesen pontos eredményeket kaptam, viszont ki kell emelni a számítási idejét, amely eltörpült a többi eljáráshoz képest. Végezetül a SciML módszer bizonyult a legpontosabbnak, viszont nem meglepő módon ennek a becslési eljárásnak van a legnagyobb számítási

igénye. Így összességében kijelenthető, hogy a szakdolgozat elején kitűzött célok teljesültek, mindhárom kifejlesztett becslési eljárás alkalmas a súrlódási tényező azonosítására kisebb-nagyobb hibákkal. A három eljárást különböző szempontok mentén összehasonlítottam, megállapítottam az egyes metódushoz tartozó előnyöket és hátrányokat, így egy összefoglaló képet kaphattam az elvégzett munka eredményeiről.

Reference

[1] J. Svendenius, *Tire Modeling and Friction Estimation.* PhD thesis, Department of Automatic Control, 2007.

[2] H. B. Pacejka, "Chapter 3 - theory of steady-state slip force and moment generation," in *Tyre and Vehicle Dynamics (Second Edition)*, pp. 90–155, Oxford: Butterworth-Heinemann, 2006.

[3] S. Beregi, D. Barton, D. Rezgui, and S. Neild, "Using scientific machine learning for experimental bifurcation analysis of dynamic systems," workingpaper, Oct. 2021.

[4] Honda, "Riding assist." `https://global.honda/innovation/CES/2017/002.html`. Accessed: 2022-12-04.

[5] BikesRepublic.com, "Honda-riding-assist-motorcycle-self-balancing-01." `https://www.bikesrepublic.com/features/self-balancing-honda-riding-assist-concept-debuts/attachment/honda-riding-assist-motorcycle-self-balancing-01/`. Accessed: 2022-12-06.

[6] C. Ahn, H. Peng, and H. E. Tseng, "Robust estimation of road frictional coefficient," *IEEE Transactions on Control Systems Technology*, vol. 21, no. 1, pp. 1–13, 2013.

[7] T. Kuno and H. Sugiura, "Detection of road conditions with ccd cameras mounted on a vehicle," *Systems and Computers in Japan*, vol. 30, no. 14, pp. 88–99, 1999.

[8] F. Holzmann, M. Bellino, R. Siegwart, and H. Bubb, "Predictive estimation of the road-tire friction coefficient," in *2006 IEEE Conference on Computer Aided Control System Design, 2006 IEEE International Conference on Control Applications, 2006 IEEE International Symposium on Intelligent Control*, pp. 885–890, 2006.

[9] T. Umeno, E. Ono, K. Asano, S. Ito, A. Tanaka, Y. Yasui, and M. Sawada, "Estimation of tire-road friction using tire vibration model," *SAE Transactions*, vol. 111, pp. 1553–1558, 2002.

[10] L. R. RAY, "Nonlinear tire force estimation and road friction identification: Simulation and experiments," *Automatica*, vol. 33, no. 10, pp. 1819–1833, 1997.

[11] K. Nakajima, M. Kurishige, M. Endo, and T. Kifuku, "A vehicle state detection method based on estimated aligning torque using eps," in *SAE 2005 World Congress and Exhibition*, SAE International, apr 2005.

[12] Y. Yasui, W. Tanaka, Y. Muragishi, E. Ono, M. Momiyama, H. Katoh, H. Aizawa, and Y. Imoto, "Estimation of lateral grip margin based on self-aligning torque for vehicle dynamics enhancement," 03 2004.

[13] B. M. Györök, “Estimating the coefficient of friction based on the memory effect of an elastic tire,” *Budapest University of Technology and Economics, Students’ Scientific Conference*, 2022.

[14] H. B. Pacejka, “Chapter 5 - non-steady-state out-of-plane string-based tire models,” in *Tire and Vehicle Dynamics (Third Edition)* (H. B. Pacejka, ed.), pp. 211–286, Oxford: Butterworth-Heinemann, third edition ed., 2012.

[15] A. O’Neill, J. Prins, J. F. Watts, and P. Gruber, “Enhancing brush tyre model accuracy through friction measurements,” *Vehicle System Dynamics*, vol. 60, no. 6, pp. 2075–2097, 2022.

[16] MathWorks, “Solve system of nonlinear equations - MATLAB.” `https://www.mathworks.com/help/optim/ug/fsolve.html?s_tid=srchtitle_fsolve_1`. Accessed: 2022-10-29.

[17] M. Altrichter, G. Horváth, B. Pataki, G. Strausz, G. Takács, and V. József, *Neurális hálózatok*. Panem Kft., 2006.

[18] Á. Antal and B. M. Györök, “Központi idegrendszer működésének modellezése neurális hálóval egy helyben állás közben,” *Budapesti Műszaki és Gazdaságtudományi Egyetem, Tudományos Diákköri Konferencia*, 2021.

[19] A. Geron, *Hands-on machine learning with Scikit-Learn and TensorFlow: concepts, tools, and techniques to build intelligent systems*. Sebastopol, CA: O’Reilly Media, 2017.

[20] M. Abadi, P. Barham, J. Chen, Z. Chen, A. Davis, J. Dean, M. Devin, S. Ghemawat, G. Irving, M. Isard, M. Kudlur, J. Levenberg, R. Monga, S. Moore, D. G. Murray, B. Steiner, P. Tucker, V. Vasudevan, P. Warden, M. Wicke, Y. Yu, and X. Zheng, “Tensorflow: A system for large-scale machine learning,” in *Proceedings of the 12th USENIX Conference on Operating Systems Design and Implementation*, OSDI’16, (USA), p. 265–283, USENIX Association, 2016.

[21] A. Gulli and S. Pal, *Deep learning with Keras*. Packt Publishing Ltd, 2017.

[22] D. Masters and C. Luschi, “Revisiting small batch training for deep neural networks,” 2018.

[23] N. Baker, F. Alexander, T. Bremer, A. Hagberg, Y. Kevrekidis, H. Najm, M. Parashar, A. Patra, J. Sethian, S. Wild, K. Willcox, and S. Lee, “Workshop report on basic research needs for scientific machine learning: Core technologies for artificial intelligence,” 2 2019.

[24] C. Rackauckas, Y. Ma, J. Martensen, C. Warner, K. Zubov, R. Supekar, D. Skinner, and A. Ramadhan, “Universal differential equations for scientific machine learning,” *arXiv preprint arXiv:2001.04385*, 2020.

[25] D. Takács, G. Orosz, and G. Stépán, “Delay effects in shimmy dynamics of wheels with stretched string-like tyres,” *European Journal of Mechanics A-solids*, vol. 28, pp. 516–525, 2009.

[26] S. Beregi, D. Takacs, G. Gyebroszki, and G. Stepan, “Theoretical and experimental study on the nonlinear dynamics of wheel-shimmy,” *Nonlinear Dynamics*, vol. 98, p. 2581–2593, Sep 2019.

[27] G. Csernák and G. Stépán, *Rezgéstan.* Budapesti Műszaki és Gazdaságtudományi Egyetem Műszaki Mechanikai Tanszék, 2019.

[28] D. Takács and G. Stépán, “Experiments on quasiperiodic wheel shimmy,” *Journal of Computational and Nonlinear Dynamics - J COMPUT NONLINEAR DYN*, vol. 4, 07 2009.

[29] P. LLC, “Exponential filter.” `https://gregstanleyandassociates.com/whitepapers/FaultDiagnosis/Filtering/Exponential-Filter/exponential-filter.htm`. Accessed: 2022-12-08.

[30] C. Oertel and A. Fandre, “Rmod-k tyre model system,” *ATZ worldwide*, vol. 103, 11 2001.

[31] C. E. Rasmussen and C. K. I. Williams, *Gaussian Processes for Machine Learning.* The MIT Press, 11 2005.

[32] C.-S. L. G. student and H. P. A. Professor, “Road friction coefficient estimation for vehicle path prediction,” *Vehicle System Dynamics*, vol. 25, no. sup1, pp. 413–425, 1996.

[33] K. B. Singh and S. Taheri, “Estimation of tire–road friction coefficient and its application in chassis control systems,” *Systems Science & Control Engineering*, vol. 3, no. 1, pp. 39–61, 2015.

[34] S. Rajendran, S. K. Spurgeon, G. Tsampardoukas, and R. Hampson, “Estimation of road frictional force and wheel slip for effective antilock braking system (abs) control,” *International Journal of Robust and Nonlinear Control*, vol. 29, no. 3, pp. 736–765, 2019.

Appendix

The created scripts

All the scripts that are created for the estimation methods can be found here: `https://github.com/gyorokbendeguz/BSc-Thesis` .

The Matlab scripts related to the simulation environment and the analytic estimation can be found in the `BrushSim` directory, the Jupyter notebook files related to the machine learning-based techniques can be found in the `MachineLearning` directory.

Deformation function parameters for three fragmentation zones

The points, where the sticking region turns into sliding, can be expressed as

$$x_{\mathrm{R}} = -\frac{a\left(\sqrt{9\,{F_N}^2\,\mu^2+4\,a^4\,k^2\,\psi^2-12\,F_N\,a\,e\,k\,\mu\,\psi\,\mathrm{sign}\left(\psi\right)}-2\,a^2\,k\,\psi\,\mathrm{sign}\left(\psi\right)\right)}{3\,F_N\,\mu},$$

$$x_{\mathrm{L}} = \frac{a\left(\sqrt{9\,{F_N}^2\,\mu^2+4\,a^4\,k^2\,\psi^2+12\,F_N\,a\,e\,k\,\mu\,\psi\,\mathrm{sign}\left(\psi\right)}-2\,a^2\,k\,\psi\,\mathrm{sign}\left(\psi\right)\right)}{3\,F_N\,\mu}.$$

Deformation function parameters for five fragmentation zones

The parameters of the deformation function with five zones, in case of positive angular direction can be expressed as

$$x_{\mathrm{R}}^* = -\frac{a\left(\sqrt{9\,{F_N}^2\,\mu^2+4\,a^4\,k^2\,{\psi_{\max}}^2-12\,F_N\,a\,e\,k\,\mu\,\psi_{\max}\,\mathrm{sign}\left(\psi_{\max}\right)}-2\,a^2\,k\,\psi_{\max}\,\mathrm{sign}\left(\psi_{\max}\right)\right)}{3\,F_N\,\mu},$$

$$x_{\mathrm{L}}^* = \frac{a\left(\sqrt{9\,{F_N}^2\,\mu^2+4\,a^4\,k^2\,{\psi_{\max}}^2+12\,F_N\,a\,e\,k\,\mu\,\psi_{\max}\,\mathrm{sign}\left(\psi_{\max}\right)}-2\,a^2\,k\,\psi_{\max}\,\mathrm{sign}\left(\psi_{\max}\right)\right)}{3\,F_N\,\mu},$$

$$m_{\mathrm{R}} = -\frac{\mathrm{num}\left(m_{\mathrm{R}}\right)}{\mathrm{denum}\left(m_{\mathrm{R}}\right)},$$

$$\begin{aligned}
\mathrm{num}\left(m_{\mathrm{R}}\right) = {} & e\,\psi + \\
& + \frac{3\,F_N\,\mu\left(a^2-\frac{a^2\left(\sqrt{9\,{F_N}^2\,\mu^2+4\,a^4\,k^2\,{\psi_{\max}}^2-12\,F_N\,a\,e\,k\,\mu\,\psi_{\max}\,\mathrm{sign}(\psi_{\max})}-2\,a^2\,k\,\psi_{\max}\,\mathrm{sign}(\psi_{\max})\right)^2}{9\,{F_N}^2\,\mu^2}\right)}{4\,a^3\,k} + \\
& + \frac{a\,\psi\left(\sqrt{9\,{F_N}^2\,\mu^2+4\,a^4\,k^2\,{\psi_{\max}}^2-12\,F_N\,a\,e\,k\,\mu\,\psi_{\max}\,\mathrm{sign}\left(\psi_{\max}\right)}-2\,a^2\,k\,\psi_{\max}\,\mathrm{sign}\left(\psi_{\max}\right)\right)}{3\,F_N\,\mu}
\end{aligned}$$

$$\mathrm{denum}\left(m_{\mathrm{R}}\right)=e+$$

$$+\frac{0.3333\,a\,\left(\sqrt{9\,{F_N}^2\,\mu^2+4\,a^4\,k^2\,{\psi_{\max}}^2-12\,F_N\,a\,e\,k\,\mu\,\psi_{\max}\,\mathrm{sign}\left(\psi_{\max}\right)}-2\,a^2\,k\,\psi_{\max}\,\mathrm{sign}\left(\psi_{\max}\right)\right)}{F_N\,\mu},$$

$$m_{\mathrm{L}}=\frac{\mathrm{num}\left(m_{\mathrm{L}}\right)}{\mathrm{denum}\left(m_{\mathrm{L}}\right)},$$

$$\mathrm{num}\left(m_{\mathrm{L}}\right)=\frac{3\,F_N\,\mu\,\left(a^2-\frac{a^2\,\left(\sqrt{9\,{F_N}^2\,\mu^2+4\,a^4\,k^2\,{\psi_{\max}}^2+12\,F_N\,a\,e\,k\,\mu\,\psi_{\max}\,\mathrm{sign}(\psi_{\max})}-2\,a^2\,k\,\psi_{\max}\,\mathrm{sign}(\psi_{\max})\right)^2}{9\,{F_N}^2\,\mu^2}\right)}{4\,a^3\,k}-$$

$$-e\,\psi+\frac{a\,\psi\,\left(\sqrt{9\,{F_N}^2\,\mu^2+4\,a^4\,k^2\,{\psi_{\max}}^2+12\,F_N\,a\,e\,k\,\mu\,\psi_{\max}\,\mathrm{sign}\left(\psi_{\max}\right)}-2\,a^2\,k\,\psi_{\max}\,\mathrm{sign}\left(\psi_{\max}\right)\right)}{3\,F_N\,\mu},$$

$$\mathrm{denum}\left(m_{\mathrm{L}}\right)=e-$$

$$-\frac{0.3333\,a\,\left(\sqrt{9\,{F_N}^2\,\mu^2+4\,a^4\,k^2\,{\psi_{\max}}^2+12\,F_N\,a\,e\,k\,\mu\,\psi_{\max}\,\mathrm{sign}\left(\psi_{\max}\right)}-2\,a^2\,k\,\psi_{\max}\,\mathrm{sign}\left(\psi_{\max}\right)\right)}{F_N\,\mu},$$

$$x_{\mathrm{R}}=\frac{a^3\,k\,\left(\frac{\sigma_1}{\sigma_2}-\sqrt{\frac{{\sigma_1}^2}{{\sigma_2}^2}-\frac{6\,F_N\,\mu\,\left(\frac{e\,\sigma_1}{\sigma_2}-\frac{3\,F_N\,\mu}{2\,a\,k}\right)}{a^3\,k}}\right)}{F_N\,\mu},$$

$$\sigma_1=e\,\psi+\frac{3\,F_N\,\mu\,\left(a^2-\frac{a^2\,{\sigma_3}^2}{9\,{F_N}^2\,\mu^2}\right)}{4\,a^3\,k},$$

$$\sigma_2=e+\frac{a\,\sigma_3}{3\,F_N\,\mu},$$

$$\sigma_3=\sqrt{9\,{F_N}^2\,\mu^2+4\,a^4\,k^2\,{\psi_{\max}}^2-12\,F_N\,a\,e\,k\,\mu\,\psi_{\max}\,\mathrm{sign}\left(\psi_{\max}\right)}-2\,a^2\,k\,\psi_{\max}\,\mathrm{sign}\left(\psi_{\max}\right),$$

$$x_{\mathrm{L}}=\frac{a^3\,k\,\left(\frac{\sigma_4}{\sigma_5}+\sqrt{\frac{{\sigma_4}^2}{{\sigma_5}^2}-\frac{6\,F_N\,\mu\,\left(\frac{e\,\sigma_4}{\sigma_5}-\frac{3\,F_N\,\mu}{2\,a\,k}\right)}{a^3\,k}}\right)}{F_N\,\mu},$$

$$\sigma_4=-e\,\psi+\frac{3\,F_N\,\mu\,\left(a^2-\frac{a^2\,{\sigma_6}^2}{9\,{F_N}^2\,\mu^2}\right)}{4\,a^3\,k},$$

$$\sigma_5=e-\frac{a\,\sigma_3}{3\,F_N\,\mu},$$

$$\sigma_6=\sqrt{9\,{F_N}^2\,\mu^2+4\,a^4\,k^2\,{\psi_{\max}}^2+12\,F_N\,a\,e\,k\,\mu\,\psi_{\max}\,\mathrm{sign}\left(\psi_{\max}\right)}-2\,a^2\,k\,\psi_{\max}\,\mathrm{sign}\left(\psi_{\max}\right).$$

And then, the parameters of the deformation function with five zones, in case of negative angular direction can be expressed as

$$x_{\mathrm{R}}^{*} = -\frac{a\left(\sqrt{9\,{F_N}^2\,\mu^2 + 4\,a^4\,k^2\,{\psi_{\max}}^2 - 12\,F_N\,a\,e\,k\,\mu\,\psi_{\max}\,\mathrm{sign}\left(\psi_{\max}\right)} - 2\,a^2\,k\,\psi_{\max}\,\mathrm{sign}\left(\psi_{\max}\right)\right)}{3\,F_N\,\mu},$$

$$x_{\mathrm{L}}^{*} = \frac{a\left(\sqrt{9\,{F_N}^2\,\mu^2 + 4\,a^4\,k^2\,{\psi_{\max}}^2 + 12\,F_N\,a\,e\,k\,\mu\,\psi_{\max}\,\mathrm{sign}\left(\psi_{\max}\right)} - 2\,a^2\,k\,\psi_{\max}\,\mathrm{sign}\left(\psi_{\max}\right)\right)}{3\,F_N\,\mu},$$

$$m_{\mathrm{R}} = -\frac{\mathrm{num}\left(m_{\mathrm{R}}\right)}{\mathrm{denum}\left(m_{\mathrm{R}}\right)},$$

$$\mathrm{num}\left(m_{\mathrm{R}}\right) = e\,\psi - \\ -\frac{3\,F_N\,\mu\left(a^2 - \frac{a^2\left(\sqrt{9\,{F_N}^2\,\mu^2+4\,a^4\,k^2\,{\psi_{\max}}^2-12\,F_N\,a\,e\,k\,\mu\,\psi_{\max}\,\mathrm{sign}(\psi_{\max})}-2\,a^2\,k\,\psi_{\max}\,\mathrm{sign}(\psi_{\max})\right)^2}{9\,{F_N}^2\,\mu^2}\right)}{4\,a^3\,k} + \\ +\frac{a\,\psi\left(\sqrt{9\,{F_N}^2\,\mu^2 + 4\,a^4\,k^2\,{\psi_{\max}}^2 - 12\,F_N\,a\,e\,k\,\mu\,\psi_{\max}\,\mathrm{sign}\left(\psi_{\max}\right)} - 2\,a^2\,k\,\psi_{\max}\,\mathrm{sign}\left(\psi_{\max}\right)\right)}{3\,F_N\,\mu},$$

$$\mathrm{denum}\left(m_{\mathrm{R}}\right) = e + \\ +\frac{a\left(\sqrt{9\,{F_N}^2\,\mu^2 + 4\,a^4\,k^2\,{\psi_{\max}}^2 - 12\,F_N\,a\,e\,k\,\mu\,\psi_{\max}\,\mathrm{sign}\left(\psi_{\max}\right)} - 2\,a^2\,k\,\psi_{\max}\,\mathrm{sign}\left(\psi_{\max}\right)\right)}{3\,F_N\,\mu},$$

$$m_{\mathrm{L}} = -\frac{\mathrm{num}\left(m_{\mathrm{L}}\right)}{\mathrm{denum}\left(m_{\mathrm{L}}\right)},$$

$$\mathrm{num}\left(m_{\mathrm{L}}\right) = e\,\psi + \\ +\frac{3F_N\,\mu\left(a^2 - \frac{a^2\left(\sqrt{9\,{F_N}^2\,\mu^2+4\,a^4\,k^2\,{\psi_{\max}}^2+12\,F_N\,a\,e\,k\,\mu\,\psi_{\max}\,\mathrm{sign}(\psi_{\max})}-2\,a^2\,k\,\psi_{\max}\,\mathrm{sign}(\psi_{\max})\right)^2}{9\,{F_N}^2\,\mu^2}\right)}{4\,a^3\,k} - \\ -\frac{a\,\psi\left(\sqrt{9\,{F_N}^2\,\mu^2 + 4\,a^4\,k^2\,{\psi_{\max}}^2 + 12\,F_N\,a\,e\,k\,\mu\,\psi_{\max}\,\mathrm{sign}\left(\psi_{\max}\right)} - 2\,a^2\,k\,\psi_{\max}\,\mathrm{sign}\left(\psi_{\max}\right)\right)}{3\,F_N\,\mu},$$

$$\mathrm{denum}\left(m_{\mathrm{L}}\right) = e - \\ -\frac{a\left(\sqrt{9\,{F_N}^2\,\mu^2 + 4\,a^4\,k^2\,{\psi_{\max}}^2 + 12\,F_N\,a\,e\,k\,\mu\,\psi_{\max}\,\mathrm{sign}\left(\psi_{\max}\right)} - 2\,a^2\,k\,\psi_{\max}\,\mathrm{sign}\left(\psi_{\max}\right)\right)}{3\,F_N\,\mu},$$

$$
\begin{aligned}
x_{\mathrm{R}} &= -\frac{a^3\,k\,\left(\frac{\sigma_7}{\sigma_8}+\sqrt{\frac{{\sigma_7}^2}{{\sigma_8}^2}+\frac{6\,F_N\,\mu\,\left(\frac{e\,\sigma_7}{\sigma_8}+\frac{3\,F_N\,\mu}{2\,a\,k}\right)}{a^3\,k}}\right)}{3\,F_N\,\mu},\\
\sigma_7 &= e\,\psi-\frac{3\,F_N\,\mu\,\left(a^2-\frac{a^2\,{\sigma_9}^2}{9\,{F_N}^2\,\mu^2}\right)}{4\,a^3\,k}+\frac{a\,\psi\,\sigma_9}{F_N\,\mu},\\
\sigma_8 &= e+\frac{a\,\sigma_9}{3\,F_N\,\mu},\\
\sigma_9 &= \sqrt{9\,{F_N}^2\,\mu^2+4\,a^4\,k^2\,{\psi_{\mathrm{max}}}^2-12\,F_N\,a\,e\,k\,\mu\,\psi_{\mathrm{max}}\,\mathrm{sign}\left(\psi_{\mathrm{max}}\right)}-2\,a^2\,k\,\psi_{\mathrm{max}}\,\mathrm{sign}\left(\psi_{\mathrm{max}}\right),\\
x_{\mathrm{L}} &= -\frac{a^3\,k\,\left(\frac{\sigma_{10}}{\sigma_{11}}+\sqrt{\frac{{\sigma_{10}}^2}{{\sigma_{11}}^2}-\frac{6\,F_N\,\mu\,\left(\frac{e\,\sigma_{10}}{\sigma_{11}}-\frac{3\,F_N\,\mu}{2\,a\,k}\right)}{a^3\,k}}\right)}{3\,F_N\,\mu},\\
\sigma_{10} &= e\,\psi+\frac{3\,F_N\,\mu\,\left(a^2-\frac{a^2\,{\sigma_{12}}^2}{9\,{F_N}^2\,\mu^2}\right)}{4\,a^3\,k}-\frac{a\,\psi\,\sigma_{12}}{F_N\,\mu},\\
\sigma_{11} &= e-\frac{a\,\sigma_{12}}{3\,F_N\,\mu},\\
\sigma_{12} &= \sqrt{9\,{F_N}^2\,\mu^2+4\,a^4\,k^2\,{\psi_{\mathrm{max}}}^2+12\,F_N\,a\,e\,k\,\mu\,\psi_{\mathrm{max}}\,\mathrm{sign}\left(\psi_{\mathrm{max}}\right)}-2\,a^2\,k\,\psi_{\mathrm{max}}\,\mathrm{sign}\left(\psi_{\mathrm{max}}\right),
\end{aligned}
$$

where $\sigma_1 \ldots \sigma_{12}$ are parameters created, in order to ease the description of the given expressions.

Analytic estimation results for simulated data

The results of the analytic estimation for simulated data, are shown here (only those cases, that were not showed in the documentation).

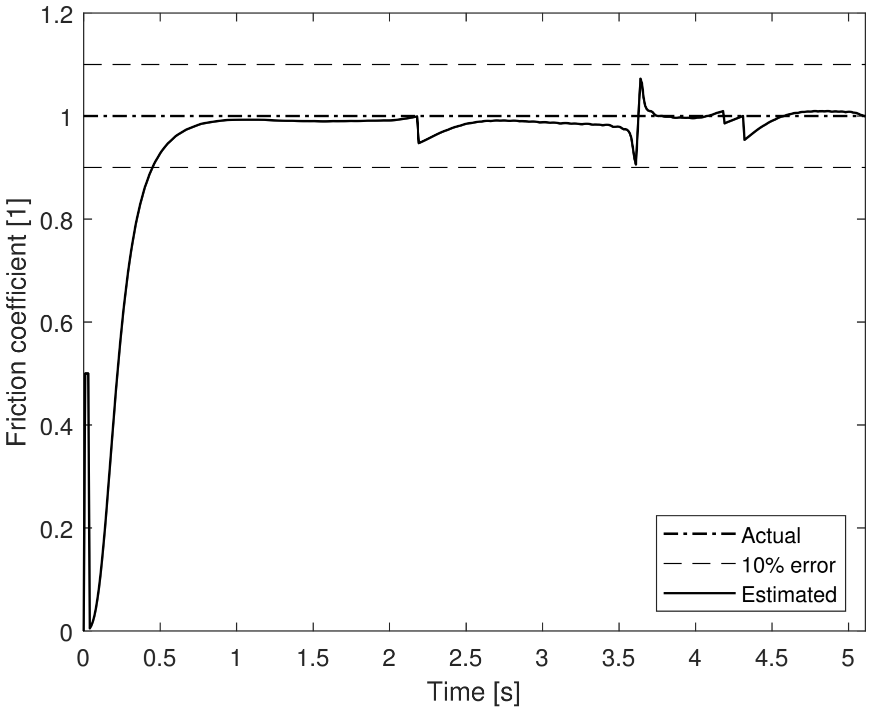

Figure 6.1: Analytic coefficient of friction estimation with simulated data for $\mu = 1$.

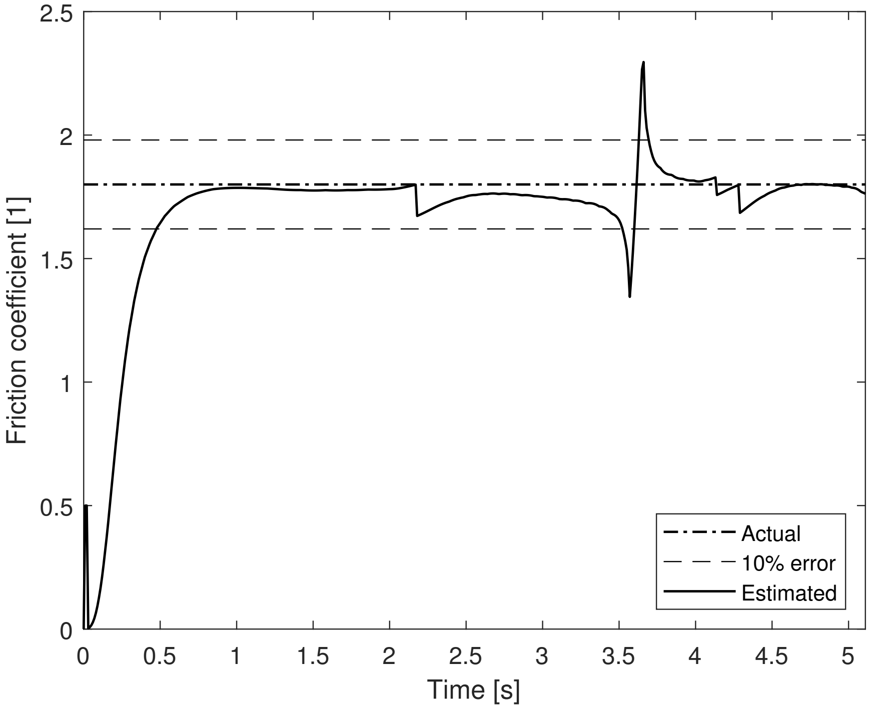

Figure 6.2: Analytic coefficient of friction estimation with simulated data for $\mu = 1.8$.

Analytic estimation results for measured data

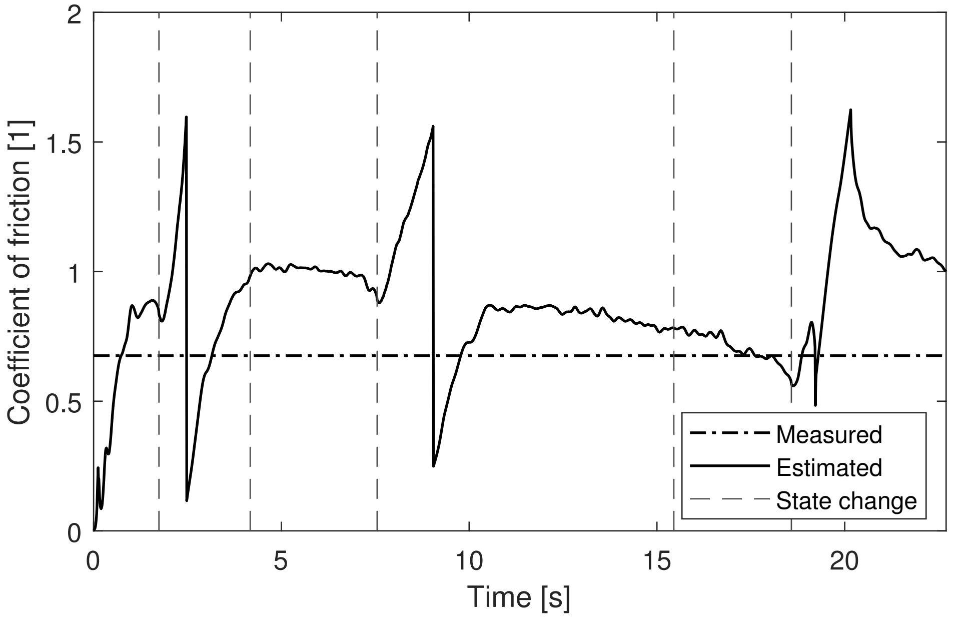

Figure 6.3: Estimation results, for the black emery paper, with contact patch half-length of $a = 40$ mm

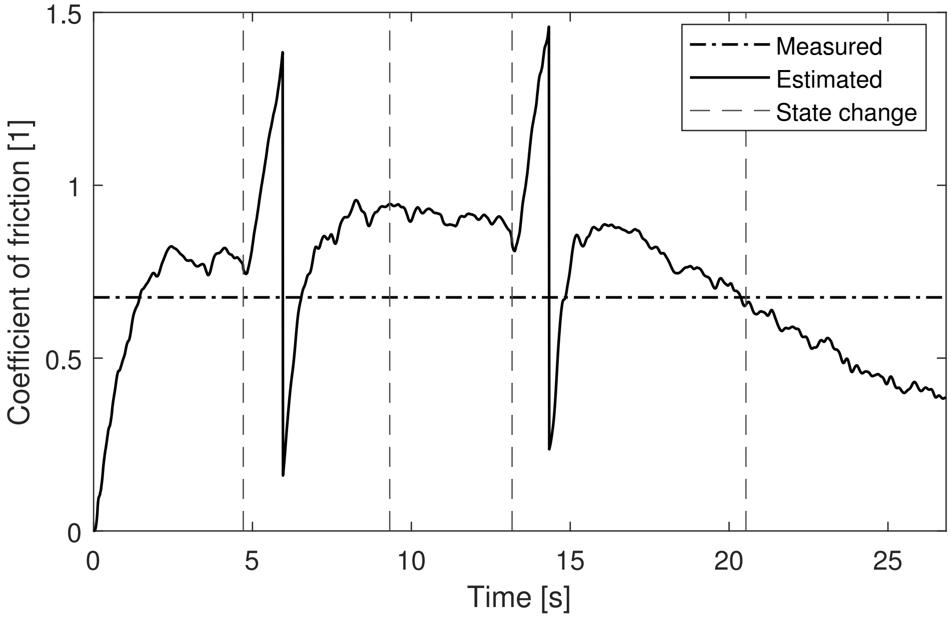

Figure 6.4: Estimation results, for the black emery paper, with contact patch half-length of $a = 40$ mm

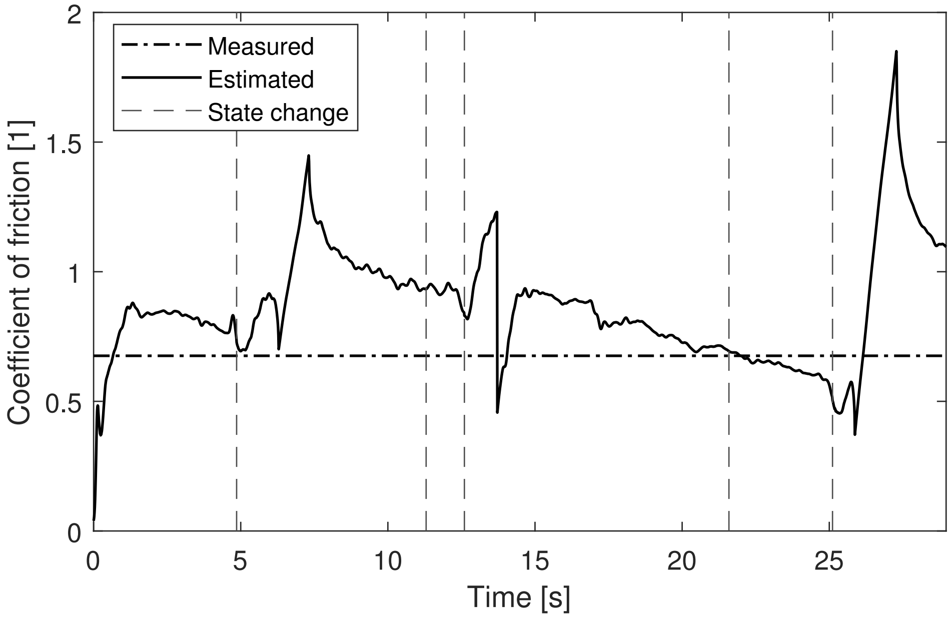

Figure 6.5: Estimation results, for the black emery paper, with contact patch half-length of $a = 40$ mm

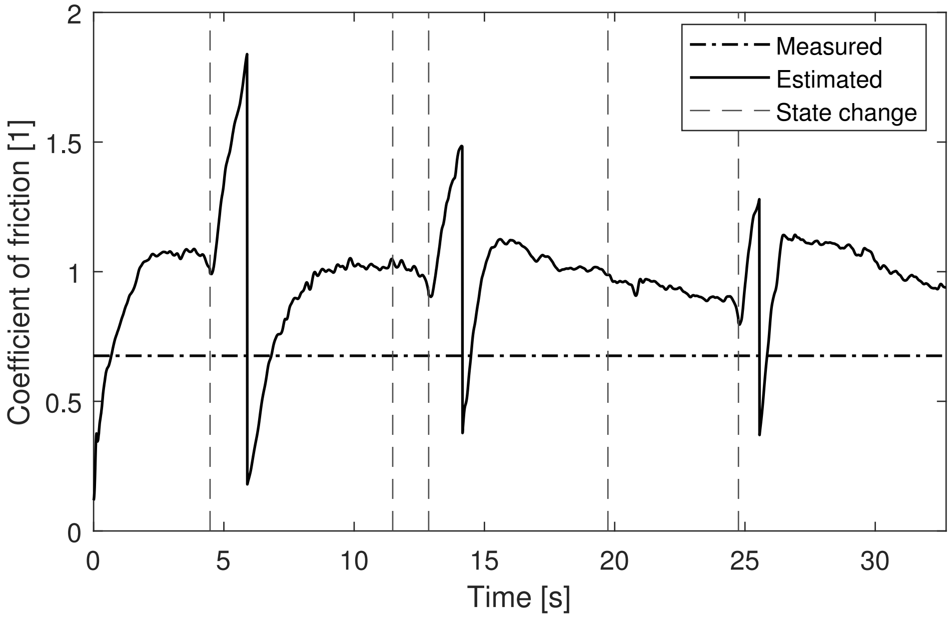

Figure 6.6: Estimation results, for the black emery paper, with contact patch half-length of $a = 45$ mm

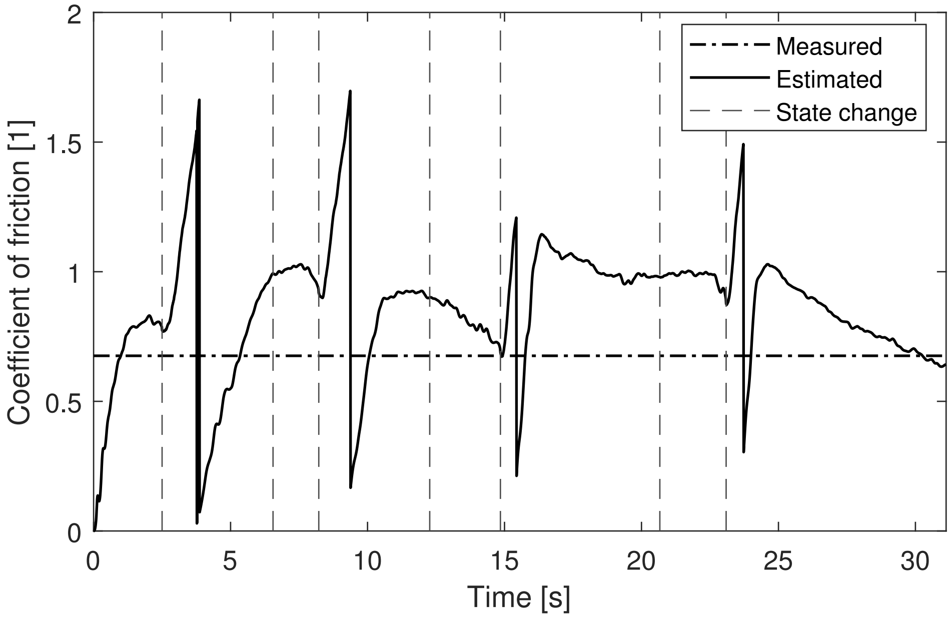

Figure 6.7: Estimation results, for the black emery paper, with contact patch half-length of $a = 45$ mm

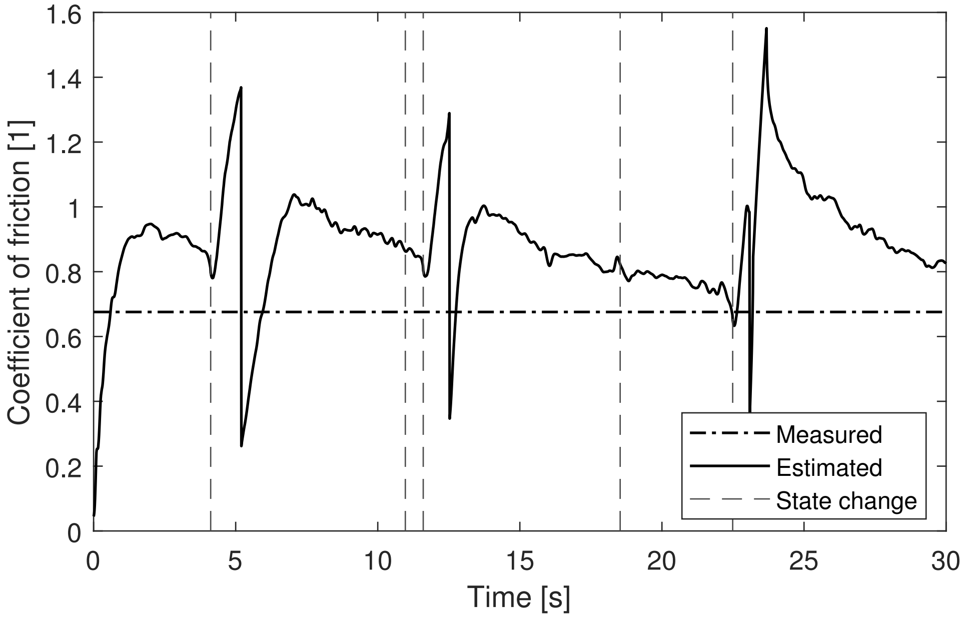

Figure 6.8: Estimation results, for the black emery paper, with contact patch half-length of $a = 45$ mm

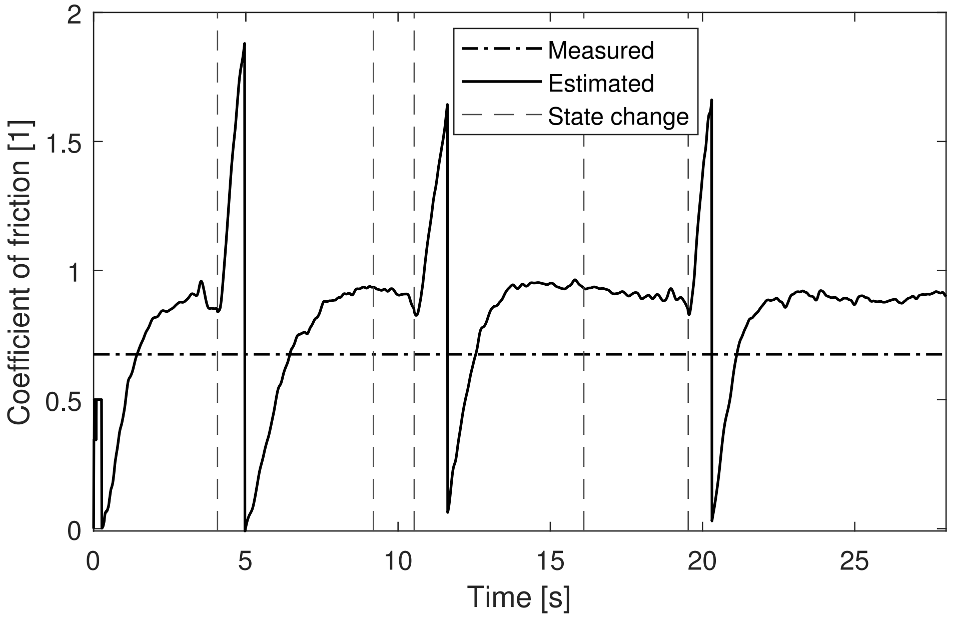

Figure 6.9: Estimation results, for the black emery paper, with contact patch half-length of $a = 50$ mm

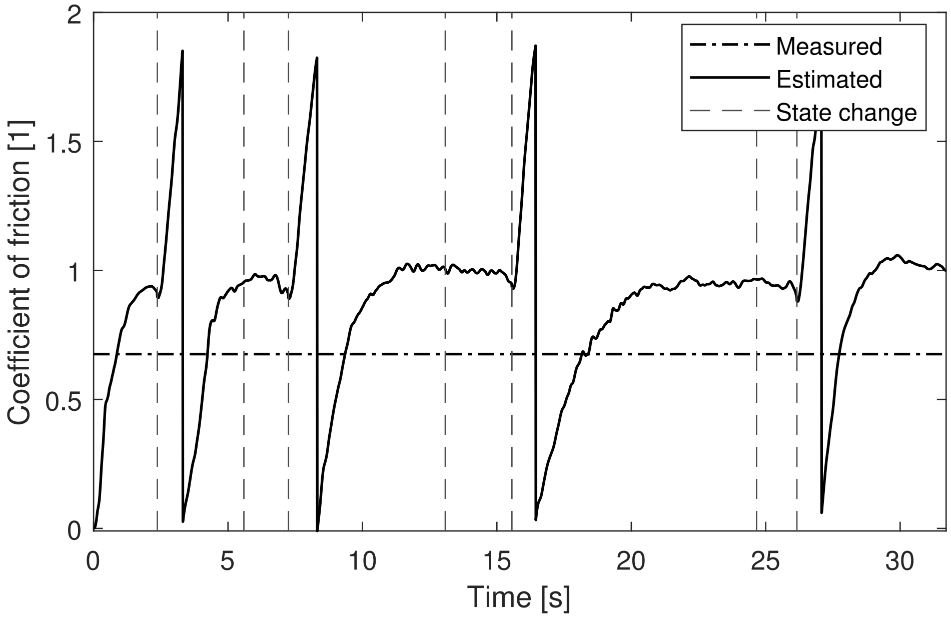

Figure 6.10: Estimation results, for the black emery paper, with contact patch half-length of $a = 50$ mm

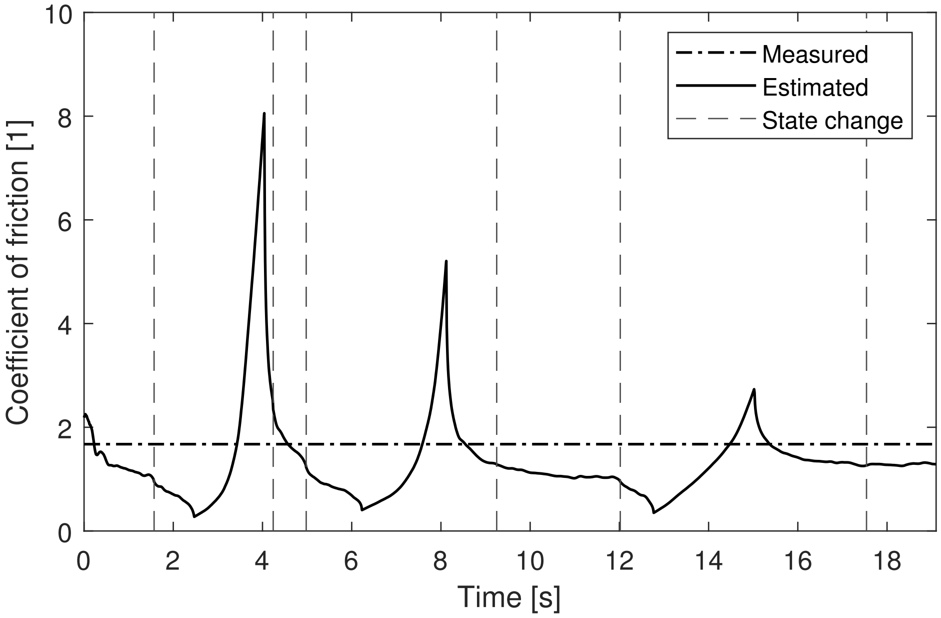

Figure 6.11: Estimation results, for the metal sheet, with contact patch half-length of $a = 40$ mm

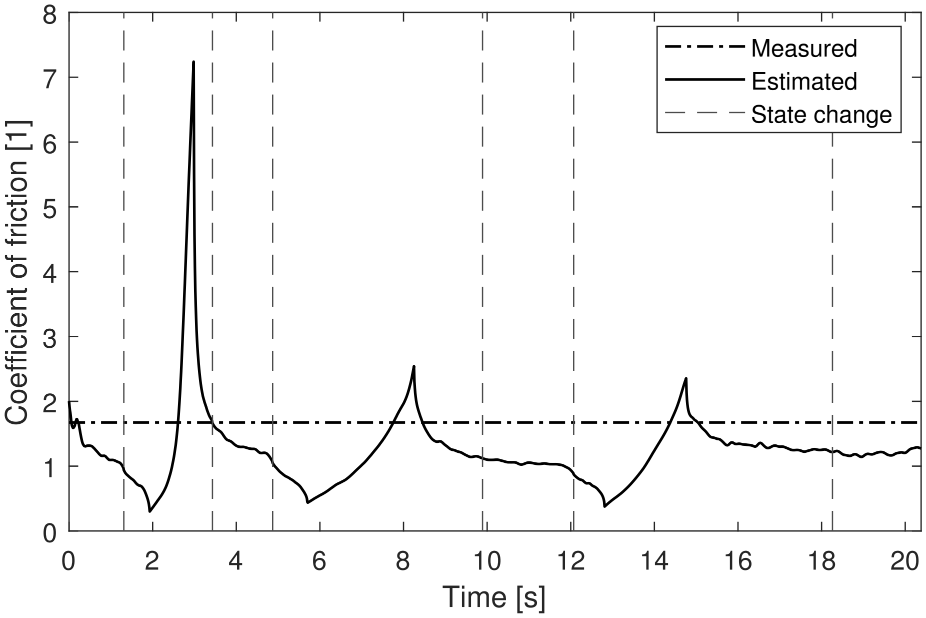

Figure 6.12: Estimation results, for the metal sheet, with contact patch half-length of $a = 40$ mm

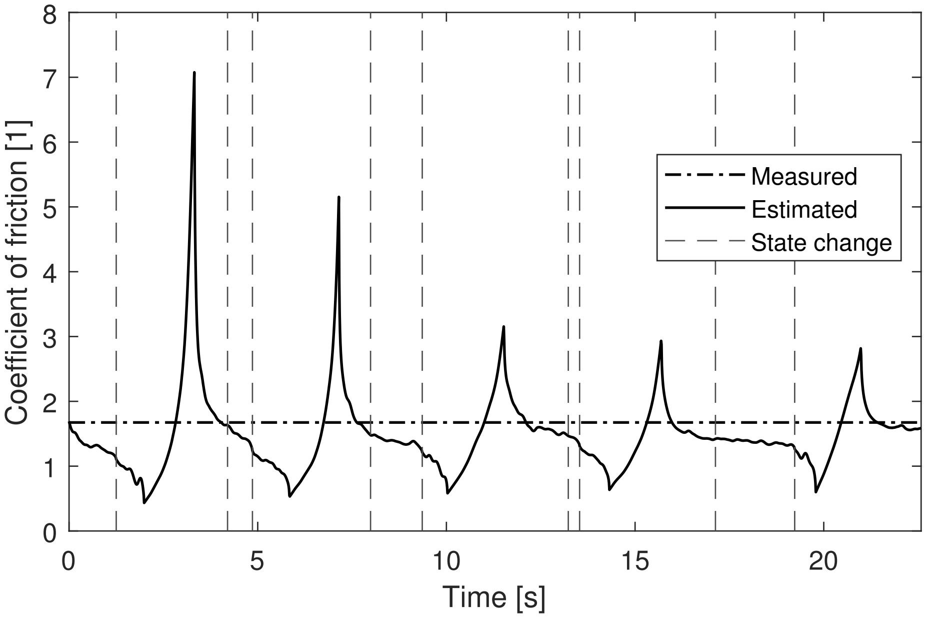

Figure 6.13: Estimation results, for the metal sheet, with contact patch half-length of $a = 45$ mm

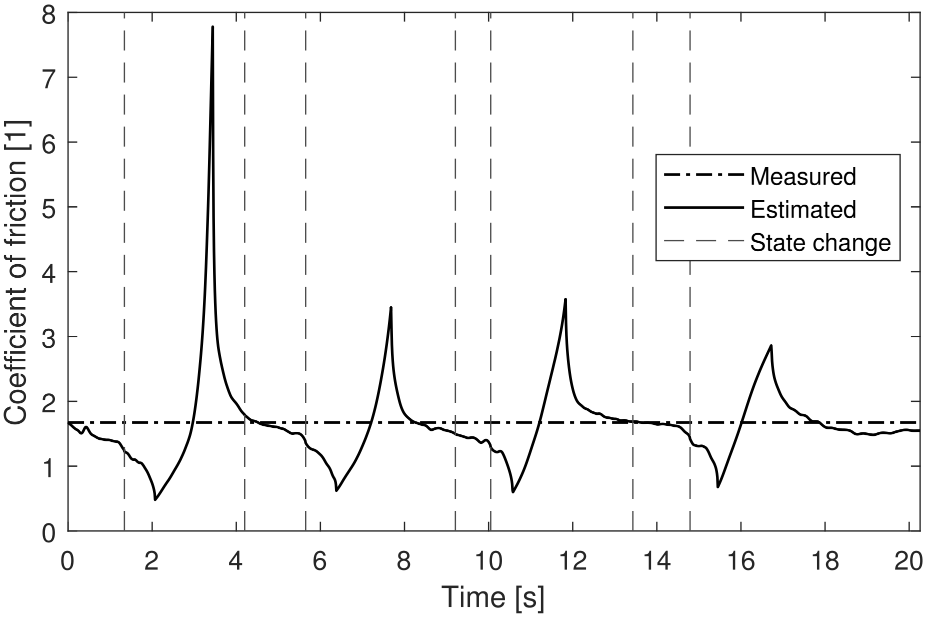

Figure 6.14: Estimation results, for the metal sheet, with contact patch half-length of $a = 45$ mm

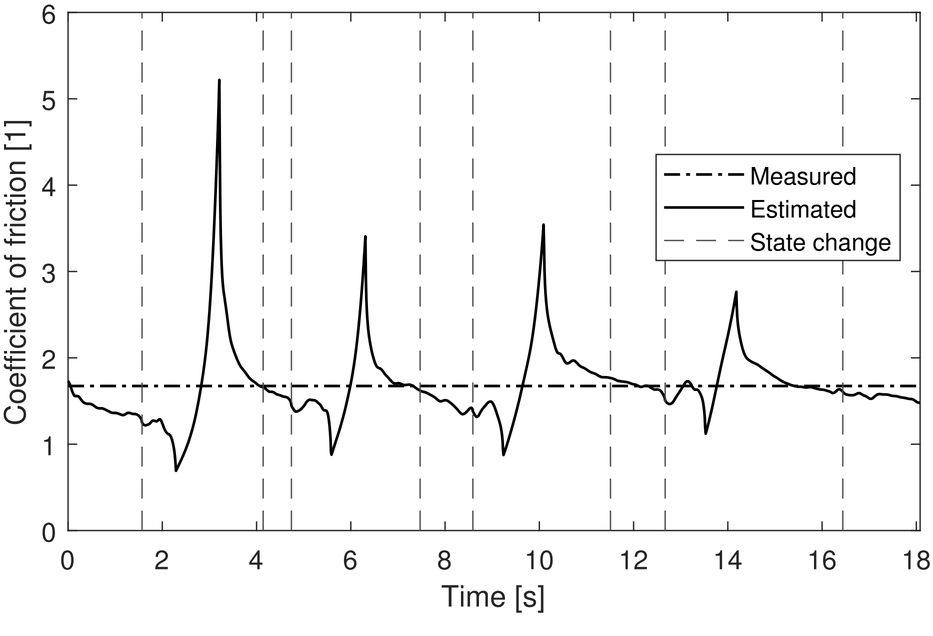

Figure 6.15: Estimation results, for the metal sheet, with contact patch half-length of $a = 50$ mm

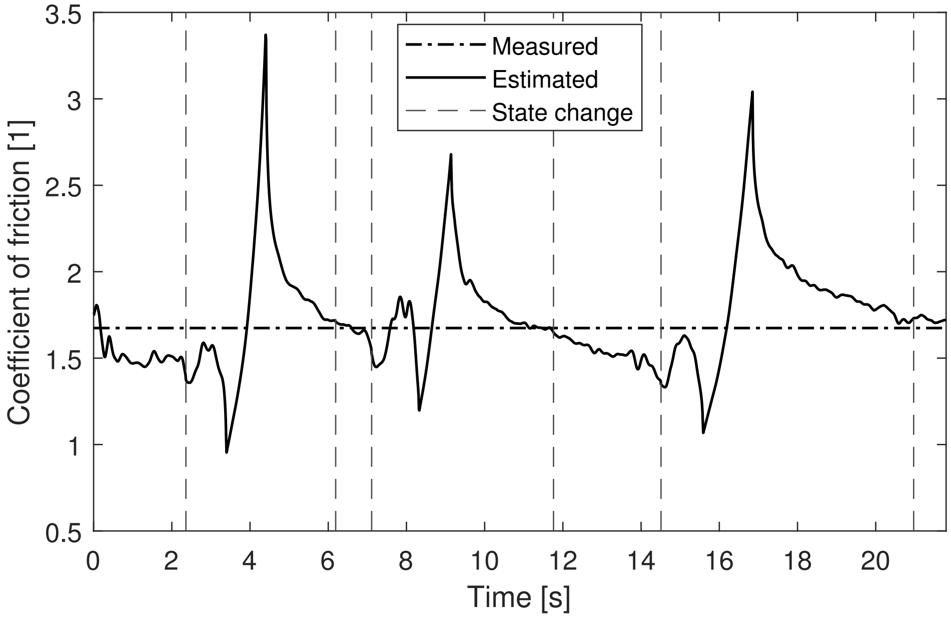

Figure 6.16: Estimation results, for the metal sheet, with contact patch half-length of $a = 50$ mm

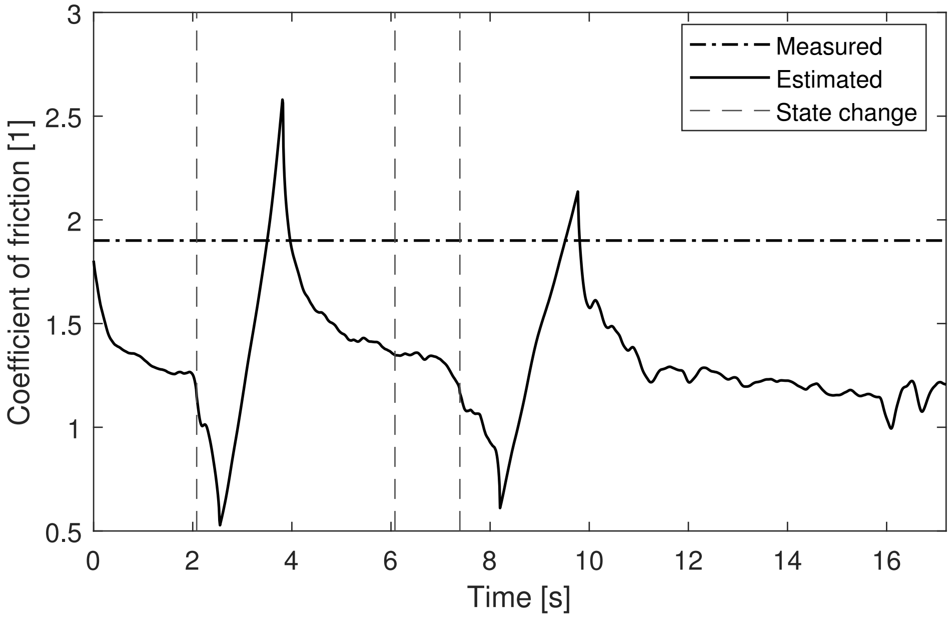

Figure 6.17: Estimation results, for the red emery paper, with contact patch half-length of $a = 40$ mm

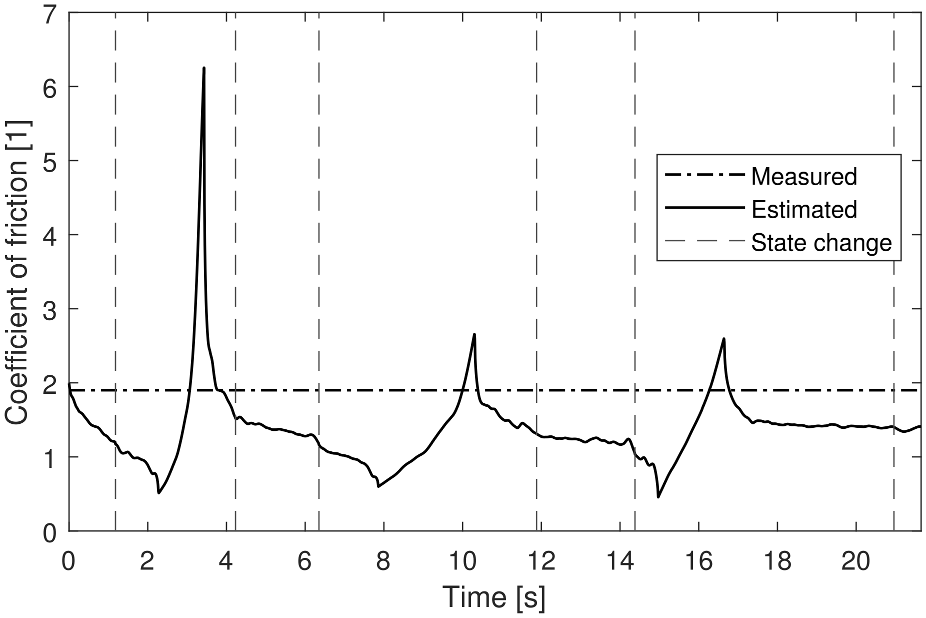

Figure 6.18: Estimation results, for the red emery paper, with contact patch half-length of $a = 40$ mm

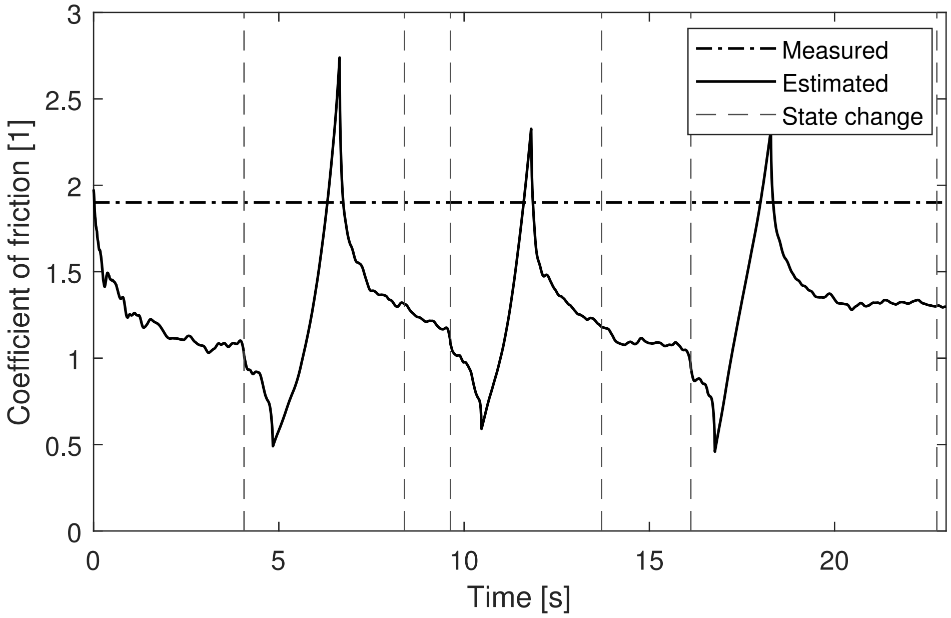

Figure 6.19: Estimation results, for the red emery paper, with contact patch half-length of $a = 40$ mm

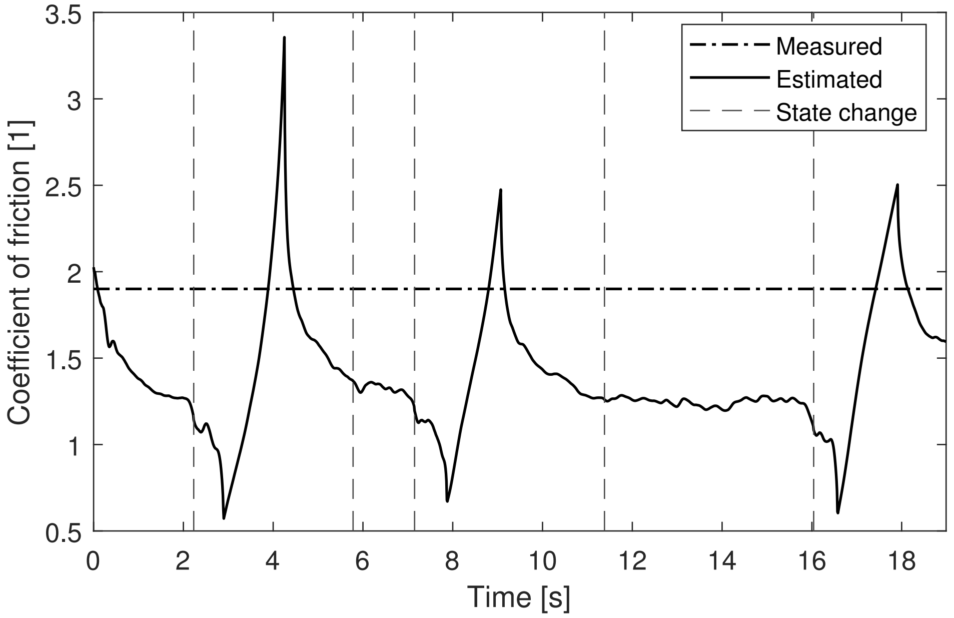

Figure 6.20: Estimation results, for the red emery paper, with contact patch half-length of $a = 45$ mm

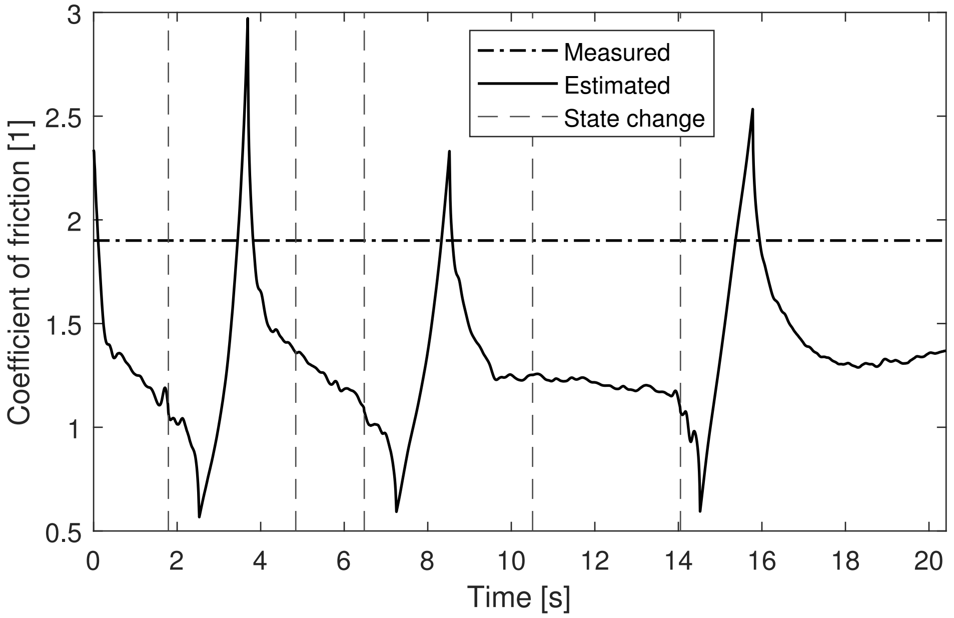

Figure 6.21: Estimation results, for the red emery paper, with contact patch half-length of $a = 45$ mm

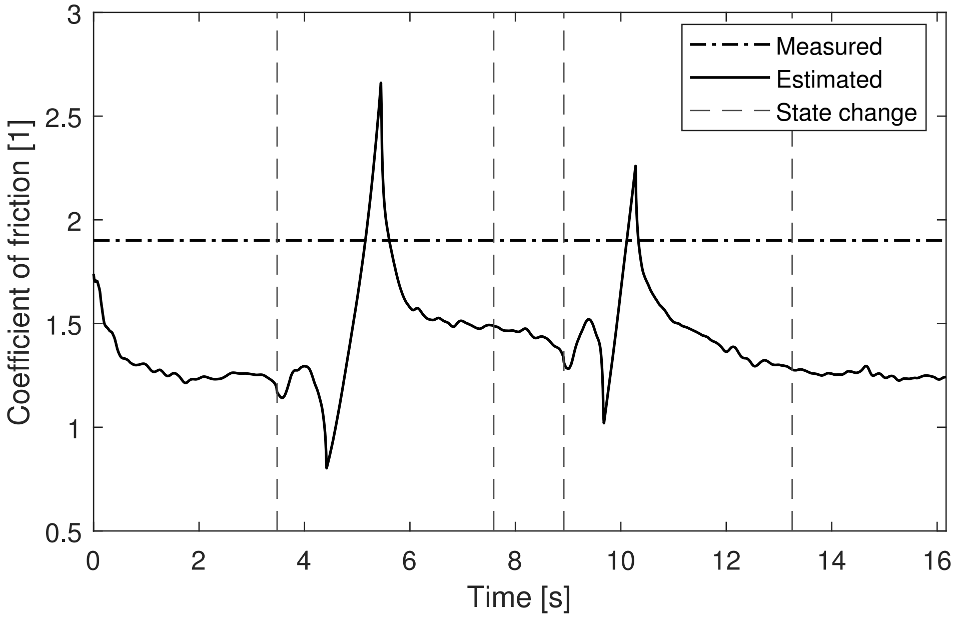

Figure 6.22: Estimation results, for the red emery paper, with contact patch half-length of $a = 50$ mm

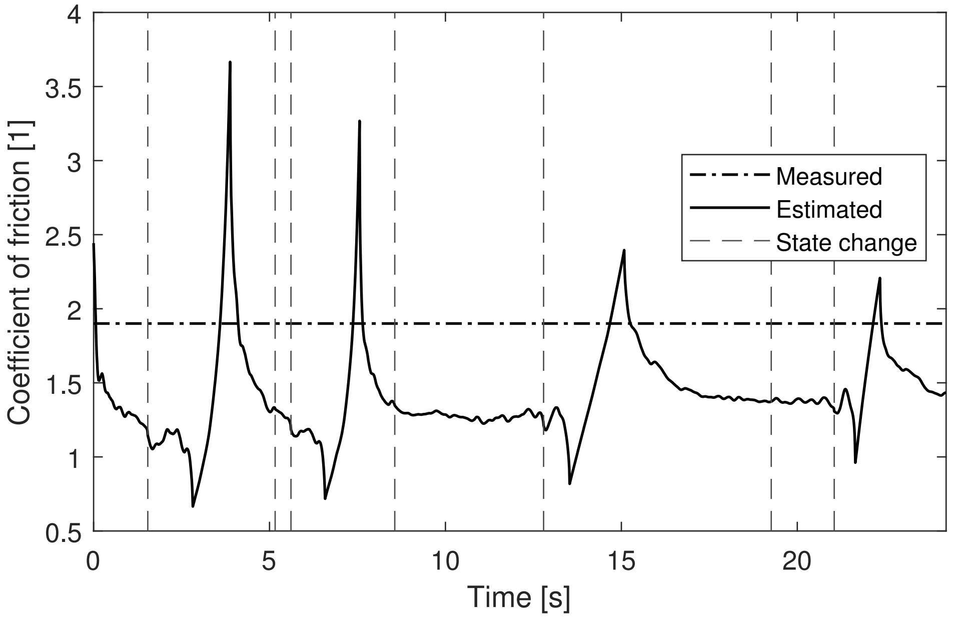

Figure 6.23: Estimation results, for the red emery paper, with contact patch half-length of $a = 50$ mm

Comparing charts of the estimation results for the validation measurements

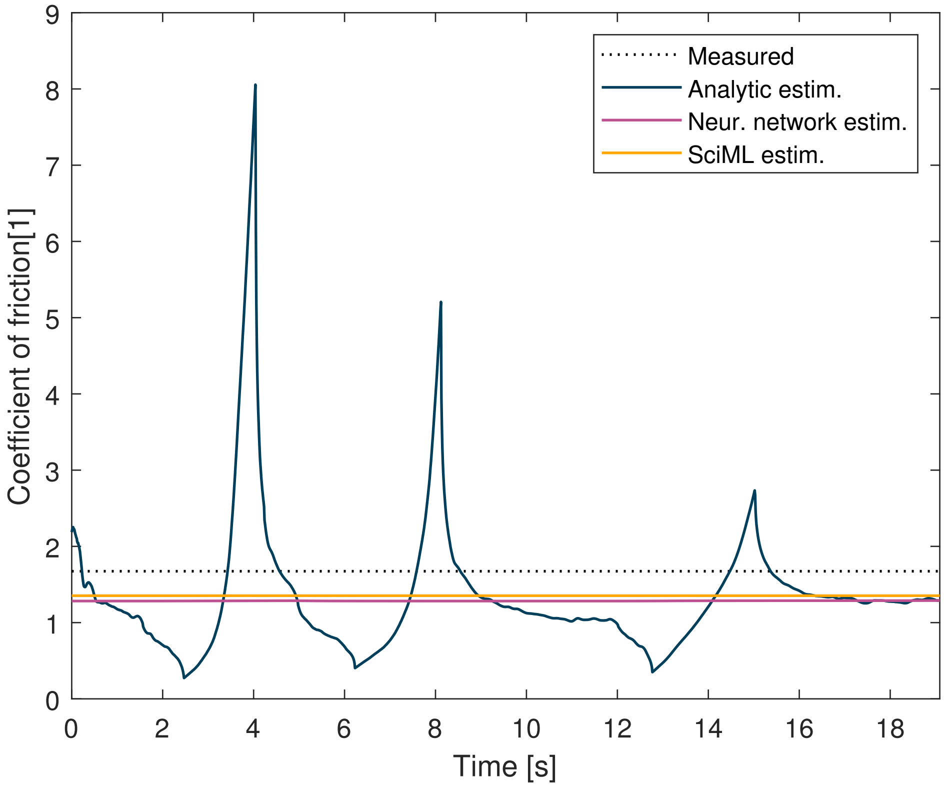

Figure 6.24: Comparing the results of each estimation method for the first validation measurement.

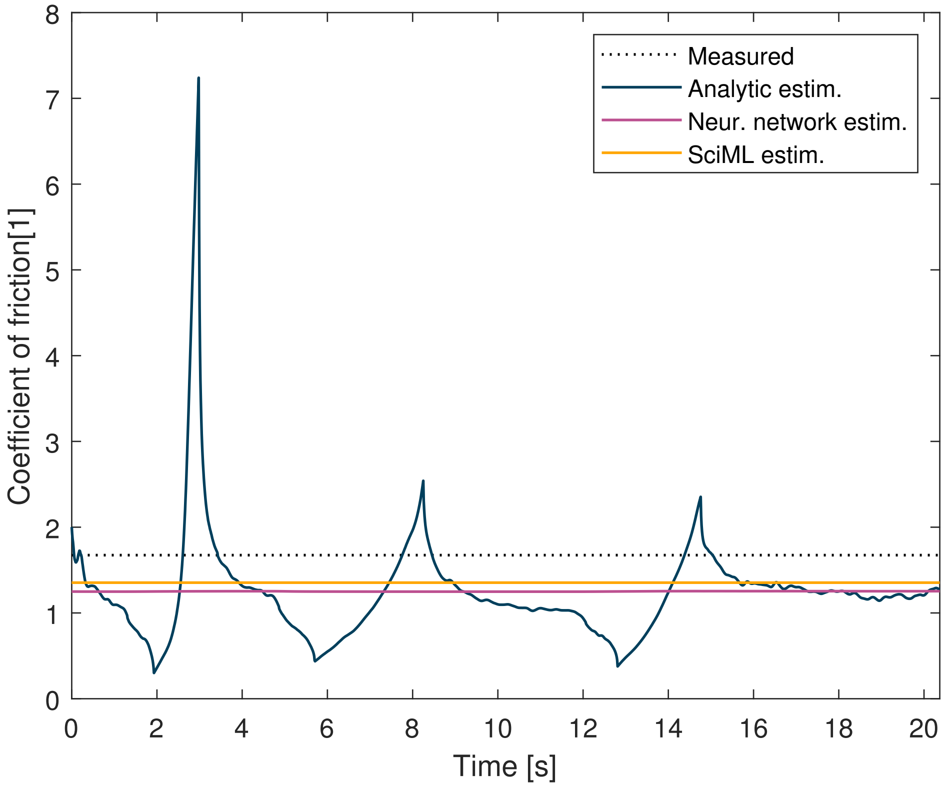

Figure 6.25: Comparing the results of each estimation method for the second validation measurement.

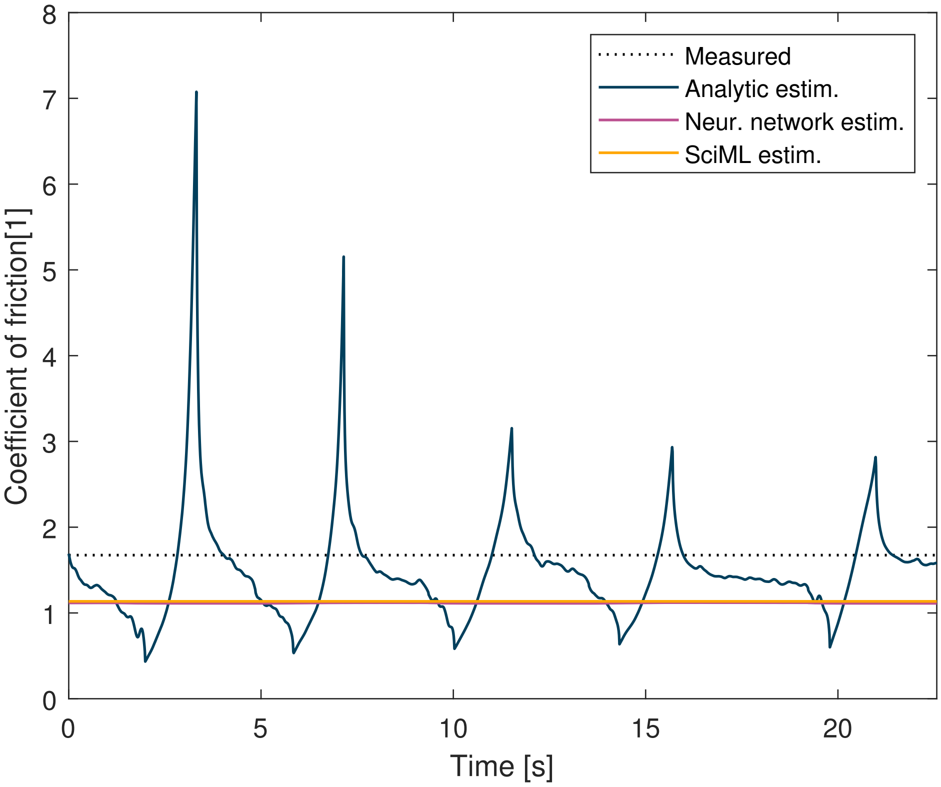

Figure 6.26: Comparing the results of each estimation method for the third validation measurement.

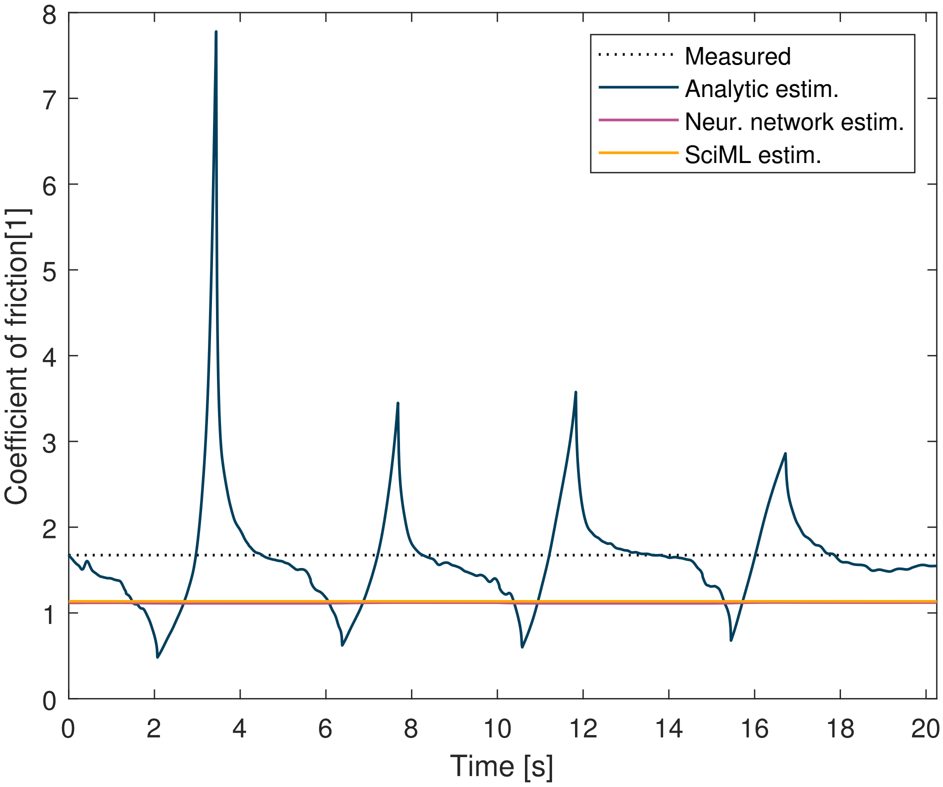

Figure 6.27: Comparing the results of each estimation method for the fourth validation measurement.

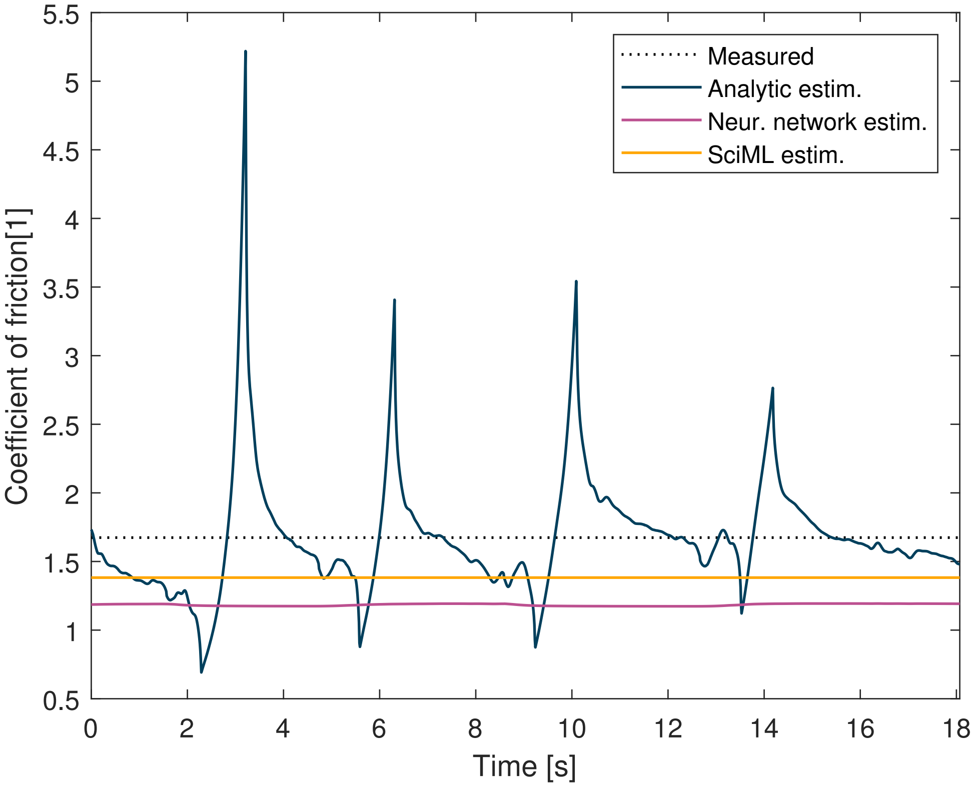

Figure 6.28: Comparing the results of each estimation method for the fifth validation measurement.

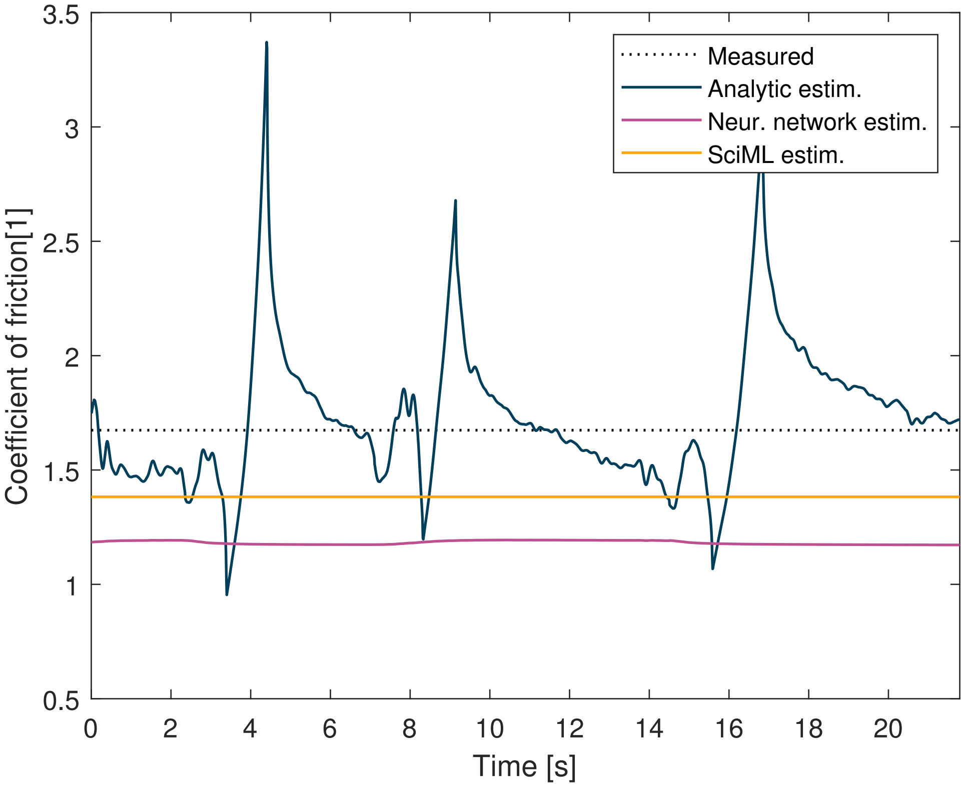

Figure 6.29: Comparing the results of each estimation method for the sixth validation measurement.